Probing the Acceleration Region of the Solar Wind Using UltraViolet Spectroscopy

Huw Morgan

Supervisor: Prof S. Rifai Habbal

Thesis Submitted for the Degree of Philosophy

of the University of Wales, Aberystwyth

January 2005

Solar Physics Group

Institute of Mathematical and Physical Sciences

University of Wales

Aberystwyth SY23 3BZ

DECLARATION

This work has not previously been accepted in substance for any degree and is not being concurrently submitted in candidature for any degree.

Signed (candidate) Date

STATEMENT 1

This thesis is the result of my own investigations, except where otherwise stated. Other sources are acknowledged by footnotes giving explicit references. A bibliography is appended.

Signed (candidate) Date

STATEMENT 2

I hereby give consent for my thesis, if accepted, to be available for photocopying and for inter-library loan, and for the title and summary to be made available to outside organisations.

Signed (candidate) Date

Cyflwynaf y gwaith yma i Nia a theuluoedd Bryn Aere a Gorslwyd. Heb eu cymorth a'u cefnogaeth gyson ni fyddai wedi gweld golau dydd!

Acknowledgments

I would like to thank my supervisor Prof. Shadia Habbal for her constant encouragement, patience, and often unfounded belief in me. Many thanks also to my colleague, Dr. Nicholas Labrosse, for answering many of my endless stream of dumb questions regarding a broad range of subjects.

My gratitude to:
Dr. X.Li for many patient hours of advice.
Dr. B.Li for his advice and the use of his model results in chapter 7.
Dr. K.Birkinshaw for his valuable insights on spectral deconvolution.
Dr. L.Gardner, Dr. A.Panasyuk and Dr. R.Suleiman for their useful advice on the UVCS instrument and data analysis.
J.McAteer and S.Bloomfield at Queens University Belfast for their assistance on wavelet analysis.
Scott McIntosh for his valuable input on an earlier version of chapter 6.
Dr. S.Fineschi for providing the impetus for chapter 7.
Dr. E.Quémerais and Dr. P.Lamy for the electron density maps.
Dr. A.Stanger for quick access to data.
Dr. Andy Breen, Dr. Nicholas Fenwick, Dr. R.Fay-Siebenburgen and Dr. Richard Woo for interesting conversations on solar physics and science in general.

The UVCS/SOHO instrument is a collaborative effort between NASA, the Agenzia Spaziale Italiana and a Swiss participation. The ground-based polarized brightness (pB) data used in this thesis are from the Mauna Loa Solar Observatory's MKIV coronagraph, operated by the High Altitude Observatory (HAO). HAO is a division of the National Center for Atmospheric Research, which is sponsored by the National Science Foundation (USA). The space-based pB data used in this thesis is courtesy of the LASCO/SOHO consortium. SOHO is a project of international cooperation between ESA and NASA.

Summary

This thesis is concerned with observations of the inner corona by UVCS/SOHO. An iterative scheme is introduced which exploits observations of the O VI doublet at 1031.9 and 1037.6Å to give density, temperature and outflow velocity of the O^{5+} ions. The technique is applied to UVCS observations of the solar maximum corona. The results show less contrast between plasma parameters within a streamer and a neighboring region than that seen in the solar minimum corona. The non-streamer region has different conditions from the streamer, but not conditions typical of a coronal hole, suggesting that some regions of the corona are best defined as quiet regions.

A contribution from sunspots in the incident radiation which excites the coronal O^{5+} ions has a large impact on the intensity ratio of O VI. The study of a large solar maximum active region streamer shows that a contribution from sunspots in the quiet disk spectrum allows the model to converge to non-zero outflow velocities at low heights.

A parameter study shows that observed differences between O VI 1032 and 1037 linewidths is due to the different balance of radiative and collisional components in each line, a balance sensitive to outflow velocity and temperature anisotropy. The linewidth ratio serves as an additional constraint on O VI modelling.

Time analysis shows that significant oscillations exist in the intensity of the Ly-α line. A preference toward 7-8 minute oscillations is found. These are interpreted as compressional density waves, the detection of which provides observational impetus for models of coronal heating.

The Solar Probe mission will reach heights as low as $4R_{\odot}$. The spectral profiles from a UV spectrometer aboard Solar Probe are modelled. The instrument will observe away from the Sun along a radial direction, and the modelled O VI profiles have separated collisional and radiative components, promising excellent solar wind diagnostics.

Commonly Used Abbreviations

CDS - Coronal Diagnostic Spectrometer

CME - Coronal Mass Ejection

DAS - Data Analysis Software (of UVCS)

EIT - Extreme ultraviolet Imaging Telescope

ESA - European Space Agency

EUV - Extreme UltraViolet

FOV - Field of View HAO - High Altitude Observatory

IDL - Interactive Data Language

IMP - Interplanetary Monitoring Platform

IPS - InterPlanetary Scintillation

LASCO - Large Angle and Spectrometric COronagraph

LOS - Line Of Sight

MDI - Michelson Doppler Imager

MHD - MagnetoHydroDynamic

MKIV - Mauna Loa Mark IV Coronagraph

NASA - National Aeronautics and Space Administration

O VI 1032 - O VI 1031.9Å spectral line

O VI 1037 - O VI 1037.6Å spectral line

pB - Polarized Brightness

POS - Plane Of Sky

SNR - Signal to Noise Ratio

SoHO - Solar and Heliospheric Observatory

SUMER - Solar Ultraviolet Measurements of Emitted Radiation

TRACE - Transition Region And Coronal Explorer

UV - UltraViolet

UVCS - UltraViolet Coronagraph Spectrometer

$V_{1/e}$ - $1/e$ linewidth in velocity units

WLC - White Light Channel (of UVCS)

Abstract

The solar wind is heated and accelerated in the inner corona. UltraViolet (UV) spectroscopy of this key region has led to many important discoveries which have provided essential constraints on models of coronal energy deposition. Despite such advances, many aspects of the structure and dynamics of the inner corona remain unresolved. This thesis is primarily concerned with the semi-empirical modelling and time analysis of inner coronal observations made by the UltraViolet Coronagraph Spectrometer (UVCS) aboard the Solar and Heliospheric Observatory (SOHO).

An iterative inversion scheme is introduced which fully exploits UVCS observations of the O VI doublet at 1031.9 and 1037.6Å to give the density, temperature and outflow velocity of the O^{5+} ions. In previous semi-empirical modelling of UVCS observations, the ion density is fixed in proportion to the electron density. A major contradiction is inherent to such an approach, since the results of coronal hole semi-empirical modelling have shown overwhelming evidence for the preferential acceleration of heavy ions relative to the background plasma. Preferential acceleration guarantees that the ion density will not remain proportional to the electron density within coronal holes. It is also known that ion abundance is generally enhanced in streamers, and that the cores of quiescent streamers at low heights show a major depletion of O^{5+} ions. The scheme developed for this thesis determines ion density directly from the observed O VI intensity, independently of the electron density. This is a powerful new approach to spectroscopic coronal observations. The comparison of ion to electron densities at several heights can show direct evidence of preferential acceleration. Estimates of ion density and outflow velocity at several heights gives ion mass flux, which is used to constrain assumed parameters within the empirical model.

Publications based on the analysis and semi-empirical modelling of UVCS observations have concentrated mainly on the solar minimum corona. Semi-empirical modelling of solar maximum UVCS observations are rare due mainly to the complex structure of the corona during solar maximum. In this thesis, the iterative inversion technique is applied to several UVCS observations of the solar maximum corona. The results show far less contrast between the plasma parameters of a streamer and a neighboring region than that seen in studies of the solar minimum corona. The non-streamer region does not possess conditions typical of a coronal hole, but nevertheless is significantly different from the streamer in most parameters. Such regions which are not associated with neither streamers nor coronal holes are often seen in the solar maximum corona and are defined

here as quiet coronal regions. There is slow but significant outflow of O^{5+} ions, with acceleration between heights of 3.1 and $5.1R_{\odot}$, in both the streamer and the quiet coronal region. O^{5+} mass flux suggests a $T_{\parallel} = 0.1T_{\perp}$ temperature anisotropy in the quiet corona, and a comparison of ion to electron density shows evidence of preferential ion acceleration.

The O VI disk spectrum emitted from sunspots is very different from the spectrum emitted from the quiet Sun or coronal holes. Including a contribution from sunspots in the incident radiation which excites the coronal O^{5+} ions has a large impact on the intensity and intensity ratio of the coronal O VI spectral lines. This has important implications for the calculation of the outflow velocity of the O^{5+} ions. Existing model studies of O VI spectral lines from UVCS streamer observations often conclude that O^{5+} ions have no significant outflow velocity at heights below $\sim 3R_{\odot}$, and extremely large increases in outflow velocity are calculated above this height. These results are interpreted as different flows arising from the closed and open magnetic field regions within streamers. The observations are always modelled with a typical O VI quiet Sun disk spectrum. This thesis shows that the presence of sunspots within the relevant regions of the Sun's disk concurrent with such streamer observations would demand a revision of the published results. The study of a large solar maximum active region streamer shows the presence of a large sunspot cluster at the streamer base. The inclusion of a 3% contribution from sunspots in the modelled quiet disk spectrum allows agreement between the observed and modelled intensity ratio at lower heights at non-zero outflow velocities. This can not be achieved with a standard quiet Sun disk spectrum. With a sunspot contribution, the O^{5+} ions have an outflow velocity of ~ 80 km s^{-1} at a height of $3R_{\odot}$, increasing linearly to ~ 260 km s^{-1} at a height of $8R_{\odot}$.

Published results on the modelling of the linewidth of the Ly-α coronal line showed largely negligible sensitivity to outflow velocity. A parameter study in this thesis shows that this is due to the dominance of the radiative component of the Ly-α line, and that the linewidth of the collisional component of a coronal spectral line is far more sensitive to outflow velocity. This has important consequences for the interpretation of O VI linewidths as a measure of ion temperature. The iterative inversion scheme, in contrast to previous semi-empirical modelling of UVCS O VI observations, removes the influence of outflow velocity on the calculation of ion temperature.

Observed O VI 1032 and 1037 linewidths often differ significantly. Although mentioned in the literature, this effect has not been adequately explained, and has not been exploited as an additional

constraint on the modelling of UVCS observations. A parameter study shows that the 1032/1037 linewidth ratio is sensitive to the different balance of radiative and collisional components in each line, a balance sensitive to outflow velocity and temperature anisotropy. The linewidth ratio will serve as an extra diagnostic for the calculation of ion temperature anisotropy and outflow velocity in the iterative inversion scheme.

In contrast to many other solar spectroscopic instruments (such as SUMER and CDS on SOHO), UVCS observations of coronal spectral lines have not been subjected to detailed time analysis. This thesis shows that oscillations with significant power exists in the line intensity of Ly-α observed by UVCS. A preference toward 7-8 minute oscillations is found. The oscillations are interpreted as the signature of compressional density waves, the detection of which at heights observed by UVCS provides observational impetus for models of coronal energy deposition.

The future Solar Probe mission will fly to heights as low as $4R_{\odot}$. The spectral profiles from a UV spectrometer aboard such a spacecraft are modelled and discussed - an analysis essential in the proposition and planning of such an instrument. The line of sight of the instrument will point away from the Sun along a radial direction, and the resulting O VI modelled profiles are very different from those observed by the current UVCS. The O VI collisional and radiative components are separated, promising excellent diagnostics for ion outflow velocities and ion temperatures.

Contents

1 The Solar Corona and Solar Wind **25**

1.1 Introduction 25

1.2 The Sun, Corona and Solar Wind 27

1.2.1 The Sun 27

1.2.2 The Corona 28

1.2.3 The Solar Wind 30

1.3 Observing the Corona 33

1.3.1 The White Light Corona 34

1.3.2 Observing the Coronal Base in EUV 36

1.3.3 Observing the Extended Corona in UV 36

1.4 Streamers and Coronal Holes 42

1.4.1 Streamers 42

1.4.2 Coronal Holes 47

1.5 Conclusions 52

2 The Coronal O VI Lines - Formation and Modelling **53**

2.1 Introduction 53

2.2 Formation of UV Coronal Emission Lines 53

2.2.1 Collisional Component 55

2.2.2 Radiative Component 56

2.2.3 Other Mechanisms for Emission 57

2.3 Computing the O VI Intensities 57

2.3.1 The Ion Velocity Distribution 57

2.3.2 Analytical Solutions . . . 58
2.3.3 The O VI Spectral Line Program . . . 59
2.4 Doppler Dimming and Pumping . . . 59
2.5 Outflow Velocity and the Intensity Ratio of the O VI Doublet . . . 62
2.5.1 Model Parameters . . . 62
2.5.2 Results and Discussion . . . 64
2.6 Sensitivity of the O VI Intensity Ratio to Various Parameters . . . 65
2.6.1 Chromospheric Spectrum . . . 65
2.6.2 Electron Temperature and Ion Abundance . . . 68
2.6.3 Electron Density . . . 68
2.7 Conclusions . . . 68

3 Instrumentation, Observations and Data Analysis 71

3.1 Introduction . . . 71
3.2 The Instrument . . . 71
3.3 Observations . . . 72
3.4 Basic Data Processing . . . 74
3.4.1 Calibration and Flat Field Correction . . . 74
3.4.2 Combining Data . . . 75
3.4.3 Correcting the Spectrum . . . 76
3.4.4 Stray Light . . . 78
3.5 Spectral Analysis . . . 79
3.5.1 χ^2 Goodness of Fit . . . 80
3.5.2 Minimizing χ^2 . . . 80
3.5.3 Fitting Lines with Multiple Gaussians . . . 81
3.5.4 Uncertainties . . . 83
3.6 Interpreting UVCS Linewidths . . . 84
3.7 Sliding Windows and Contour Maps . . . 86
3.8 Electron Density from LASCO C2 Observations . . . 88
3.9 Conclusion . . . 90

4 Coupling Observations with Models 91

4.1 Introduction . . . 91

4.2 An Iterative Scheme . . . 92

4.2.1 A Brief Test of the Method . . . 93

4.2.2 Non-uniqueness of the Solution . . . 94

4.3 Plane of Sky Approximation . . . 94

4.3.1 Observations . . . 95

4.3.2 Other Parameters . . . 97

4.3.3 Results and Discussion . . . 98

4.3.4 Conclusion . . . 101

4.3.5 2D Maps of Ion Parameters . . . 102

4.4 Mass Flux as a Constraint on Assumed Parameters . . . 105

4.4.1 Observations . . . 105

4.4.2 Results and Discussion . . . 108

4.4.3 Conclusions . . . 111

4.5 Conclusions . . . 112

5 The Linewidth Ratio of the O VI 1032 and 1037.6 Å Doublet 115

5.1 Introduction . . . 115

5.2 Observation . . . 116

5.3 The Model . . . 118

5.4 Results and Discussion . . . 120

5.5 Implications for the Inversion Method . . . 123

5.6 Conclusions . . . 125

6 Hydrogen Ly-α Intensity Oscillations Observed by UVCS/SOHO 127

6.1 Introduction . . . 127

6.2 Observations . . . 128

6.3 Data Analysis . . . 130

6.4 Results . . . 132

6.4.1 Significant Oscillations . . . 132

6.4.2 Similar Spectra at Neighboring Heights 133
6.4.3 Similar Spectra Across the Slit 134
6.5 Discussion 136
6.6 Conclusions 139

7 The Future of UVCS - a Radial Line of Sight 141
7.1 Introduction 141
7.2 A Radial Line of Sight 142
7.2.1 Collisional Component 142
7.2.2 Radiative Component 144
7.3 Modelled O VI Profiles 145
7.4 Discussion and Conclusion 155

8 Conclusion and Perspectives 157
8.1 Conclusion 157
8.2 Perspectives 159
8.2.1 The Iterative Inversion Scheme 159
8.2.2 UVCS Time Analysis 160
8.2.3 UVCS on Solar Probe 161

List of Figures

1.1 The Solar and Heliospheric Observatory 26

1.2 Large scale structure of the Sun 27

1.3 A model solar atmosphere 29

1.4 Total solar eclipse of July 11, 1991 30

1.5 The corona at solar maximum and minimum 31

1.6 Schematic illustration of the Parker spiral 32

1.7 Solar wind speed measured by the Mariner 2 spacecraft. 33

1.8 Examples of Mauna Loa MKIV, LASCO C2 and EIT 284Å images 35

1.9 The concept of Doppler dimming 37

1.10 1970 image of the Ly-α corona 39

1.11 O VI 1032/1037 intensity ratio computed as a function of outflow speed 40

1.12 An UVCS spectrum 41

1.13 Streamers and closed magnetic structure. 43

1.14 Source of the slow wind at solar minimum 44

1.15 Depletion of O VI intensity in streamer cores 45

1.16 Electron temperature across a streamer 46

1.17 O VI temperature across a streamer 47

1.18 Coronal holes at solar minimum and maximum 48

1.19 Solar minimum magnetic structure and solar wind speed measured by Ulysses . . . 49

1.20 UVCS data and derived outflow velocities from polar coronal holes 51

1.21 Observed and modelled O VI intensity ratio in coronal holes 52

2.1 Example of UV emission lines 54

2.2 Line of sight geometry in the corona 55
2.3 Chromospheric profile of O VI and C II - 1 60
2.4 Doppler dimming of O VI 60
2.5 Comparison of chromospheric spectrum and coronal velocity distribution 61
2.6 Observed effective O VI temperature in a coronal hole 63
2.7 Intensity ratio vs. outflow 64
2.8 Observed intensity ratio - coronal hole 65
2.9 Chromospheric profile of O VI and C II - 2 66
2.10 Sensitivity of intensity ratio to incident spectrum. 67
2.11 Sensitivity of intensity ratio to electron temperature 68
2.12 Sensitivity of intensity ratio to electron density 69

3.1 The UVCS instrument 72
3.2 The UVCS field of view 73
3.3 Detector exposure and raw spectrum 74
3.4 UVCS spectral line instrument broadening 76
3.5 Stray light in UVCS observations 79
3.6 Two Gaussian UVCS profiles 83
3.7 Sensitivity of linewidth to outflow speed 85
3.8 Coronal parameters across the UVCS slit 86
3.9 Contour maps of the corona 87
3.10 Contour maps of the corona 89

4.1 Flowchart of iterative scheme 93
4.2 Convergence of parameters 94
4.3 UVCS slit positions 2001/01/18-20 96
4.4 Streamer and non-streamer data from UVCS 2001/01/18-20 97
4.5 Time series of O VI intensity at height $5.1R_{\odot}$ in a streamer 98
4.6 Streamer and non-streamer electron density 2001/01/18-20 98
4.7 Ion densities, outflow velocities and temperatures calculated from the 2001/01/18-20 observations. 99

4.8 Mass flux times height squared for the 2001/01/18-20 observations. 100
4.9 Ratio of ion to electron density for the 2001/01/18-20 observations. 101
4.10 Contour maps of observables for the 2001/01/18-20 observations. 103
4.11 Contour maps of ion density, outflow, temperature and mass flux for the 2001/01/18-20 observations. 104
4.12 UVCS slit positions 2000/01/28-29 106
4.13 EIT and MDI images 2000/01/30 - 2000/02/03 107
4.14 Data from UVCS and LASCO C2, 2000/01/28-29 108
4.15 Ion density, outflow velocity and mass flux calculated from the 2000/01/28-29 observations. 109
4.16 Mass flux calculated from the 2000/01/28-29 observations. 110
4.17 Ion parameters calculated from the 2000/01/28-29 observations. 111

5.1 The South corona in white light on 2000/05/07 117
5.2 O VI UVCS data from 2000/05/5-16 118
5.3 A set of solar wind parameters and the resulting lines. 119
5.4 Intensity and linewidth ratios as functions of outflow velocity, radial velocity gradient and temperature anisotropy. 121
5.5 Contour plots of O VI radiative and collisional emission 122
5.6 1037 linewidth under plane of sky and spherical symmetrical approximations . . . 124

6.1 Positions of UVCS observations 2002/06/20-21 129
6.2 Example of wavelet and global power spectrum 132
6.3 Examples of observed time series and power spectra 133
6.4 Normalized global spectra at the same latitude 134
6.5 Normalized global spectra across the slit 135
6.6 Histograms of significant oscillations 137
6.7 Distribution of significant oscillations across the UVCS slit 138

7.1 Planned trajectory of Solar Probe 142
7.2 Radial LOS geometry 143
7.3 MHD Model Parameters 146

7.4 Modelled O VI profiles - streamer with low $T_{\|}$ 147
7.5 Modelled O VI profiles - streamer with high $T_{\|}$ 149
7.6 Modelled O VI profiles - coronal hole with low $T_{\|}$ 151
7.7 Modelled O VI profiles - coronal hole with high $T_{\|}$ 153

List of Tables

2.1 Measurements of Chromospheric O VI and C II 66

3.1 Comparison of Gaussian parameters fitted using UVCS DAS and a genetic algorithm 82

4.1 Details of UVCS observations 2001/01/18-20. 97

4.2 Details of UVCS observations 2000/01/28-29 105

6.1 Details of UVCS observations 2002/06/20-21. 128

Chapter 1

The Solar Corona and Solar Wind

1.1 Introduction

> *The solar corona has long been one of the chief mysteries of astrophysics. Due to the pioneer work of many investigators, culminating in Lyot's invention of the coronagraph and Edlén's identification of the emission lines, it now has lost some of its secrets. Yet the problems relating to the heating of the corona and to its structural details still remain very puzzling. (van de Hulst, 1950)*

These words are from a 1950 paper by van de Hulst (1950) before the modern picture of a dynamic, magnetically dominated outflowing corona was conceived. Since 1950 there have been great advances in the development of tools for observing the corona and the last decade has seen the deployment of spacecraft such as the Solar and Heliospheric Observatory (SOHO, see figure 1.1), dedicated to multi-instrument observations of the Sun. Despite such detailed observations and recent complex and sophisticated models of the corona, Van de Hulst's last sentence remains as relevant today as it was half a century ago. Many aspects of coronal heating and structure still remain very puzzling.

Recently a strong emphasis has been made in solar physics on the concept of space weather. This term encompasses the study of the dynamic and sometimes explosive nature of the corona from the Sun to the Earth and beyond. Such studies have blossomed in the last decade due to the large amount of data collected by the plethora of instruments trained on the Sun and her atmosphere. Explosive events called Coronal Mass Ejections (CME) can be closely tracked from magnetic disturbances

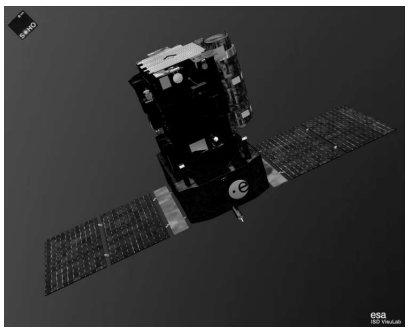

Figure 1.1: The Solar and Heliospheric Observatory (SOHO). SOHO was launched in 1995 and observes the Sun from an orbit around the L1 Lagrangian point between the Sun and Earth.

on the Sun's disk out to heights* of 30 solar radii ($R_\odot$†) using instruments aboard SOHO. These events are then observed near Earth as a storm of energetic particles. A less dramatic but no less important example is the slow and dense solar wind flow measured near Earth which is associated with structures called streamers in the inner corona. These streamers are in turn often associated with closed magnetic field structures rising from regions of enhanced magnetic activity on the Sun's disk. Fast and low density solar wind flow measured near Earth is associated with regions called coronal holes in the inner corona.

It is fascinating that space weather conditions as far out as Earth and beyond are dictated by conditions on the Sun. Despite our ability to observe this link, there are large gaps in our understanding of it. The largest mystery lies in the nature of the evolution of the inner corona as it expands outwards from the Sun into interplanetary space. The acceleration and heating of the solar wind must happen in the region from the base of the corona to $\sim 10 R_\odot$. The imprint of conditions on the Sun's disk must also be preserved.

In situ measurements have not been made closer than ~0.3 AU‡ to the Sun by the Helios spacecraft (Schwenn & Marsch, 1991), but we can study the inner corona remotely. Currently, Ultra-Violet (UV) and white light observations offer the best diagnostics for inferring conditions in the inner corona. The main emphasis of this work is analysis of inner coronal UV observations made by an instrument called the UltraViolet Coronagraph Spectrometer (UVCS) aboard SOHO. UVCS has made many discoveries that have both deepened our understanding as well as raise new questions of the inner corona and the solar wind.

*Heights given in this thesis are always measured from Sun center.
†$1 R_\odot = 6.96 \times 10^5$ km
‡Astronomical Unit, distance from the Sun to Earth. 1 AU = $215 R_\odot$

This chapter gives brief descriptions of the Sun, corona and solar wind in section 1.2. Section 1.3 gives an introduction to methods of observing the corona remotely, with an historical overview of the development of coronal UV spectroscopy. Section 1.4 gives a detailed overview of streamers and coronal holes, with particular emphasis on the discoveries made by UVCS observations. A brief conclusion ends the chapter.

1.2 The Sun, Corona and Solar Wind

1.2.1 The Sun

The Sun is a fascinating object. It dictates the rhythm of our lives and of most life on Earth. Throughout history it has held a religious significance for most peoples and it is only recently that scientific observation has given us a reasonable understanding of the Sun. The Sun is a massive (1.99×10^{30} kg) sphere of gas compromised by mass of 74% Hydrogen, 25% Helium and 1% other elements. Figure 1.2 shows the large scale structure of the Sun and its atmosphere. The Sun's energy is created by nuclear fusion in the core and is transported by radiation and convection to the solar atmosphere, the lowest layer of which is the photosphere.

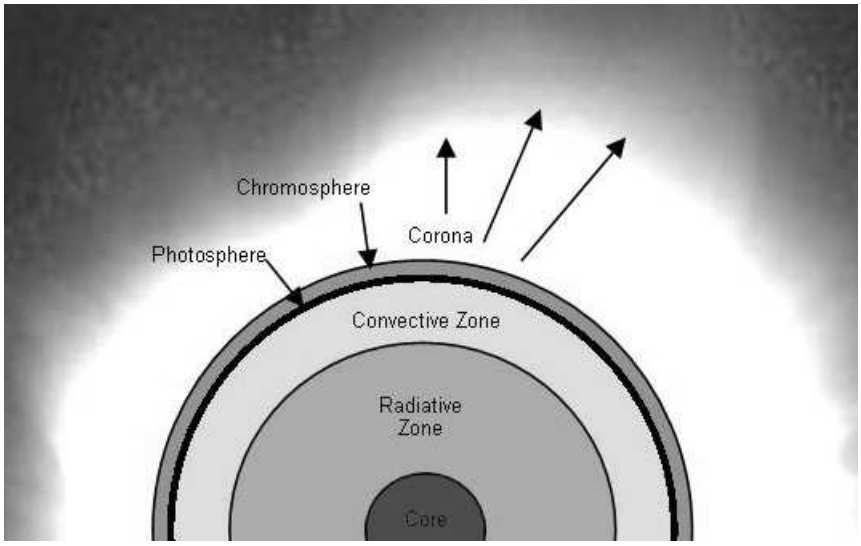

Figure 1.2: The large scale structure of the Sun.

1.2.2 The Corona

The photosphere is an extremely thin layer of plasma which emits most of the solar radiation. It is dense and opaque compared to the overlying chromosphere and corona, therefore most of the light emitted in the photosphere escapes into space. The boundaries between the photosphere, chromosphere and corona are defined by the general temperature profile as a function of height. The corona is the hot (> million K) outer part of the Sun's atmosphere. Its lower boundary is at the transition region between the chromosphere and corona , ~2000 km above the photosphere. The Earth is encompassed by a stream of charged particles known as the solar wind, which can be thought of as a part of the Sun's outflowing corona. The strong magnetic field of the Sun emerges from the photosphere and permeates the corona, so that coronal structures and their dynamics are closely linked to those of the Sun.

During the total solar eclipse of 1869 a puzzling emission line was discovered in the spectrum of the corona. The presence of this 'green line' and other lines in the coronal spectrum was a great mystery to astrophysicists at the time and remained so for over half a century (Young, 1884). No satisfactory match could be found with spectroscopic laboratory measurements and the spectral line was attributed to an undiscovered new element called coronium (see Clerke (1898)). This was not such an extreme proposition since Helium was first detected with coronal spectroscopy in 1868 and only later discovered on earth (Ramsay, 1896). It was 1939 before Edlén correctly identified four of the green lines with the spectral lines of Fe X, Fe XI, Ca XII and Ca XIII (Swings, 1943). These highly ionized states of iron and calcium implied a very hot corona - more than a million degrees. Such a hot corona was surprising since the photosphere is at a temperature of around 4300 K and the temperature was naturally expected to decrease from the surface upward as one moved further from the energy source of the solar interior.

Figure 1.3 illustrates the accepted general current model of temperature and density in the solar atmosphere. The boundary between the photosphere and chromosphere is defined by the minimum in temperature. The boundary between the chromosphere and corona is the narrow transition region, where there is an extreme rise in temperature and drop in density. The temperature of formation of a few ions is also shown in figure 1.3. O VI, or O 5+, is an oxygen atom with five of its electrons stripped by collisions with the energetic electrons. To achieve the high ionisation of these ions the surrounding plasma must be at a high temperature. The heating mechanism behind the rise

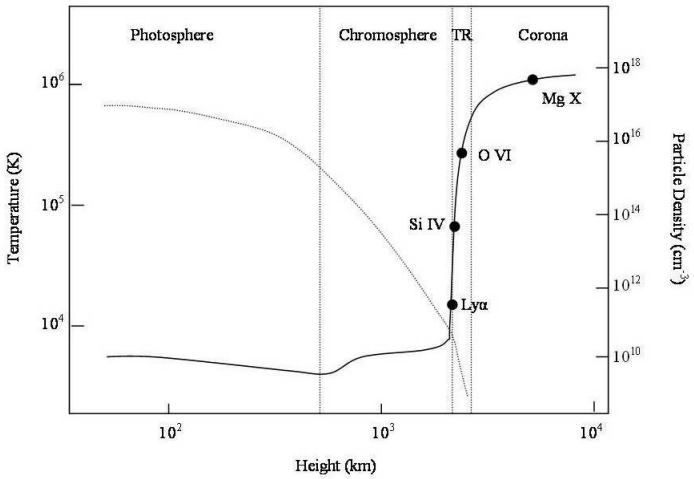

Figure 1.3: Temperature (solid line) and density (dotted line) in a model solar atmosphere. Height is measured from the base of the photosphere (Peter, 2002).

in temperature through the chromosphere and the extreme rise through the transition region to the million degree corona remains largely an unanswered question in solar physics.

The influence of the Sun's magnetic field on the structure of the corona can be clearly seen in high quality white light images. One example is the eclipse image of figure 1.4, a North American total solar eclipse of 1991 July 11. It is a mosaic of several processed digital images composed to enhance the fainter regions furthest from the Sun. The corona in this image shows a general radial structure. Thin threads of enhanced intensity which reach out from the Sun into the extended corona can be seen most clearly in the darker regions of the North, North-east and South-west corona. These are filamentary structures or plumes. Higher intensity candle-flame shaped structures extend from the Sun along the South-easterly and North-westerly radial directions. These are called streamers. Streamers can be associated with regions of sunspots and high magnetic activity called active regions on the photosphere. Streamers, coronal holes and quiet regions are long-lived and large-scale structures in the corona, and will be discussed in detail in section 1.4.

The number, latitudes and areas of sunspots on the photosphere have been recorded for over three centuries. Over this time a reasonably regular cycle can be seen in the number of sunspots, with a period of ~11 years. The sunspot cycle is a manifestation of the global magnetic cycle of the Sun. Reflecting the changing magnetic activity emerging from the photosphere, the coronal structure changes drastically during the solar cycle. Figure 1.5 shows the contrast between the corona at the minimum and maximum of the sunspot cycle using images taken by the Large Angle

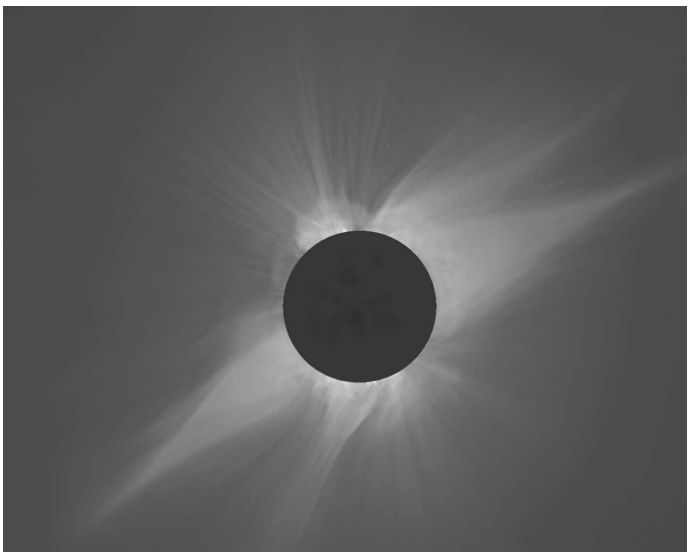

Figure 1.4: Total solar eclipse of July 11, 1991 as seen from Baja California. The image is a mosaic of five separate images each exposed to enhance different distances from the Sun. The photographs were taken by Dennis di Cicco (Sky and Telescope) and Gary Emerson (E. E. Barnard Observatory), digitized by David Sime (High Altitude Observatory) and processed by Steve Albers (Boulder, CO).

and Spectrometric Coronagraph (LASCO)/SOHO C2 instrument* . During solar minimum (figure 1.5a) streamers are restricted near to the Sun's equator while at maximum (figure 1.5b) they can appear at all latitudes.

1.2.3 The Solar Wind

The first clues suggesting the possible existence of a continuous stream of charged particles from the Sun emerged in the 19^{th} century with the observation of anti-sunward pointing comet tails. Many observers assumed that the comet tails were made of solid particles on which was acting a repulsive force directed anti-sunward (see Festou et al. (1993)). In the late 19^{th} century it was also noticed that flares on the Sun sometimes coincided with magnetic storms on Earth, a further indication of a connection between the Sun and the Earth (Carrington, 1859; Hodgson, 1859).

The existence of a static interplanetary gas was assumed in the first half of the 20^{th} century to explain the polarization of the zodiacal light (van de Hulst, 1947; Whipple & Gossner, 1949; Rense, 1952). Soon after, observations of accelerated anti-sunward pointing comet tails discounted a stationary gas and provided mounting evidence for an interplanetary wind outflowing from the Sun with speeds of 500 to 1500 km s^{-1} (Biermann, 1957). Inspired by the observations of Biermann,

*LASCO and the C2 coronagraph will be described in section 1.3.

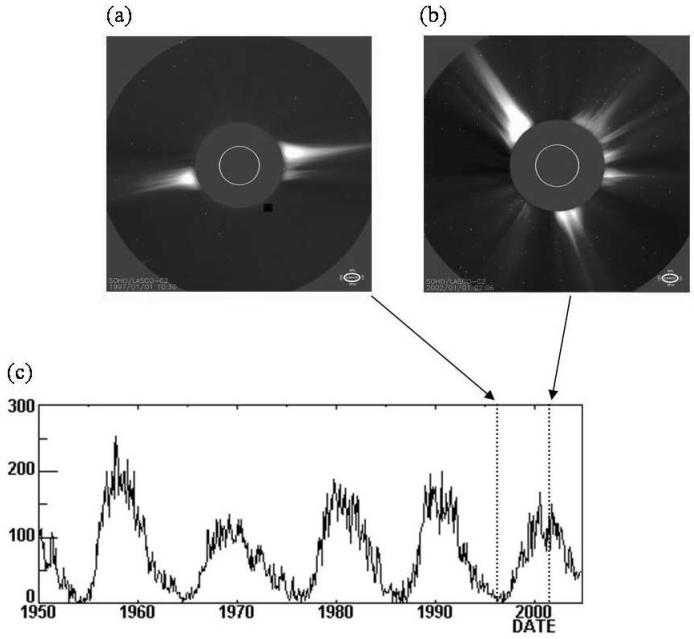

Figure 1.5: LASCO C2 coronagraph images of (a) streamers restricted close to the equator at solar minimum (1997/01/01) and (b) streamers at all latitudes at solar maximum (2002/01/01). (c) shows the monthly average sunspot numbers from 1950 to present.

Parker (1958) abandoned ideas of a hydrostatic corona and showed that a hot gas would create enough pressure to counteract the Sun's gravity. This would ensure a constant outflow of material from the Sun. The conservation of mass and momentum in a spherically symmetric isothermal corona allowed Parker to calculate expansion speed as a function of height for various temperatures. A supersonic flow, in general agreement with the observational constraints of Biermann, arises naturally from reasonable coronal temperatures of $\sim 10^6$ K or higher.

Parker (1958) was also successful in predicting the general shape of the interplanetary magnetic field. The typical timescales for significant bulk motions of the coronal plasma, t_v, are much smaller than the timescales for the Sun's magnetic field to diffuse, t_d. This is reflected by high values of the dimensionless magnetic Reynolds number, $R_m = t_d/t_v$. R_m has values of around 10^{13} in the chromosphere. This guarantees that the plasma and magnetic field are inextricably linked, or that the magnetic field is frozen in the plasma. The coronal magnetic field, emerging from the photosphere in a predominately radial direction, is stretched out radially by the expanding corona while the Sun rotates. This creates a magnetic field with a spiral structure called the Parker spiral, pictured in figure 1.6.

The outflowing corona predicted by Parker's model was subsequently directly observed by many

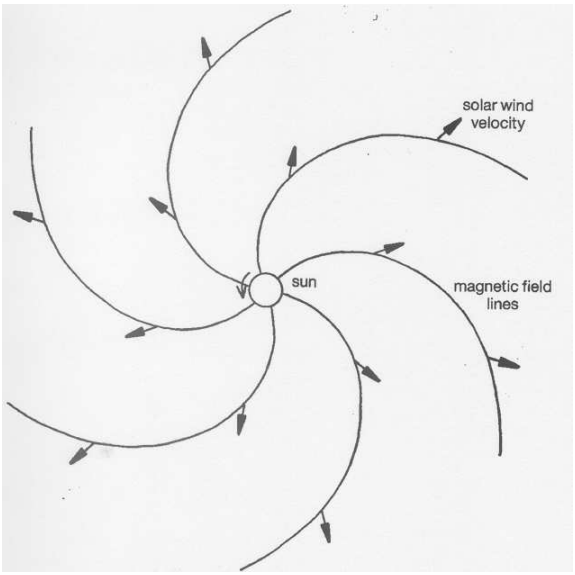

Figure 1.6: The spiral structure of the large-scale interplanetary magnetic field in the ecliptic plane as predicted by Parker (1958). The solar wind flows radially outwards while the magnetic field is drawn into an Archimedal spiral by the rotation of the Sun (from Phillips (1992)).

spacecraft. *In situ* measurements provides the bulk of the knowledge of the solar wind. Measurements by spacecraft of interplanetary electric and magnetic fields can be made, as well as measurements of solar wind composition and particle energies, densities, temperatures and velocities. Despite the richness and quality of the data, the observations are limited to the sparse paths taken by Earth and a few spacecraft in the whole vastness of the heliosphere. InterPlanetary Scintillation (IPS) observations are not so limited, and have been made at a wide range of heights in the corona and heliosphere. Density variations carried by the solar wind cause fluctuations in the phase and intensity of radio signals received from distant sources, for example quasars or spacecraft (Hewish et al., 1964). Cross correlation of these fluctuating signals observed at several different positions on Earth can give information on the outflow velocity of the solar wind (Breen et al., 1996, 2000). IPS can also give information on density and the scale size of density irregularities (Rickett, 1992).

The solar wind is a predominately electron-proton plasma with a few percent helium and traces of heavy ions. At distances of 1 AU, there are two forms of wind. The fast wind has a velocity of around 800 km s^{-1} while the slow wind outflow is 300-400 km s^{-1}. The slow wind is denser than the fast, and is more variable. Fast wind protons are hotter than those of the slow wind, while fast wind electrons are cooler. The Mariner 2 spacecraft, en route to Venus during 1962, yielded the first conclusive detection of the fast and slow solar wind streams (Neugebauer & Snyder, 1966).

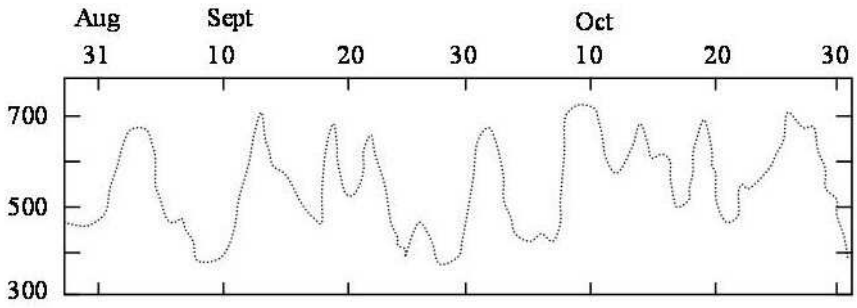

Figure 1.7: Solar wind speed measured over ~62 days by the Mariner 2 spacecraft (from Neugebauer & Snyder (1966)).

Figure 1.7 shows the variations in the speed of the solar wind as seen by Mariner 2 - the values fluctuate from 400 to 700 km/sec. It was observed that the measured pattern of fast and slow wind approximately repeated at 27 day intervals. This suggested that their sources rotated with the Sun. It was several years before advancements in the remote sensing of the inner corona could associate structures at the Sun with the fast and slow wind at Earth.

1.3 Observing the Corona

The corona below heights of ~0.3 AU has only been observed remotely using radio waves (Krüger, 1979), Ultraviolet (UV) (Gabriel, 1971b) and X ray (Vaiana et al., 1973) emission lines, electron scattered white light (van de Hulst, 1950) and IPS (Hewish et al., 1964). Observations of coronal UV emission lines (the E corona) and coronal white light (the K and F corona) dominate this work. The K and F white light coronas are formed by light from the Sun's disk scattered by electrons and dust respectively. The E corona consists of isolated and often highly intense spectral lines emitted by the high temperature ions.

This section includes brief descriptions of white light and Extreme UltraViolet (EUV) observations from instruments which are used in this thesis, and a more detailed introduction to UV observations of the extended corona. IPS, radio and X-ray observations are extremely important in coronal physics but will not be discussed here.

1.3.1 The White Light Corona

White light from the corona is formed by light from the Sun scattered from the electrons and dust in the corona. Even the brightest part of the white light corona near the Sun is around a million times fainter than the Sun's disk and is only visible to the naked eye during a total eclipse. Each century, there are over 200 Solar eclipses, around 60 of which will be total eclipses. In a total eclipse, an observer sees the moon occulting the whole solar disk and for a short period the denser inner solar corona is revealed. Prior to the 19th Century, astronomers were primarily concerned with the predictions and measurements of solar eclipse timing and locations but advances in photography and spectroscopy soon allowed them to use eclipses to study the nature of the corona.

Eclipse observations are still important for today's solar physicists since they offer such a clear view of the corona; enabling high spatial, spectral and temporal resolution at a relatively low budget. However, they do not allow us to observe the Sun on a daily basis and it was Lyot, a French astronomer attempting to observe Mercury near the Sun's limb, who overcame this problem with his invention of the coronagraph in 1931 (Lyot, 1932). A coronagraph employs an occulting disk, placed in front of the telescope entrance, to block most of the unwanted light from the Sun's disk. Figure 1.8a is a processed white light image taken by the ground-based Mauna Loa Mark IV Coronagraph (MKIV). MKIV makes radial scans of the inner corona at heights $\sim$1.1-2.2$R_\odot$ so the image in figure 1.8a has been subject to a transform from polar (θ, r) to cartesian (x, y) solar coordinates. A radial gradient filter is also applied. Radial gradient filters remove the average sharp drop in white light intensity with increasing coronal height to reveal the more interesting latitudinal contrasts. Thus structures such as streamers or coronal holes can be seen projecting radially out to large distances in the corona.

A space-based coronagraph offers large advantages over the ground-based instruments. Observations can be made at any time without weather concerns or stray light from the atmosphere. The Large Angle and Spectrometric Coronagraph (LASCO) instrument aboard SOHO has a set of three coronagraphs, each optimized to view different heights in the corona (Brueckner et al., 1995). The C2 coronagraph has a range of $\sim$2 to 6$R_\odot$ and a processed C2 image is shown in figure 1.8b. The processing includes a radial gradient filter. This figure shows the great improvement in clarity between the ground and space based coronagraphs. The LASCO C1 coronagraph, which was designed for viewing the innermost corona at the same height range as the MKIV instrument, unfortunately

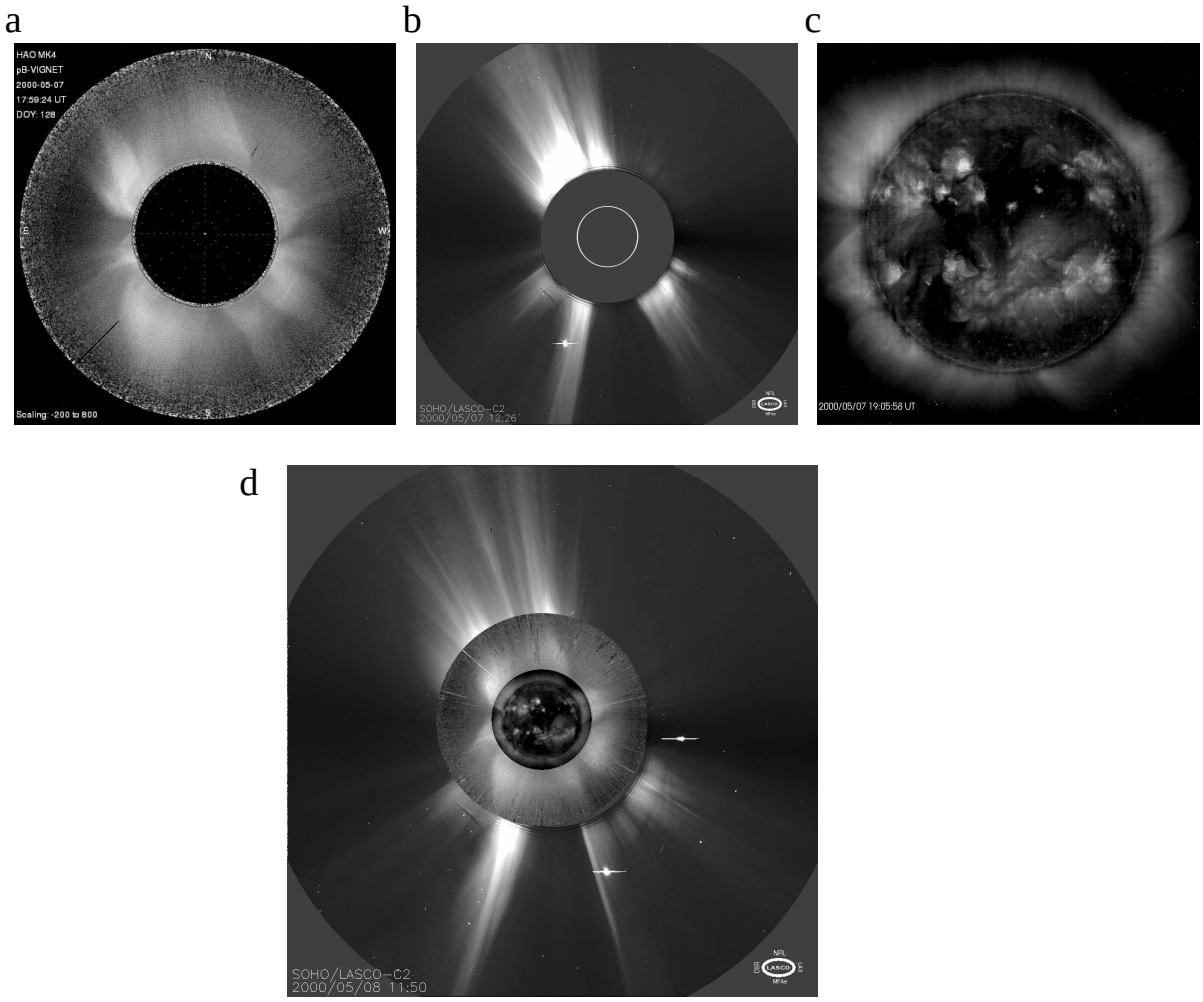

Figure 1.8: Examples of (a) Mauna Loa MKIV (white light), (b) LASCO C2 (white light) and (c) EIT (284Å) images. (d) is a nested composite image of (a), (b) and (c). The images were all observed on 2000 May 8. The central white circle in (b) shows the position of the Sun, hidden behind the occulting disk. The white light images have been processed with a radial filter to artificially enhance features with increasing height.

stopped functioning after the temporary loss of SOHO.

Images from MKIV and the LASCO C2 coronagraphs are often used in this thesis to place spectroscopic coronal observations in the context of large scale density structures. For example, spectroscopic observations of coronal UV lines with relatively high intensities and narrow linewidths are characteristic of streamers, and this is most easily confirmed by looking at the appropriate region in a white light image.

An important application of calibrated white light images, in particular polarized white light images, is to give a measure of coronal electron density. The white light scattered by electrons (the K-corona) is strongly polarized compared to white light scattered by dust (the F-corona), therefore

the F-corona may be removed from polarized brightness (pB) observations. The intensity, I_k of the K-corona white light is then proportional to the electron density along the line of sight (LOS): $I_k \propto \int_0^{+\infty} N_e\, dx$, where the x-axis is along the LOS. An inversion method for obtaining electron density from LASCO C2 and MKIV pB observations is given in chapter 3. Calculations of electron density are important for the modeling of coronal and solar wind plasma parameters.

1.3.2 Observing the Coronal Base in EUV

The Extreme Ultraviolet Imaging Telescope (EIT) aboard SOHO uses filters to pass only certain EUV wavelength ranges. These narrow bandpasses are dominated by emission lines from certain ions. Since the temperatures of formation differ for ions and there is a large temperature gradient at the base of the corona, imaging in lines from different ions creates images at different heights in the corona. Figure 1.8c is an EIT image with a bandpass centered on a wavelength of 284Å which contains a Fe XV line which is formed at ~2.5 MK. Therefore most of the light in this image must be formed in the corona.

As with the white light images, pre-processed EIT images are used in this work to show the connections between structures in the extended corona and structures at the coronal base. For example, in figures 1.8, the streamers seen in the white light images in the North-eastern corona may be associated with the bright regions seen in the EIT image at the same latitude. It is simple and often extremely useful to create composite images from concurrent EIT, MKIV and C2 observations. Figure 1.8d shows an example where figures 1.8a, b and c have been nested together. In this way, the position of streamers or dark regions in the white light images can be traced to the base of the corona.

The Transition Region and Coronal Explorer (TRACE) is a space-based telescope dedicated to viewing the lower corona and transition region. It views narrow spectral bandpasses in the EUV and can focus on small regions of the coronal base, thus achieving a far better spatial resolution than EIT. Closed magnetic structures above active regions can be seen in great detail.

1.3.3 Observing the Extended Corona in UV

Spectroscopic observations of UV emission lines in the extended corona are extremely important. The width of emission lines gives a direct measurement of the velocity distribution of the emitting

ions along the observed line of sight. This can give an accurate measure of ion temperature. The width of the H Ly-α line gives a measure of the coronal proton temperature (Allen et al., 2000; Withbroe et al., 1982). Co-spatial and concurrent measurements of electron density and UV emission line intensities can give estimates of the ion bulk outflow velocity through Doppler dimming techniques. Ion abundances may be calculated from the absolute intensities of emission lines.

Formation of UV Emission and Doppler Dimming.

UV emission lines in the corona are formed by two main processes - collisional and radiative. These processes are described in detail in chapter 2. The collisional component of an emission line is caused by the excitation of ions by collisions with the free, hot electrons of the coronal plasma. The radiative component is formed by photo-excitation of coronal ions by light from the Sun's disk and chromosphere. UV light from the disk and chromosphere consists of many high intensity emission lines and the coronal ions resonate with these so that the brightness of the radiative component of UV coronal lines is dependent on the disk and chromospheric emission.

The concept of Doppler brightening and dimming was first introduced in a coronal context by Hyder & Lites (1970), and concentrated on a ground-based observation of a high intensity eruptive prominence seen near the limb of the corona during March 1969. This pioneering work showed that in the case of UV radiative emission, such as the Lyman-Alpha line of neutral hydrogen at 1216 Å, the intensity would be sensitive to the velocity of hydrogen in the corona relative to the Sun.

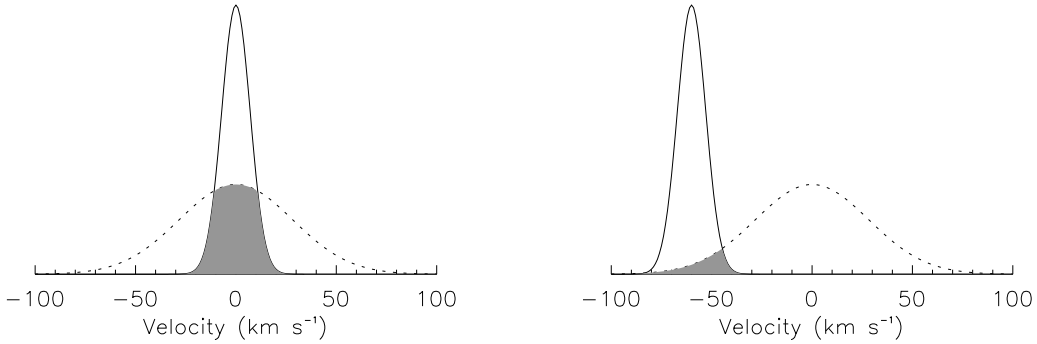

Figure 1.9: Schematic illustrating the simple concept of Doppler dimming. The solid line shows a narrow UV emission line emerging from the Sun's disk translated into the velocity space of the coronal ions. The dotted line shows the wide velocity distribution of the coronal ions in the hot corona. The left plot shows resonance for the case of no bulk flow of the coronal ions. The right plot shows the case for a coronal bulk flow velocity of 60 km s^{-1} away from the Sun. The shaded areas shows the degree of resonance between the disk emission and coronal ions.

The basic concept of Doppler dimming is shown schematically in figure 1.9, where the UV emission from the Sun's disk is shown relative to the velocity distribution of ions in the corona. The left plot shows resonance for the case of no bulk flow of the coronal ions. In this case, a large number of the coronal ions are able to resonate with the emission from the Sun. This is shown by the shaded area. The right plot shows the case for a coronal bulk flow velocity of 60 km s^{-1} away from the Sun. In this case, in the rest frame of the coronal ions, the disk emission is redshifted and much resonance is lost. Coronal outflow can sometimes reach sufficient velocities so that some ions achieve resonance with lines belonging to other ions in the disk spectrum. This is called Doppler pumping. Doppler dimming and pumping diagnostics can give estimates of the bulk outflow velocity of the emitting ions (Withbroe et al., 1982; Kohl & Withbroe, 1982; Noci et al., 1987).

UV Coronal Observations - an Historical Overview

The Earth's atmosphere strongly absorbs UV light and the practical uses of Doppler dimming and other diagnostic techniques were greatly limited by the lower quality of ground-based UV observation. A major breakthrough in coronal UV spectroscopy was achieved during the total solar eclipse of 1970 March 7, when an instrument was flown into the path of totality on a NASA sounding rocket. The resulting observations revealed unexpected images of the corona in Ly-α and other weaker lines (Gabriel et al., 1971a). One such image is shown in figure 1.10. The Ly-α line was found to be by far the strongest emission over the wavelength range of the experiment (850-1250 Å). Such high intensities at relatively large heights in the corona was clear proof that the line was formed mostly by resonance between the coronal hydrogen and the high intensity Ly-α line emerging from the disk (Gabriel, 1971b).

Beckers & Chipman (1974) applied Doppler dimming techniques to the eclipse observations of 1970 March 7, primarily to derive the proton temperature in the corona from the profile of the Ly-α line. An instrument capable of observing the corona both in UV and in visible light without the aid of an eclipse was developed in the mid-1970's and was named the UltraViolet Coronagraph Spectrometer (UVCS) (Kohl et al., 1978). Integrated with the instrument was the White Light Channel (WLC) for electron density diagnostics. This advance in instrumentation made the prospect of remotely measuring outflow velocities and temperatures in the corona a reality. Three test rocket

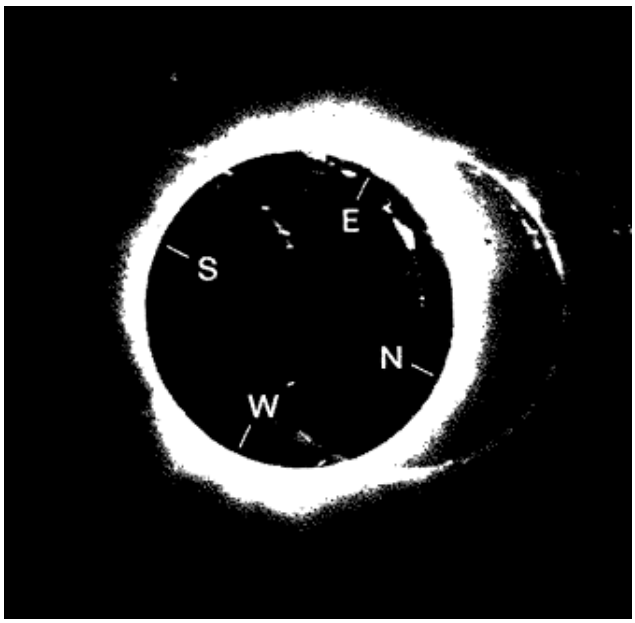

Figure 1.10: Image of the corona in Ly-α light made during a 1970 eclipse rocket flight. This is a slitless spectrum so we see the whole corona, with weaker lines dispersed to the right. The strength of the Ly-α image was proof that the line was formed by photo-excitation. From Gabriel (1971b).

flights between 1979 and 1982 acquired around 12 minutes of data. Although the primary objectives of these flights were the verification of the coronagraph and spectrometer design and performance, the good quality of the data inspired much analysis.

Ly-α data from the first flight made in 1979 April 13 showed a decreasing proton temperature with height in a quiet coronal region (Kohl et al., 1980). The analysis of data from the same flight by Withbroe et al. (1982) suggested a subsonic solar wind outflow below heights of $4R_{\odot}$ in the quiet coronal region. Conversely, data from the 1982 July 20 flight showed strong evidence of supersonic proton outflow in a coronal hole at a height of $2.1R_{\odot}$ (Kohl et al., 1984). The geometrical mapping of distant *in situ* solar wind velocity data from the Vela and Pioneer VI spacecraft to the inner corona had previously shown association between the fast solar wind and the position of coronal holes identified in X-ray observations (Krieger et al., 1973). The work of Withbroe et al. (1982) and Kohl et al. (1984) was direct evidence to support this. A more sophisticated analysis of the 1982 data by Strachan et al. (1993) showed an outflow velocity of 183 (+41,-101) km s^{-1} at a height of $1.5R_{\odot}$ in the coronal hole.

The theoretical framework for modern coronal UV spectroscopic diagnostics was established by Withbroe et al. (1982), Kohl & Withbroe (1982) and Noci et al. (1987). Withbroe et al. (1982)

considered mainly Doppler dimming and temperature diagnostics for the Ly-α line. The work of Kohl & Withbroe (1982) and Noci et al. (1987) showed that Doppler pumping, in particular pumping of the O VI 1037.6Å line by the nearby chromospheric C II 1037.0Å line, could be used to extend the diagnostic possibilities over a much larger range of outflow velocities. In addition, it was shown that the intensity ratio of a doublet line emitted by the same ion, such as the O VI 1031.9 and 1037.6Å doublet, could give far more robust estimates of outflow velocities. This improvement was due to using an intensity ratio as a diagnostic rather than an absolute intensity. This elegant approach lessened the dependence of the Doppler diagnostics on density and various atomic parameters.

Figure 1.11 shows advanced computations of the O VI 1032/1037 intensity ratio as a function of outflow velocity calculated for a height of $3R_\odot$ and various combinations of temperatures parallel ($T_\parallel$) and perpendicular ($T_\perp$) to the radial magnetic field (Li et al., 1998). Calculations such as these will be described and discussed in detail in chapter 2. This figure shows that an intensity ratio of 2.8 gives an outflow velocity of 94 km s^{-1} regardless of the choice of temperature.

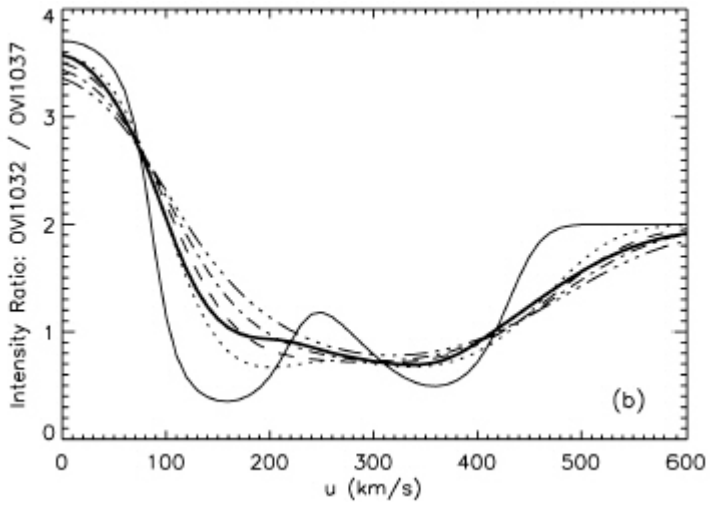

Figure 1.11: Computed O VI 1032/1037 intensity ratio as a function of outflow velocity at a height of $3R_\odot$. The various lines are for different combinations of temperatures parallel ($T_\parallel$) and perpendicular ($T_\perp$) to the radial magnetic field. The calculations include Doppler pumping of the O VI 1037.6 line by both CII 1037 and 1036.3 lines. From Li et al. (1998)

The years from 1993 to 1995 saw the launch of another three Spartan rockets armed with UVCS (Kohl et al., 1994). The success of these and the 1979-1982 rocket flights along with the exciting diagnostic prospects outlined by Noci et al. (1987) paved the way for the design of a second-generation UVCS. This instrument is part of the SOHO mission, a mission that has greatly advanced the field of solar physics.

A Brief Introduction to UVCS/SOHO

The UVCS/SOHO instrument has been observing the corona more or less continuously since 1996 and has made an enormous contribution to coronal and solar wind physics. A detailed description of the UVCS instrument is given in chapter 3 and in Kohl et al. (1995). Here we give a brief description only to facilitate subsequent discussions of the results obtained by UVCS.

UVCS makes measurements of the solar corona with high spectral and spatial resolution, at any latitude and between heights of 1.3 and $10R_\odot$. The instrument creates an artificial solar eclipse in UV light, blocking out the bright emission from the solar disk and allowing observation of the less intense light (by several orders of magnitude) from the extended corona. UVCS has observed approximately 37 spectral lines in the extended solar corona emitted by H I and ions of C, N, O, Mg, Al, Si, S, Fe, and Ni. Figure 1.12 shows spectral lines in the Ly-α and O VI channels, observed in a streamer on 1996 July 23-24, at a height of $1.5R_\odot$ (Raymond et al., 1997a).

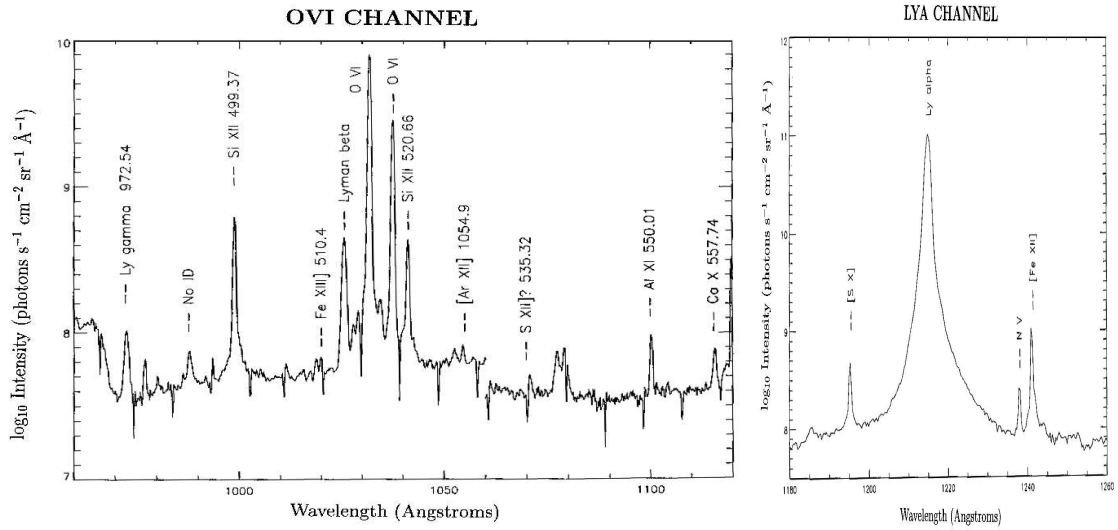

Figure 1.12: Identification of spectral lines from UVCS observations(from Raymond et al. (1997a)).

In practice, at heights greater than $\sim 1.5R_\odot$ or in regions outside streamers, many of the spectral lines shown in figure 1.12 are undetectable due to weakened intensity. The most important lines measured by UVCS are the O VI doublet at 1031.9 and 1037.6Å and the H Ly-α line at 1216Å. Generally these intense lines remain detectable in streamers out to heights of $8R_\odot$ but only to 3 or $4R_\odot$ in coronal holes, depending on observational parameters such as the width of the UVCS entrance slit or the time spent observing.

1.4 Streamers and Coronal Holes

Two distinct types of large-scale coronal structures or regions are described in this section: streamers and coronal holes. Particular emphasis is given to the relevant discoveries made by UVCS.

1.4.1 Streamers

Prior to the SOHO mission, little was known of coronal streamers except for their general high density and their shapes, given by white light images. Even today, no direct measurements of a streamer's magnetic structure in the inner corona have been made and the standard view, presented below, may be open to revision as advances are made in the observation of coronal magnetic fields using, for example, polarization of UV line emission (Fineschi et al., 1999).

Streamers are structures with densities around 3 to 10 times higher than surrounding regions (Schmidt, 1953; Pätzold et al., 1997). They are large and long-lived structures which, in radially filtered white light images, can be seen to extend from the base of the corona out to several solar radii. The LASCO C3 coronagraph has a field of view extending to a height of $\sim 30 R_{\odot}$ and, with a radial filter, some streamers can remain distinct throughout its field of view. In Carrington maps created from many consecutive LASCO C2 white light coronal images, streamers can often be seen moving gradually in latitude, as their projection on the plane of sky moves with solar rotation. Such maps show also that some streamers can remain stable for many solar rotations, even up to 10 rotations (Li et al., 2002).

Quiescent streamers are stable structures which emerge from regions of the coronal base which are not particularly magnetically active. Active region streamers are more dynamic and are associated with areas of enhanced magnetic flux and activity on the solar disk called active regions. These streamers may be composed of several open and closed magnetic field structures continually interacting with each other. The continuous emergence of sunspots and magnetic flux from active regions in the photosphere provides the long life spans of the active region coronal streamers (Li et al., 2002). During solar minimum, large quiescent streamers straddle the solar equator. At solar maximum, quiescent and active region streamers appear at any latitude and it often becomes difficult to identify isolated streamers in large streamer complexes, or to disentangle the complex line of sight in white light and UV data.

The exact magnetic structure of streamers is not known, but the chromosphere and low corona

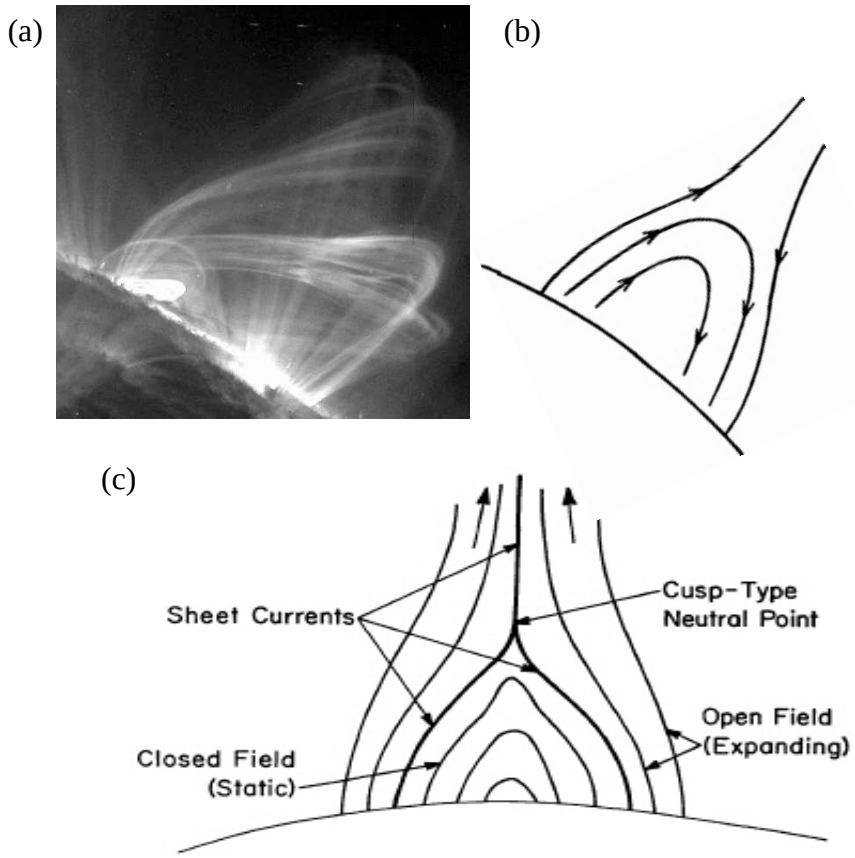

Figure 1.13: (a) Coronal loops at the solar limb seen in the 171Å pass band by TRACE. The image was taken on 1998 November 23. The loops are above active region AR8384. (b) Simple schematic showing the standard view of the polarity of magnetic field lines within a streamer (from Koutchmy & Livshits (1992), with minor edits). (c) Further detail of the standard view of streamer magnetic structure (from Pneuman & Kopp (1971)).

above active regions show a dominance of closed magnetic field structures. Figure 1.13a is a TRACE observation of closed magnetic structures above an active region. Closed magnetic structures such as these are often called coronal loops. The standard view of the magnetic structure within a streamer is shown schematically in figures 1.13b and 1.13c. This view suggests that all streamers are associated with a neutral current sheet which separates two flux tubes of opposite polarity (Sturrock & Smith, 1968; Pneuman & Kopp, 1971; Koutchmy & Livshits, 1992).

The slow speed solar wind is believed to originate in streamers (Gosling et al., 1981; Feldman et al., 1981). Gosling et al. (1981) compared *in situ* data from the Interplanetary Monitoring Platform (IMP) spacecraft* with inner coronal pB Carrington maps. Slow and high density wind flow patterns containing magnetic field reversals seen in the *in situ* data were interpreted as a signal of

*IMP-8 measured solar wind conditions from 1973 to 2001 - the third longest-lived operational spacecraft in history!

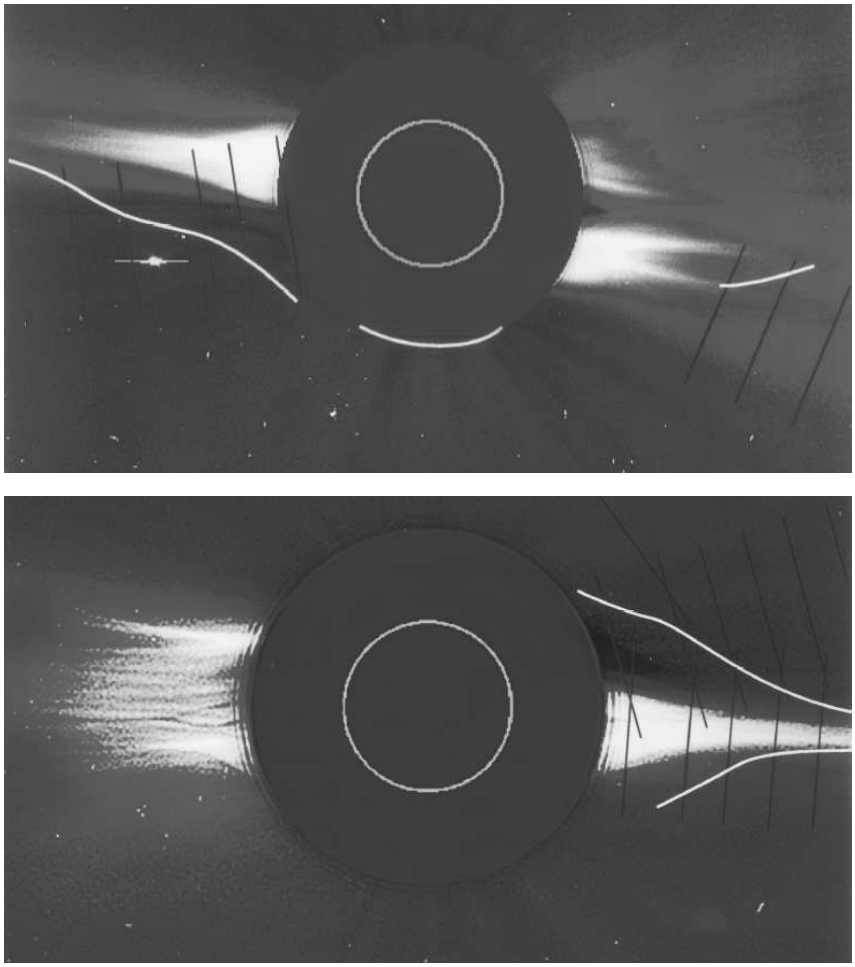

Figure 1.14: White light images of the corona taken with LASCO C2 on 1997 January 17 (*top*) and 1997 April 27 (*bottom*). Straight black lines are the positions of the UVCS field of view (FOV). The white contour marks the position where the intensity ratio of O VI 1032/1037 equals 2.8, or, equivalently, an outflow velocity of 94 km s^{-1} (from Habbal et al. (1997)).

the coronal streamer belt at 1 AU. More direct evidence of the source of the slow wind during solar minimum was provided by analysis of UVCS observations of the inner corona and Galileo radio Doppler scintillation measurements made during the solar conjunction of early 1997 by Habbal et al. (1997). Figure 1.14 shows how Habbal et al. (1997) used UVCS observations of the O VI 1032/1037 intensity ratio to map an isocontour of 2.8 across large regions of the solar minimum corona. The intensity ratio of 2.8 is roughly equivalent to an outflow velocity of 94 km s^{-1} (see the results of Li et al. (1998) in figure 1.11 of section 1.3). The isocontour follows the boundary between the equatorial streamers and surrounding regions, showing direct evidence of the streamers as sources of the slow wind. A similar analysis in Habbal et al. (2001a) showed slower outflow from a mid-latitude solar maximum streamer compared with neighboring regions.

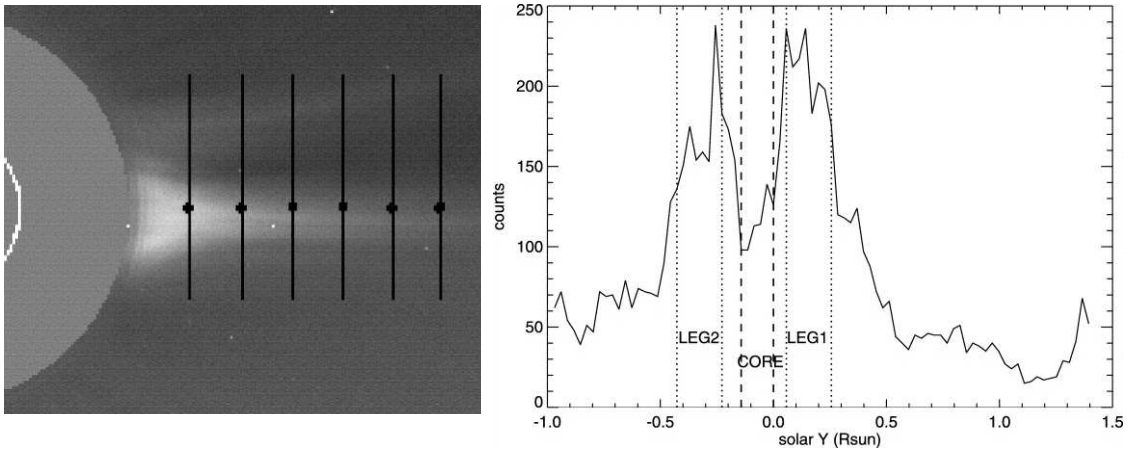

Figure 1.15: *Left* - Positions of UVCS FOV overlaid on a LASCO C2 white light image of 1996 October 12. *Right* - O VI 1032 photon counts as a function of position across the UVCS slit from the observation at height $2.6R_{\odot}$ (from Frazin et al. (2003)).

More detailed modelling of UVCS results has shown that O VI outflow velocity in solar minimum equatorial streamers is close to zero at heights below $\sim 3.5R_{\odot}$, then rises abruptly above this height before reaching values of $\sim$100 km s^{-1} at heights around $5R_{\odot}$ (Strachan et al., 2000, 2002). The results of Strachan et al. (2002) also shows the abrupt increase in outflow velocity at the boundary between solar minimum streamers and surrounding region, supporting the results of Habbal et al. (1997).

The profile of O VI intensity across quiescent streamers at low heights caused a surprise in early UVCS observations. The O VI intensity is lower in the center of many streamers (the core) than at their edges (the legs), in contrast to white light or H Ly-α intensity which peak in the streamer core. This phenomenon was reported very early in the SOHO mission by Raymond et al. (1997a) and Noci et al. (1997a). Figure 1.15 shows the dramatic depletion of O VI intensity in the core of a solar minimum equatorial streamer as seen by UVCS (Frazin et al., 2003). There are two differing views to explain this depletion. Noci et al. (1997b) suggest that if the proton flux in the streamer core decreases sufficiently, the force of the protons dragging the heavy ions into the solar wind by dynamical friction (for example, momentum transfer by Coulomb collisions (Geiss et al., 1970)) may drop below a threshold, resulting in a large depletion of oxygen. Raymond et al. (1997b) suggest that the heavy ions confined in the closed field of a streamer core are more susceptible to gravitational settling than the ions which flow along the open fields of streamer legs. For this process to occur, the heavy ions must be trapped in the streamer core for timescales of days. The

lack of a depleted core in active region streamers may result from projection (line of sight) effects, the maximum height of the core located below the observation height or a basic physical difference in streamer structure.

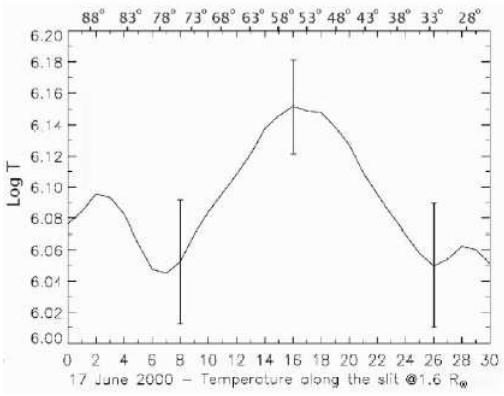

Figure 1.16: Electron temperature across a solar maximum streamer (from Bemporad et al. (2003)). The points with uncertainties are calculated from UVCS data. The line is calculated from electron density versus height calculations obtained from pB data assuming hydrostatic equilibrium.

Active regions appear bright in high-temperature emission lines, implying a high electron temperature. Feldman et al. (1998), using 1997 Solar Ultraviolet Measurements of Emitted Radiation (SUMER)/SOHO observations, found emission lines of high-ionization ions with peak temperatures of formation of 2 to 8 MK above a bright active region. Ko et al. (2002) reported high-temperature lines at heights of $1.6R_{\odot}$ in an active region streamer using UVCS observations, suggesting electron temperatures as high as 3 MK. Results such as these imply inner coronal electron temperatures in active region streamers considerably higher than seen in quiescent streamers and other coronal structures. Bemporad et al. (2003) derive electron temperatures directly from UVCS observations of the intensity of various Fe ion lines in a solar maximum streamer. Their results are shown in figure 1.16. The peak in electron temperature corresponds to the position of the streamer center, and is significantly higher than the temperature at the streamer edges.

In contrast to the relatively high electron temperature, heavy ion temperatures are lower in streamers compared to other coronal structures. Strachan et al. (2000) obtained O VI linewidths from UVCS observations of large regions of the corona made during the first Whole Sun Month (WSM) campaign conducted during solar minimum. Within approximately ±20° latitude to the streamer center, O VI $1/e$ linewidths are relatively constant, and vary only from ~100 to 150 km s^{-1} with height (1.6 to $3.0R_{\odot}$). Outside ±20°, the linewidth increases dramatically, to values higher

than 400 km s^{-1} at a height of $2.25R_{\odot}$.

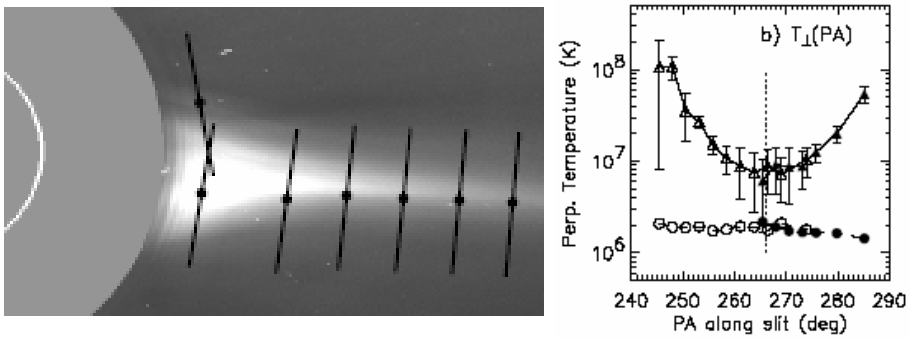

Figure 1.17: *Left* - LASCO C2 image of the corona taken on 1997 April 27, overlaid with the positions of UVCS fields of view. *Right* - O VI temperature across the 1997 April 27 solar maximum streamer calculated from the UVCS data at a height of 2.3 $R_{\odot}$ (from Strachan et al. (2002)). Triangles show the O VI temperature, circles show the Ly-α temperature. The straight vertical dotted line shows the position of the streamer center.

The O VI linewidth is more or less a direct measurement of the effective temperature* of O VI ions in a direction perpendicular to the solar radial and therefore perpendicular to the magnetic field, $T_{\perp}$. Figure 1.17 shows O VI and Ly-α effective $T_{\perp}$ across a solar minimum streamer at a height of $2.3R_{\odot}$, measured by UVCS and published by Strachan et al. (2002). O VI $T_{\perp}$ increases by a factor of 10 between the streamer center and surrounding regions, and is considerably higher than the hydrogen $T_{\perp}$. Hydrogen $T_{\perp}$ does not show a large contrast between the streamer and surrounding regions. Frazin et al. (2003) also provides evidence for a preferential heating of O VI in a solar minimum streamer , as well as showing evidence for an anisotropic O VI velocity or temperature distribution. That is, $T_{\perp}$ is shown to be greater than $T_{\parallel}$, the temperature parallel to the magnetic field. Anisotropic velocity distributions will be discussed further in the following section, within the context of coronal hole observations.

1.4.2 Coronal Holes

The identification of coronal holes as regions of low density in the inner corona was established in the 1970s with the advancement of EUV and X-ray observations of the inner corona (Munro & Withbroe, 1972) although they were first discovered during the 1950s in coronagraphic images of the 5303Å green line as long-lived regions of extremely low intensity (see Waldmeier, 1975). In

*Effective temperature is a temperature that includes the projection of outflow velocity along the LOS and other large-scale bulk motions of the plasma as well as the microscopic motions of particles.

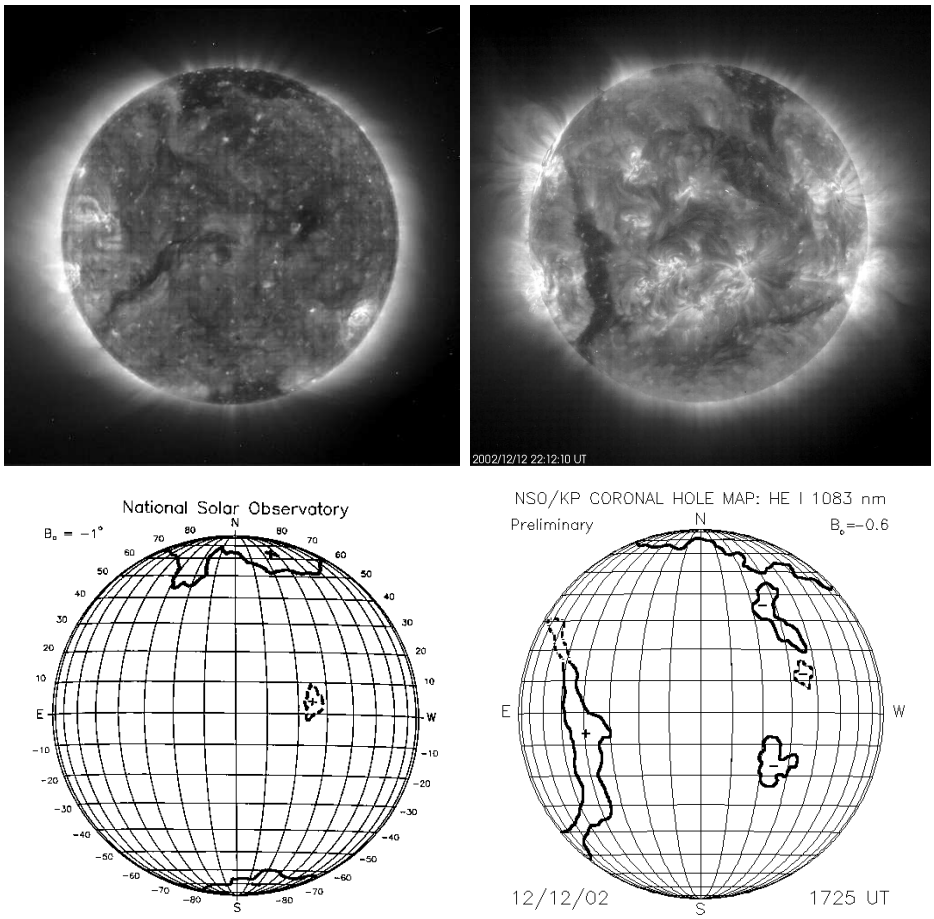

Figure 1.18: Coronal holes at 1996 December 12 during solar minimum (left column) and 2002 December 12 during solar maximum (right column). The top images are EIT 195Å observations. The bottom figures are coronal hole maps obtained from National Solar Observatory Kitt Peak observations of the Sun's disk in He 10803Å. The coronal holes outlined in the Kitt Peak maps can be seen clearly as dark regions in the EIT images.

X-ray or EUV images, coronal holes appear as dark regions. This can be seen in the EIT images of figure 1.18. Coronal holes only become apparent at heights of several Mm above the photosphere, with lower densities and electron temperatures than quiet or active regions. At solar minimum, seen in the left column of figure 1.18, large and long-lived coronal holes exist at the solar poles. At solar maximum, seen in the right column, coronal holes appear at all latitudes and are often smaller and lead shorter lives than the solar minimum polar coronal holes. A detailed review of coronal hole observations and models is given in Cranmer (2002).

In good quality white light images, coronal holes are far darker than streamers, and filaments of increased intensity called plumes can be seen extending radially within the holes. Plumes can be seen in the eclipse image of figure 1.4. Coronal holes are believed to be associated with regions of

open magnetic fields in the corona, and plumes are thought to be filaments of higher plasma density which follow open lines of strong magnetic flux. The configuration of plumes, and the general shape of the solar corona seen in radially filtered white light eclipse and coronagraph images have led to the association of coronal holes, in particular the solar minimum polar coronal holes, with super-radially expanding magnetic fields which follow the global dipole structure of the Sun's magnetic field. The left plot of figure 1.19 shows the standard model of solar minimum magnetic structure overlaid on a map of the corona created from UVCS synoptic observations of Ly-α intensity (Zangrilli et al., 2002). A growing body of evidence, summarized in Woo et al. (2004), is challenging some aspects of the accepted view of coronal magnetic structure. X-ray and white light measurements of the inner corona, compared with radio measurements by Ulysses have shown a radial expansion to the corona and to the boundaries of coronal holes (Woo & Habbal, 1999a; Woo et al., 1999b). Direct observations of inner coronal magnetic field direction, made by measuring the polarization of a Fe line during 1980, suggest the coexistence of a nonradial field associated with equatorial streamers, and a more pervasive radial magnetic field (Habbal et al., 2001b).

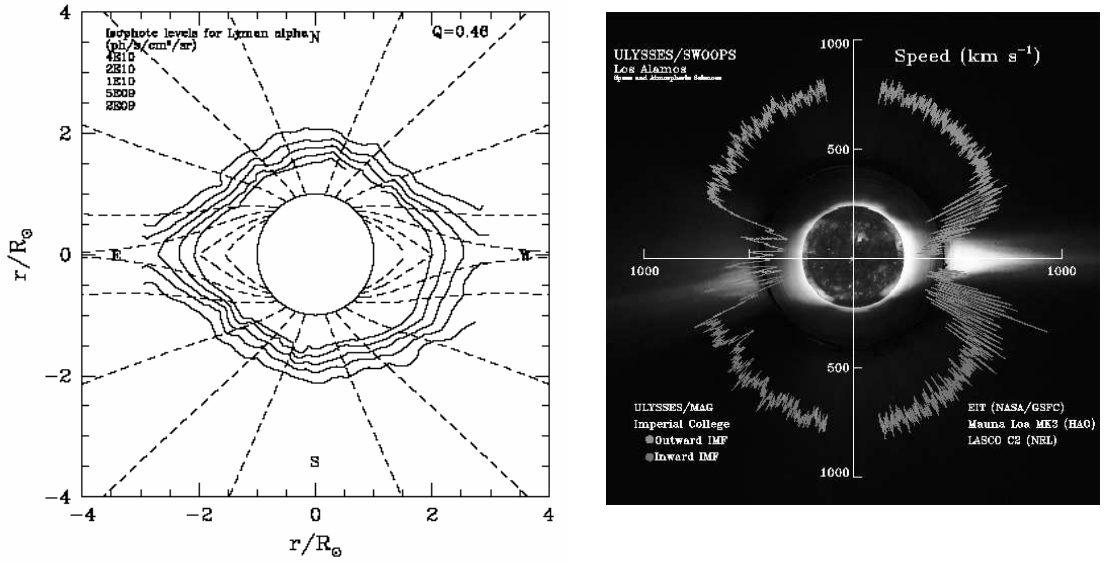

Figure 1.19: *Left* - the standard view of magnetic structure at solar minimum. The dashed lines show the basic dipole structure of the magnetic field model, expanding super-radially at the poles, and closed at the equators. The solid lines are isocontours of Ly-α intensity as obtained from UVCS synoptic observations. From Zangrilli et al. (2002). *Right* - solar wind speed measured along a whole polar orbit by the Ulysses spacecraft during solar minimum. The underlying images are composites of solar minimum observations made by EIT, the Mauna Loa MK III coronagraph and LASCO C2.

As mentioned in section 1.3, coronal holes were associated with the fast solar wind using a geo-

metrical mapping of distant *in situ* solar wind velocity data from the Vela and Pioneer VI spacecraft to coronal holes identified in X-ray observations (Krieger et al., 1973). The polar coronal holes as sources of the fastest solar wind was confirmed by *in situ* measurements made by the Ulysses spacecraft in a polar orbit during solar minimum (Balogh & Forsyth, 1998). A famous result is shown in the right plot of figure 1.19, where the solar wind speed measured by Ulysses is mapped over EIT and white light images of the solar minimum corona. Ulysses observed consistently fast wind over both poles, with slower and more variable wind over the equators. The latitudinal extent of the fast wind measured by Ulysses at large distances from the Sun is considerably larger than the latitudinal extent of the polar coronal holes in the inner corona. A super-radial expansion of the coronal holes would explain this, or the quiet mid-latitude coronal regions may also be sources of the fast solar wind.

A major result of UVCS coronal hole observations was the large linewidths of the O VI lines, with $T_\perp$ exceeding 300 MK at heights of $2R_\odot$ (Kohl et al., 1997). The top plot of figure 1.20 shows the profile of O VI observed in a 1996 June solar minimum north polar coronal hole at a height of $2.1R_\odot$. The profiles have a $V_{1/e}$ linewidth of around 500 km s^{-1}. Such linewidths were much larger than expected. O^{5+} ions in thermodynamic equilibrium with a 1 MK plasma, approximately consistent with T_e measured in coronal holes at low heights, should give linewidths of around 32 km s^{-1}. The bottom left and middle plots of figure 1.20 show several observed $V_{1/e}$ of Ly-α and O VI in solar minimum polar coronal holes (Kohl et al., 1998). The large O VI linewidths are not reflected in coronal hole Ly-α line profiles, which suggests that the large O VI widths can not be explained by turbulence. Ly-α linewidths are reflective of proton temperatures, and UVCS observations have shown that, in the case of temperatures perpendicular to the magnetic field, $T_{OVI} \gg T_p > T_e$.

Figure 1.21 shows observed and modelled O VI intensity ratios for a large north pole coronal hole observed by UVCS during 1997 January (Kohl et al., 1997). The observed intensity ratio reaches values below one at heights above $2.5R_\odot$, indicating Doppler pumping of the 1037 line. The modelled intensity ratios are calculated for a height of $3R_\odot$ and for different values of the width of the velocity distribution parallel to the radial magnetic field, or $w_\parallel$. The modelling shows clearly that a low $w_\parallel$ of less than 91 km s^{-1} is needed to achieve intensity ratios below one, compared with an observed $V_{1/e}$ of about 600 km s^{-1}. This is evidence of a large O VI temperature anisotropy in the directions parallel and perpendicular to the radial magnetic field. Evidence of O VI temperature

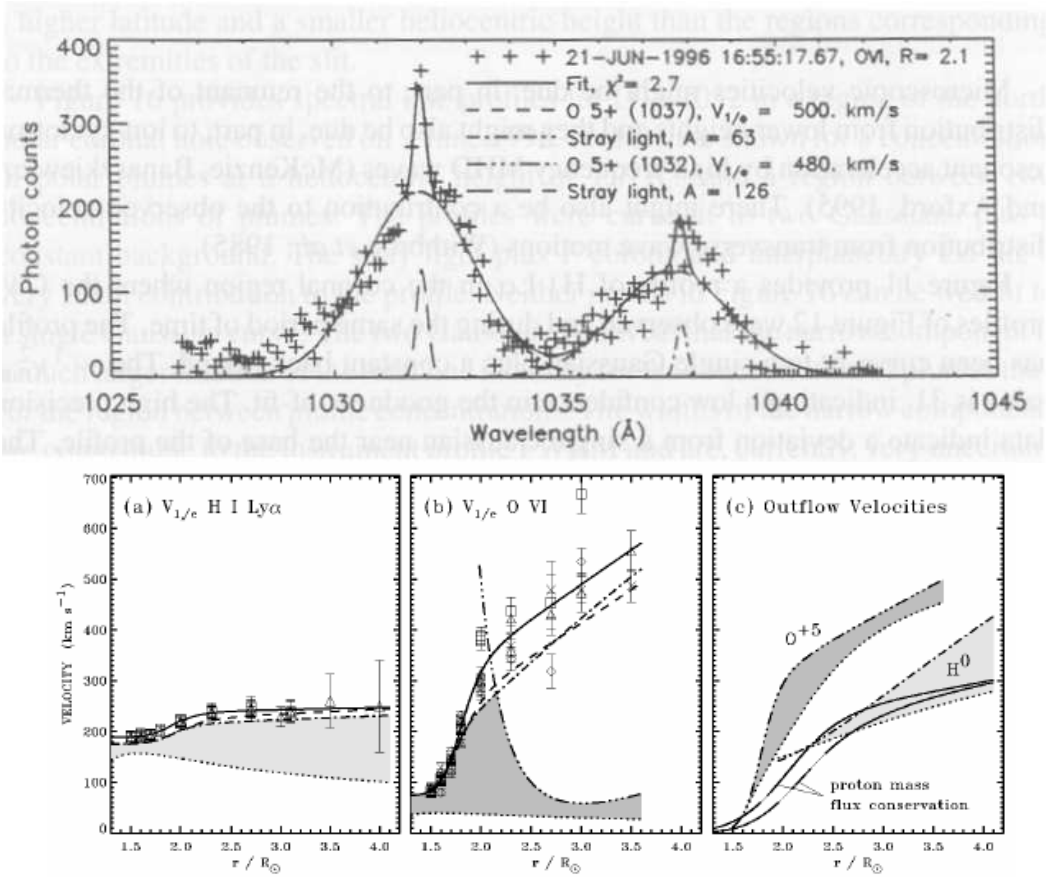

Figure 1.20: *Top* - profiles of O VI observed by UVCS in a 1996 June solar minimum north polar coronal hole at a height of $2.1R_{\odot}$. Crosses are data points, the solid line is a best fit to Gaussians, and the dashed and dashed-dotted lines show unwanted stray light contributions to the profiles. From Kohl et al. (1997). *Bottom* - several observed (a) Ly-α and (b) O VI $V_{1/e}$ linewidths versus height. Shaded areas show the limits of the most probable speeds in the direction parallel to the magnetic field, $w_{\|}$. (c) Derived O VI outflow velocity versus height. The shaded areas give the limits corresponding to the range of $w_{\|}$ in (a) and (b). From Kohl et al. (1998).

anisotropies $T_{\perp}/T_{\|}$ of order 10-100 have been consistently found from the comparison of UVCS coronal hole observations with model results (Kohl et al., 1997; Li et al., 1998; Kohl et al., 1998; Cranmer et al., 1999).

Evidence of $T_{OVI} \gg T_p > T_e$ and $T_{\perp}/T_{\|}$ of order 10-100 have led to a resurgence of interest in the modelling of ion cyclotron resonance, thought to be of major importance in the heating and acceleration of the fast wind. However, Raouafi & Solanki (2004) modelled realistic O VI intensity ratios using a simple isotropic temperature distribution. This was achieved by employing a super-radial expanding magnetic field and an electron density profile calculated by Doyle et al. (1999) from SUMER, LASCO and UVCS data. This result may have major implications on models for

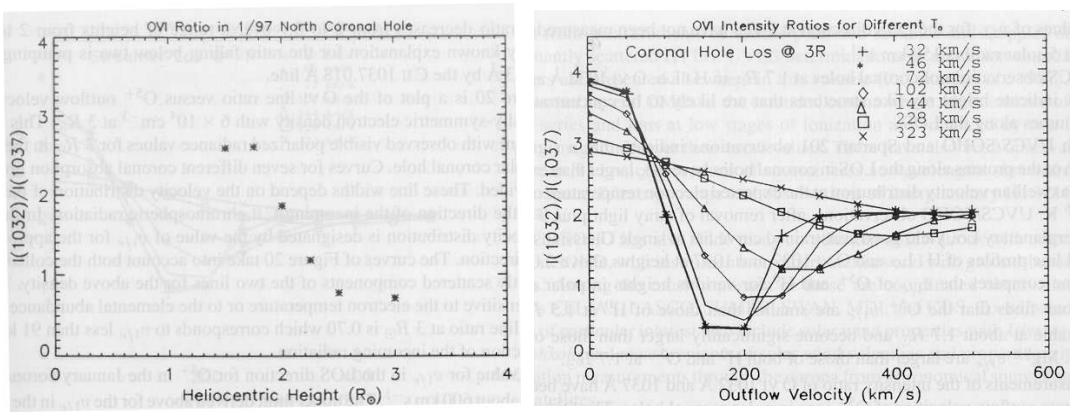

Figure 1.21: *Left* - observed intensity ratio for O VI 1032 to 1037 versus height from a north polar coronal hole during 1997 January. *Right* - modelled intensity ratio versus outflow velocity for a spherically symmetric corona with parameters constrained by the 1997 January north polar coronal hole observations. Curves are calculated for seven different widths of particle velocity distribution in a radial direction at a height of $3R_{\odot}$. The labeled values are $1/e$ velocities in a radial direction. From Kohl et al. (1997).

fast wind heating and acceleration.

1.5 Conclusions

This chapter has shown how advancements in observations, in particular UV observations of the last thirty years, have led to an enormous growth of our knowledge of the plasma properties of the solar corona. UVCS remains the only instrument capable of providing data in the acceleration region of the solar wind that can provide values of abundance, temperature and outflow velocity. The discovery of preferential heating and temperature anisotropy in coronal holes strongly suggests ion cyclotron heating in the corona. UVCS observations thus provide essential constraints on models of coronal heating and acceleration currently unavailable by any other means.

Chapter 2

The Coronal O VI Lines - Formation and Modelling

2.1 Introduction

In this chapter we examine the processes in the corona which form UV emission lines and how the O VI lines at 1031.9 and 1037.6Å are sensitive to bulk outflow velocity through Doppler dimming and pumping effects. Doppler dimming and pumping are the *raison d'être* of UVCS O VI observations and the effect is described and discussed in detail in this chapter.

The standard equations describing the formulation of collisional and radiative line intensities are introduced in section 2.2. Assuming a bi-Maxwellian velocity distribution of the emitting ions, the equations are transformed into an analytical form suitable for numerical computation in section 2.3. O VI Doppler dimming and pumping are described in section 2.4. Section 2.5 introduces the O VI intensity ratio as a diagnostic for bulk outflow velocity in the corona, and the intensity ratio is modelled as a function of outflow velocity and temperature anisotropy for typical coronal hole conditions. The sensitivity of the intensity ratio to various model parameters is examined in section 2.6. Brief conclusions are given in section 2.7.

2.2 Formation of UV Coronal Emission Lines

Figure 2.1 shows a general example of an UVCS spectrum containing the O VI doublet and the H Ly-α line. The O VI pair have their theoretical or reference line centers, λ_0, at 1031.91 and

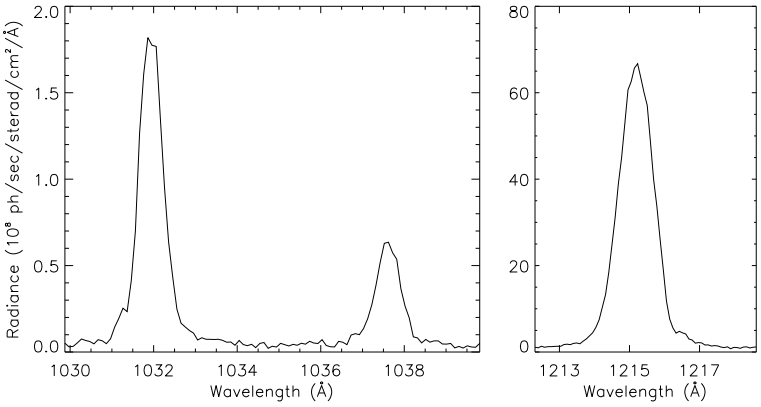

Figure 2.1: An example of the O VI doublet (*left*) and Hydrogen Ly-α (*right*) viewed by UVCS in a streamer at height $\sim$1.9 $R_\odot$, latitude $\sim$145°.

1037.61Å*. They are formed by two transitions of the O^{5+} ions: $2s^2S_{1/2} - 2p^2P_{3/2}$ for the 1032 line and $2s^2S_{1/2} - 2p^2P_{1/2}$ for the 1037 line. There are two main processes that contribute to the intensity of the O VI lines: collisional and radiative excitation. Therefore, the total intensity of an O VI line integrated over wavelength is

$$I = \int_{-\infty}^{\infty} \left(I_c(\lambda) + I_r(\lambda) \right) \, d\lambda \tag{2.1}$$

where $I_c(\lambda)$ and $I_r(\lambda)$ are the collisional and radiative intensities at wavelength λ respectively. Collisional and radiative processes will be discussed in detail in the following subsections. The Ly-α line at 1215.67Å is formed by a $1s-2p$ transition of neutral Hydrogen caused almost exclusively by radiative excitation (Gabriel, 1971b). Both radiative and collisional processes cause an excitation of the ion which is followed by de-excitation and the emission of a photon.

Figure 2.2 shows the geometry and coordinate system of a line of sight (LOS) in the corona, used extensively in the following sections. In the low density corona, the free path of a photon is effectively infinite therefore the intensity viewed by an observing instrument at a wavelength λ, $I(\lambda)$, is the emissivity, $j(\lambda, x)$, from a single point x in the corona at wavelength λ, integrated along an extended LOS:

$$I(\lambda) = \int_{-\infty}^{\infty} j(\lambda, x) \, dx \tag{2.2}$$

*For brevity, these are usually referred to as the 1032 and 1037 lines.

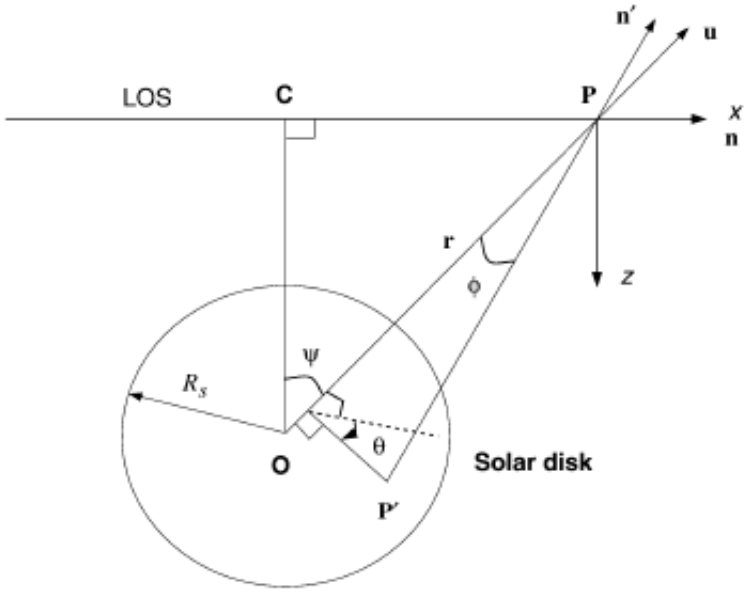

Figure 2.2: LOS geometry and coordinate system. The *x*-axis is parallel to the LOS, the *z*-axis points toward the Sun and the *y*-axis points out of the page. Point O is the center of the Sun, C is the point along the LOS closest to the Sun, P is any point along the LOS and P′ is any point on the Sun's disk. Ψ is the angle COP, ϕ is angle OPP′ and θ is the angle between the plane of the paper (*x*-*z* plane) and line OP′. **r** is the radial direction and **u** is the radial outflow velocity. **n** is the unit vector along the LOS and **n**′ is the unit vector along line PP′. From Li et al. (1998).

2.2.1 Collisional Component

Electrons in the corona have a temperature, T_e, of ~1×10^{6}K, equivalent to a $1/e$ velocity of ~5500 km s^{-1}. These energetic electrons collide with and excite ions in the corona causing subsequent de-excitation and emission of a photon. The collisional intensity at a certain wavelength viewed by an observer along a LOS can be written as:

$$I_c(\lambda) = \frac{1}{4\pi} \int_{-\infty}^{\infty} \int_{-\infty}^{\infty} q_c \, n_i \, n_e \; f(\boldsymbol{v}) \, \delta\left(\lambda_0 - \lambda + \frac{\lambda_0}{c} \boldsymbol{v.n}\right) \, dx \, d\boldsymbol{v}, \tag{2.3}$$

where q_c is the collisional excitation rate coefficient of the atomic transition (Withbroe et al., 1982), n_i is the ion density and n_e is the electron density. $\boldsymbol{n}$ is the unit vector along the LOS toward the observer therefore $\boldsymbol{v.n}$ is equal to v_x (see figure 2.2). $f(\boldsymbol{v})$ is the velocity distribution of the ions. The delta function in the integral over the velocity distribution in 2.3 selects only the ions that are at the correct velocity to emit at the observed wavelength λ, $\boldsymbol{v.n} = v_x = c\,(\lambda - \lambda_0)\,/\lambda_0$.

q_c varies with electron temperature (see section 2.6.2 of this chapter). Contained in the atomic

parameters of q_c, a $2s^2S_{1/2} - 2p^2P_{3/2}$ transition is twice as likely as a $2s^2S_{1/2} - 2p^2P_{1/2}$ transition, and the ratio of the O VI 1032 over 1037 collisional components is always close to 2.

2.2.2 Radiative Component

The radiative component of a coronal emission line is caused by photo-excitation of the ions by radiation from the chromosphere. The radiative intensity at a certain wavelength viewed by an observer along a LOS can be written as:

$$I_r(\lambda) = \frac{hB_{12}}{4\pi\lambda_0} \int_{-\infty}^{\infty}\int_{-\infty}^{\infty}\int_{-\infty}^{\infty}\int_{\omega} n_i \left[a + b\,(\boldsymbol{n}.\boldsymbol{n}')^2\right] I\,(\lambda', \omega) \times f(\boldsymbol{v})\,\delta\left(\lambda' - \lambda_0 - \frac{\lambda_0}{c}\boldsymbol{v}.\boldsymbol{n}'\right)\delta\left(\lambda_0 - \lambda + \frac{\lambda_0}{c}\boldsymbol{v}.\boldsymbol{n}\right) d\omega\, d\lambda'\, dx\, d\boldsymbol{v}, \tag{2.4}$$

where B_{12} is the Einstein coefficient and $I\,(\lambda', \omega)$ is the incident chromospheric radiation at wavelength λ' and from a point on the Sun's disk (Withbroe et al., 1982; Li et al., 1998). The integral over ω is the solid angle subtended by the Sun's disk as seen from point x. In the integral over the velocity distribution, the first delta function selects only those ions that have the correct velocity to be in resonance with the incident wavelength, $\boldsymbol{v}.\boldsymbol{n}' = c\,(\lambda' - \lambda_0)\,/\lambda_0$. The second delta function selects only those ions with $\boldsymbol{v}.\boldsymbol{n} = v_x = c\,(\lambda - \lambda_0)\,/\lambda_0$, that is, emitting at wavelength λ as seen by the observer. The incident radiation is along a particular direction $\boldsymbol{n}'$ and the function that describes the subsequent direction of the coronal emission is $\left[a + b\,(\boldsymbol{n}.\boldsymbol{n}')^2\right]$. This is called the scattering profile. For O VI 1032, a is 7/8 and b is 3/8; for O VI 1037 there is no preference for scattering direction therefore a is 1 and b is 0 (Noci et al., 1987). For H Ly-α, a is 11/12 and b is 3/12.

In the incident chromospheric spectrum, $I\,(\lambda', \omega)$, Ly-α and the O VI doublet have a strong presence. Radiative excitation is often called resonance scattering since $I\,(\lambda', \omega)$ is strongly peaked at the correct wavelengths to excite the ions in the corona. $I\,(\lambda', \omega)$ is dominated by collisional excitation therefore it has an O VI 1032 over 1037 intensity ratio of 2. In addition, since the excited O VI ions in the corona are twice as likely to occupy the $2p^2P_{3/2}$ state, the ratio of the O VI 1032 over 1037 radiative components in a corona *with no outflow* is ~4. This ratio changes if there is an outflow of the O VI ions. This effect will be described in section 2.4.

2.2.3 Other Mechanisms for Emission

Other contributions to UV coronal line intensities are (Gabriel, 1971b):

- Thomson scattering of chromospheric radiation from coronal electrons
- Rayleigh scattering of chromospheric radiation from coronal ions
- F-corona emission - scattering of chromospheric radiation from coronal dust

These contributions are weaker than the collisional and radiative contributions by many orders of magnitudes. Of these, Thomson scattering of the chromospheric lines is the most prominent. It gives a contribution with a very wide profile. For Ly-α, it has a $1/e$ width at the order of 30Å for typical coronal temperatures (Withbroe et al., 1982). In current observations, this contribution is indistinguishable from the background.

2.3 Computing the O VI Intensities

Given an appropriate coronal ion velocity distribution, analytical solutions may be found to the equations of collisional and radiative excitation (Withbroe et al., 1982; Li et al., 1998). The analytical solutions give greater efficiency in the numerical computation of emission lines.

2.3.1 The Ion Velocity Distribution

The first consideration in computing the O VI lines from equations 2.3 and 2.4 is the velocity distribution, $f(\boldsymbol{v})$. A common choice is a bi-Maxwellian distribution:

$$f(\boldsymbol{v}) = \left(\frac{m}{2\pi k T_{\parallel}}\right)^{1/2} \frac{m}{2\pi k T_{\perp}} \exp\left[-\frac{m}{2kT_{\parallel}}(v_{\parallel} - u)^2 - \frac{m}{2kT_{\perp}} v_{\perp}^2\right], \tag{2.5}$$

where $T_{\parallel}$ and $T_{\perp}$ are the temperatures parallel and perpendicular to the solar radial direction, $v_{\parallel}$ and $v_{\perp}$ are the particle velocities parallel and perpendicular to the radial direction and u is the outflow speed, assumed to be radial. The velocity profile is therefore symmetric around a radial axis from the Sun, this being a reflection of conditions in the corona since the magnetic field can be assumed to be mostly radial. The bi-Maxwellian distribution allows us to introduce a temperature anisotropy parallel and perpendicular to the magnetic field.

2.3.2 Analytical Solutions

Substituting the bi-Maxwellian form for $f(\boldsymbol{v})$ into equation 2.3, the delta function can be used to transform the collisional velocity integration,

$$F_c = \int_{-\infty}^{\infty} f(\boldsymbol{v})\delta\left(\lambda_0 - \lambda + \frac{\lambda_0}{c}\boldsymbol{v.n}\right)d\boldsymbol{v},$$

into the analytical expression:

$$F_c = \frac{1}{(\alpha_{\parallel}\alpha_{\perp}A_c)^{1/2}} \exp\left[\frac{\cos^2\psi}{A_c}\left(\frac{[\beta\sin\psi - u]}{\alpha_{\parallel}} - \frac{\beta\sin\psi}{\alpha_{\perp}}\right)^2 - \frac{(\beta\sin\psi - u)^2}{\alpha_{\parallel}} - \frac{\beta^2\cos^2\psi}{\alpha_{\perp}}\right], \qquad (2.6)$$

where $\alpha_{\parallel} = \dfrac{2kT_{\parallel}}{m}$, $\alpha_{\perp} = \dfrac{2kT_{\perp}}{m}$, $A_c = \dfrac{\cos^2\psi}{\alpha_{\parallel}} + \dfrac{\sin^2\psi}{\alpha_{\perp}}$ and $\beta = c(\lambda - \lambda_0)/\lambda_0$.

Following Li et al. (1998), the same approach can be applied to the radiative velocity integration of equation 2.4:

$$F_r = \int_{-\infty}^{\infty} f(\boldsymbol{v})\,\delta\left(\lambda' - \lambda_0 - \frac{\lambda_0}{c}\boldsymbol{v.n'}\right)\delta\left(\lambda_0 - \lambda + \frac{\lambda_0}{c}\boldsymbol{v.n}\right)d\boldsymbol{v},$$

to derive:

$$F_r = \frac{A_r^{-1/2}}{\pi\sqrt{\alpha_{\parallel}}\alpha_{\perp}} \exp\left[-\frac{1}{\alpha_{\parallel}}\left(\beta_1\sin\psi - u + \frac{\beta_2 d_z\cos\psi}{d_y^2 + d_z^2}\right)^2\right] \times$$
$$\times \exp\left\{-\frac{1}{\alpha_{\perp}}\left(\beta_1\cos\psi - \frac{\beta_2 d_z\sin\psi}{d_y^2 + d_z^2}\right)^2 - \frac{\beta_2^2 d_y^2}{\alpha_{\perp}(d_y^2 + d_z^2)} + \Delta\right\}, \qquad (2.7)$$

where

$$\Delta = \frac{d_y^2\cos^2\psi}{\alpha_{\parallel}^2\alpha_{\perp}^2 A_r}\left[\frac{\beta_2\, d_z\cos\psi(\alpha_{\perp} - \alpha_{\parallel})}{d_y^2 + d_z^2} + \alpha_{\perp}(\beta_1\sin\psi - u) - \alpha_{\parallel}\beta_1\sin\psi\right]^2.$$

β_1 and β_2 are given by

$$\beta_1 = \frac{c}{\lambda_0}(\lambda - \lambda_0), \qquad \beta_2 = \frac{c}{\lambda_0}[(\lambda_0 - \lambda') - d_x(\lambda_0 - \lambda)]$$

and A_r by

$$A_r = \frac{d_z^2}{\alpha_\perp} + d_y^2\left(\frac{\cos^2\psi}{\alpha_\parallel} + \frac{\sin^2\psi}{\alpha_\perp}\right).$$

d_x, d_y and d_z are given by

$$d_x = -\sin\phi\cos\theta\cos\psi + \cos\phi\sin\psi,$$

$$d_y = -\sin\phi\sin\theta$$

$$d_z = -\cos\phi\cos\psi - \sin\phi\cos\theta\sin\psi.$$

2.3.3 The O VI Spectral Line Program

A line emission program is readily constructed from the analytical solutions 2.6 and 2.7. The code utilised in this work is written in the Interactive Data Language (IDL). It accepts a set of coronal parameters (for example, electron and ion density, electron and ion temperature) and calculates emission along a LOS through the corona for the relevant wavelength ranges. The program makes full use of the array-manipulating capabilities of IDL to minimise the time spent looping through integrations. The time for computing the two O VI line profiles for a typical grid size of 30 wavelengths each line, 100 LOS bins, 20 ϕ angles, 20 θ angles and 40 incident wavelengths for each line is $\sim 5s$ on a standard desktop PC.

2.4 Doppler Dimming and Pumping

Doppler dimming is caused by the outflow speed of the O VI ions in the corona. An increase in outflow decreases resonance with the incident chromospheric O VI lines resulting in a decrease in the radiative coronal emission. Figure 2.3 shows a part of the chromospheric spectrum containing

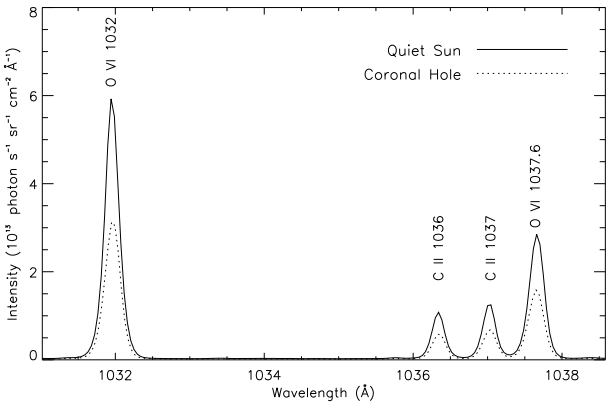

Figure 2.3: Chromospheric spectrum containing the O VI and C II doublet. This spectrum is obtained from the accumulation of quiet solar disk (solid line) and coronal hole (dotted line) observations by SUMER/SOHO (Curdt et al., 2001). There is no correction here for widening of the profiles by the spectrometer.

the O VI doublet. If the coronal O VI ions have no outflow, they are excited by the peak wavelengths of the chromospheric O VI doublet. With outflow u, they see the chromospheric spectrum redshifted by $u\lambda/c$. At high outflow, resonance is lost and the radiative excitation drops to extremely low levels. The rate of dimming with increasing outflow velocity depends critically on the width of the velocity distribution of coronal ions in the solar radial direction, characterized by the parallel temperature, $T_{\|}$. A low $T_{\|}$ increases the sensitivity of the dimming to outflow speed. The left panel of figure 2.4 shows Doppler dimming of the O VI 1032 coronal intensity as a function of outflow speed for three values of $T_{\|}$. The dimming has been calculated using a quiet Sun chromospheric spectrum. At a $T_{\|}$ of $10^6 K$ the 1032 intensity has dimmed to 5% at an outflow speed of $\sim$ 100 km s^{-1}. At a $T_{\|}$ of $10^8 K$ an outflow of $\sim$ 600 km s^{-1} is needed to achieve the same dimming.

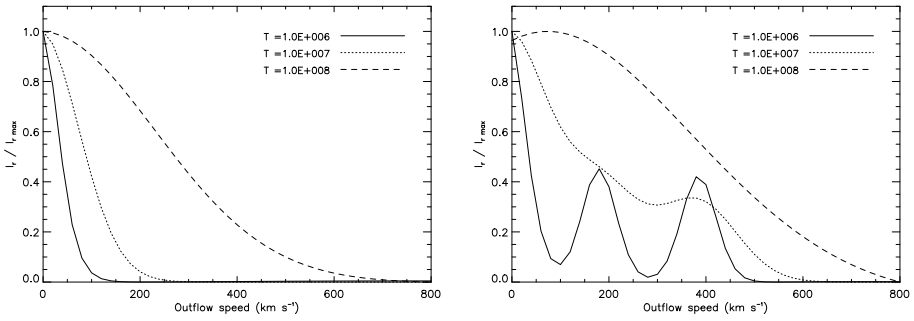

Figure 2.4: *Left* - Doppler dimming of the O VI 1032 line as a function of outflow velocity for 3 different ion $T_{\|}$. The lines were modelled using a plane of sky (POS) calculation at a height of $3R_{\odot}$ with an isotropic temperature distribution ($T_{\|} = T_{\perp}$). *Right* - the same for O VI 1037.6.

Two chromospheric C II lines can be seen in figure 2.3. Since these are close to the O VI 1037.6

line and are at shorter wavelengths (1037.02 and 1036.34 Å), they can resonate with the coronal O VI ions at certain ranges of outflow velocities. This is called Doppler pumping and its effect can be seen in the right panel of figure 2.4 for three different ion temperatures. Following the plot for a temperature of $10^6 K$, since this is the most sensitive to dimming and pumping, the 1037 line is at first dimmed due to the drop of resonance with its own chromospheric incident line. At an outflow of $\sim$ 100 km s^{-1} the O VI ions start to resonate with the closest C II line at 1037Å. This pumping reaches a maximum at $\sim$ 180 km s^{-1}. This speed translates into a redshift of 0.6Å which is the separation between the O VI and C II lines. The same effect repeats for the second C II line, peaking at an outflow of $\sim$ 400 km s^{-1}.

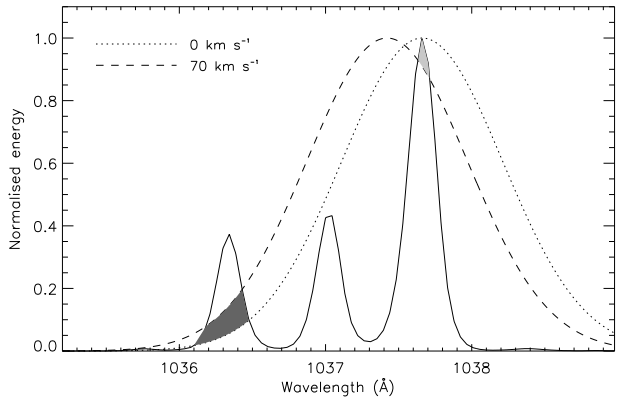

Figure 2.5: Comparison of chromospheric spectrum (solid line) and coronal velocity distribution at two outflow speeds which illustrates the increase in 1037 intensity between 0 (dotted line) and 70 (dashed line) km s^{-1} at a temperature of $10^8 K$. The coronal velocity distributions are translated into angstroms. The chromospheric spectrum is normalized to unity at the peak of the O VI 1037 line. The coronal velocity distributions are also normalized to unity. At zero outflow, the coronal velocity distribution is centered at the chromospheric 1037.6 line. Increasing outflow shifts this distribution to the left. The lightly shaded region at the peak of the O VI 1037 line represents the loss in resonance between 0 and 70 km s^{-1}. The darker shaded region shows the gain.

An interesting effect is seen in figure 2.4 for O VI 1037 at a temperature of 10^8K, where the intensity *increases* by a few percent between 0-70 km s^{-1}, a velocity range where we see the steepest dimming at lower temperatures. This can be understood best by looking at figure 2.5, which shows the normalized velocity distribution of the O VI ions for outflow velocities of 0 and 70 km s^{-1}, translated into units of angstroms and overlaid on the chromospheric spectrum. The velocity distributions are so wide that they cover most of the 3 chromospheric lines. The lightly shaded region at the peak of the O VI 1037 line represents the loss in resonance between 0 and 70 km s^{-1}. The darker shaded region shows the gain. There is a net gain in resonance so the intensity of the

coronal line is increased.

2.5 Outflow Velocity and the Intensity Ratio of the O VI Doublet

Using the Doppler dimming technique, the intensity ratio of the O VI doublet can be used as evidence of bulk outflow velocity of O VI ions from the Sun (Kohl & Withbroe, 1982; Withbroe et al., 1982; Noci et al., 1987; Li et al., 1998). At low outflow velocities, both lines are radiatively dominated, and the 1032/1037 ratio is usually between 3 and 4. At very high velocities, the radiative component of both lines is Doppler dimmed and the lines are collisionally dominated, giving a ratio close to 2. In between these extremes of outflow, the ratio can drop to values well below 2, as the 1037 line is pumped while the 1032 line continues to dim. A more detailed analysis requires a choice of coronal parameters.

2.5.1 Model Parameters

Let us consider here some conditions typical of a polar coronal hole (PCH). The following calculations are made using a solar wind model whose parameters vary along the LOS maintaining spherical symmetry. Using equations 2.3 and 2.4, a bi-Maxwellian velocity distribution and the parameters described below, we obtain the intensity ratio as a function of outflow velocity at heights of 2, 3 and 4 $R_\odot$, with 5 different temperature anisotropies modelled for each height: $T_\parallel = 0.01T_\perp$, $T_\parallel = 0.1T_\perp$, $T_\parallel = 0.5T_\perp$, $T_\parallel = T_\perp$ (isotropic) and $T_\parallel = 2T_\perp$. In all cases, temperatures are constrained not to drop below the electron temperature. In the calculations, the LOS extends to both directions from the minimum height, ρ (= 2, 3 or 4 $R_\odot$), until a height of $\rho \times 1.5$ is reached. At these extremes of the LOS, the emission is small compared to that from points closer to the Sun due primarily to the sharp drop in density.

The incident chromospheric spectrum is obtained from the one shown in figure 2.3 for the quiet Sun (Curdt et al., 2001). Using this observed spectrum directly would be incorrect since the line profiles are slightly widened by the SUMER instrument. By fitting the spectrum to a Gaussian for each line and a constant background we can correct for the increase in linewidth using standard SUMER software and reconstruct a corrected spectrum. The fitting is done with a Levenberg-Marquardt least-squares fit. Corrected linewidths of 0.11 and 0.12 Å are measured for the O VI 1032 and 1037 lines respectively, 0.09 Å for both the C II lines. These are slightly wider than the

0.1 (O VI) and 0.07 (C II) Å widths measured by Noci et al. (1987) from Skylab observations. The sensitivity of the O VI intensity ratio to incident spectrum will be discussed in a following section. It should be noted that the incident lines obtained from the SUMER solar atlas are shifted to their theoretical line centers prior to modelling.

Electron density is obtained from a simple radial profile calculated by Doyle et al. (1999) to fit PCH N_e measurements from SUMER spectral data and pB measurements from the white light channel (WLC) on UVCS and LASCO C2:

$$N_e = \frac{1 \times 10^8}{r^8} + \frac{2.5 \times 10^3}{r^4} + \frac{2.9 \times 10^5}{r^2}. \tag{2.8}$$

Electron temperature is kept fixed at all heights at 1.2×10^6 K. Ion density is calculated from the electron density using the ionization equilibria of Mazzotta et al. (1998) and the oxygen abundances of Feldman et al. (1992), both tabulated in the Chianti atomic database. Ion velocity is kept constant along the LOS.

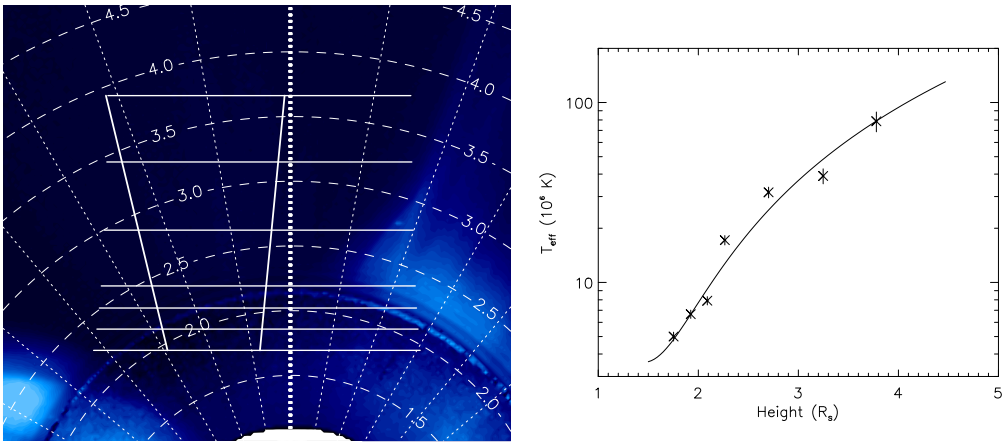

Figure 2.6: Left - UVCS field of view (FOV) positions during 2002/05/27-28 overlaid on a LASCO C2 and Mauna Loa MK IV white light image. Slit bins are integrated at each FOV between the two solid lines. Gaussian fitting of the resulting O VI 1032 profiles lead to the temperatures given in the right panel. The solid line is an error-weighted fit of a second-degree polynomial to the observed temperatures which are shown as crosses with uncertainties.

We use a $T_\perp$ for the coronal ions obtained directly from UVCS observations of O VI 1032 linewidth in a Northern PCH. The FOV positions of the observation sequence is shown overlaid on a LASCO C2 and Mauna Loa MK IV white light image in figure 2.6. The actual O VI linewidths contain contributions from microscopic, macroscopic and outflow velocities along the LOS therefore are labeled as T_{eff}, an effective temperature, in figure 2.6. This approximate radial profile of

temperature is sufficient for this discussion and a more rigorous approach will be used in chapter 4 where the surplus T_{eff} due to outflow velocity will be removed using an iterative method. See section 3.6 of chapter 3 for a discussion of T_{eff}.

2.5.2 Results and Discussion

Results are shown in figure 2.7. The profile of intensity ratio with increasing outflow velocity is similar at all heights although with increasing height the profile becomes more exaggerated. This can be explained by the general balance of collisional and radiative components with height. A stronger collisional component at low heights restricts the sensitivity of the intensity ratio to outflow velocity. It is also apparent that the sensitivity increases with decreasing parallel temperature. An anisotropy of $T_{\parallel} = 0.5T_{\perp}$ allows a minimum intensity ratio of 1 at $3R_{\odot}$ and 1.1 at $4R_{\odot}$. To drop below unity, an anisotropy of $T_{\parallel} < 0.5T_{\perp}$ is needed. Kohl et al. (1997) give intensity ratios of ~ 0.7 from UVCS observations at heights of $3R_{\odot}$ in a solar minimum PCH. This is evidence that a strong $T_{\parallel} < T_{\perp}$ anisotropy can exist in coronal holes (Kohl et al., 1997; Li et al., 1998).

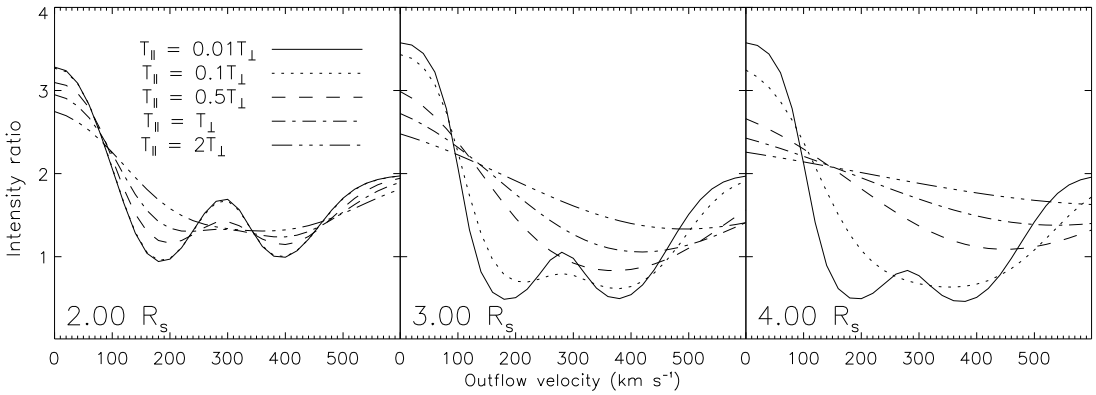

Figure 2.7: Intensity ratio as a function of outflow velocity at various heights and temperature anisotropies (see main text).

The intensity ratios measured for the coronal hole observations shown in figure 2.6 are shown in figure 2.8. The ratio of 1.15 ± 30% at $4R_{\odot}$ suggests an anisotropy of $T_{\parallel} \leq 0.5T_{\perp}$. This is far less conclusive than the values of 0.7 measured by Kohl et al. (1997). However, the profile of observed ratio with height shows the distinct double dip which is unique in the modelled ratios for $T_{\parallel} \leq 0.1T_{\perp}$. More definitive conclusions would require more rigorous constraints on the solar wind model, for example, using electron density measured in the same region and at the same time as the UVCS observations. Such improvements are made in following chapters. This section has given a

demonstration of the value of the intensity ratio as a diagnostic tool.

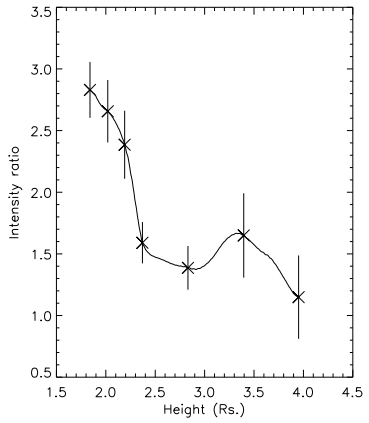

Figure 2.8: Intensity ratio for the 2002/05/27-28 coronal hole observations shown in 2.6

2.6 Sensitivity of the O VI Intensity Ratio to Various Parameters

In this section we investigate the sensitivity of the O VI intensity ratio to certain input parameters. It is important to explore the model in such a way in order to draw any conclusions from the observations.

2.6.1 Chromospheric Spectrum

Figure 2.9 shows in greater detail the SUMER spectrum shown in figure 2.3. The reconstructed spectrum after correcting for the instrument broadening, described in the previous section, is also shown. Table 2.1 compares the values obtained by Noci et al. (1987) from quiet Sun measurements obtained from Skylab and the SUMER reconstructed spectrum for quiet Sun and coronal holes. Let us first compare the quiet Sun values. Due to low spectral resolution in the Harvard spectrometer aboard Skylab, the O VI 1037.6 and C II lines are blended. The value of 152.5 for the O VI 1037.6 intensity was calculated directly as half the 1032 intensity since the chromospheric lines are formed by collisional processes. The C II 1037 intensity was then obtained by subtracting the O VI 1037.6 intensity from the blended lines. The SUMER atlas shows a ratio of 2.04 for the O VI lines. The C II lines have a ratio (1036.3/1037) of 0.82, close to the value of 0.84 given by Warren et al. (1997).

The intensities measured from SUMER for O VI in the quiet Sun are considerably lower than those measured by Noci et al. (1987). The coronal hole measurements are very low as expected

Table 2.1: Measurements of Chromospheric O VI and C II. I is in ergs s^{-1} cm^{-2} sr^{-1} and the $1/e$ halfwidths and λ_{ref} are in Å

		SUMER atlas - QS		SUMER atlas - CH		Noci et al. (1987)	
Ion	λ_{ref}	I	$\Delta\lambda$	I	$\Delta\lambda$	I	$\Delta\lambda$
O VI	1031.91	270.0	0.11	156.9	0.13	305	0.1
O VI	1037.61	132.3	0.12	77.0	0.13	152.5	-
C II	1037.02	49.9	0.09	28.6	0.10	52	0.07
C II	1036.34	40.9	0.09	23.7	0.10	-	-

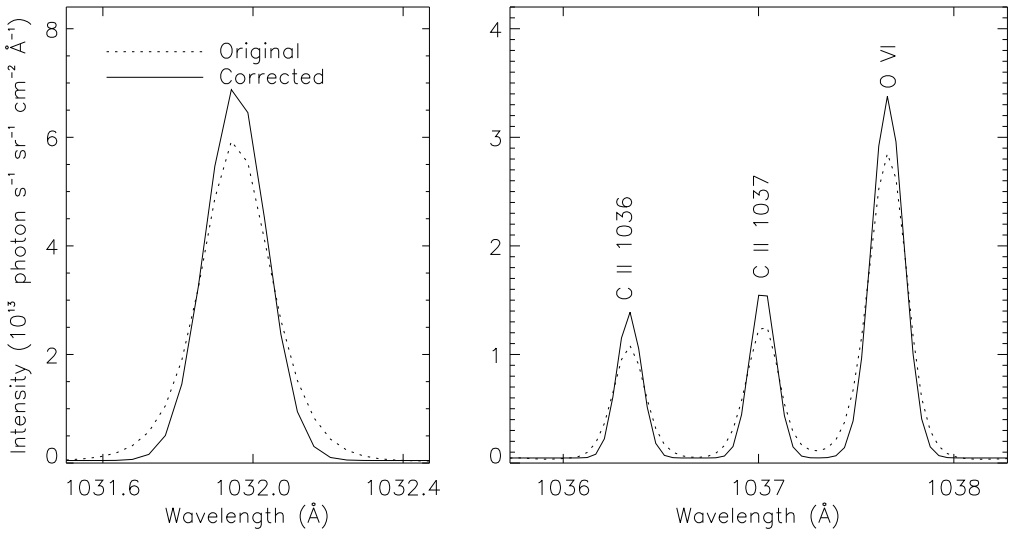

Figure 2.9: Greater detail of the spectrum shown in figure 2.3. O VI 1032 is in the left panel, O VI 1037.6 and the C II doublet in the right. The reconstructed spectrum with the correction for instrument broadening is the solid line.

- approximately half those measured by Noci et al. (1987). Figure 2.10 shows the sensitivity of intensity ratio to the choice of incident spectrum. The maximum difference between results for the SUMER quiet Sun and Noci et al. (1987) is 10% at an outflow of 280 km s^{-1}, with an average difference of only 4%. Compared to the quiet Sun, the coronal hole result has a less exaggerated profile as the radiative components of both lines are reduced with the less intense chromospheric radiation. The largest difference is 45% near 180 km s^{-1} with an average difference of 20%. It is reassuring that the differences between Noci et al. (1987) and the SUMER solar atlas spectrum lead to so little difference in intensity ratio results. Conversely, the different results obtained from using the coronal hole spectrum indicate that care must be taken in the modelling of UVCS coronal hole observations. In particular, a careful computation of O VI emission from a large solar minimum PCH should incorporate the coronal hole spectrum as part of the incident radiation from the

chromosphere.

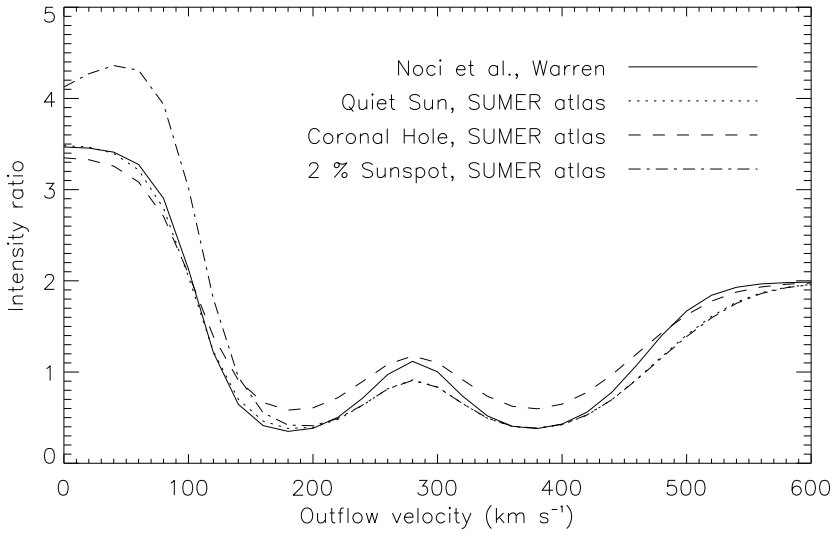

Figure 2.10: Intensity ratio as a function of outflow velocity calculated for different chromospheric incident spectra. The calculations were conducted for the same set of parameters as described in the previous section for figure 2.7 at a height of $3R_\odot$ with a temperature anisotropy of $T_\parallel = 0.01T_\perp$.

The O VI chromospheric lines from sunspots are more intense than the quiet Sun lines by a factor of 60 or more, while the intensity of the C II lines remain similar to their quiet Sun values. According to the SUMER solar atlas, the intensity ratio of the peaks of the chromospheric O VI lines is also changed from 2 to over 2.5. Since the C II emission remains similar to that of the quiet Sun, the intensity ratio of the coronal emission is only affected by sunspots at low outflow velocity. Once a certain outflow speed is reached, the coronal O VI falls out of resonance with the chromospheric O VI radiation, and the intensity ratio behaves much as it does with a quiet Sun chromospheric incident radiation. If we model the disk radiation with only a small contribution from sunspots, the coronal intensity ratio at low outflow speeds can achieve values higher than 4. This can be seen in figure 2.10, where intensity ratio is calculated using a quiet Sun chromospheric spectrum with a 2% contribution from sunspot emission. The intensity ratio increases from 4.1 to 4.4 between outflow velocities of 0 and 40 km s^{-1}. Above 180 km s^{-1} the profile closely follows that of the quiet Sun. It will be shown in chapter 4 that a contribution from sunspots has great implications on the modelling of O VI conditions in a streamer.

2.6.2 Electron Temperature and Ion Abundance

Electron temperature is included in the calculation of the collisional excitation coefficient of q_c and in the calculation of O VI abundance. Figure 2.11 shows the behavior of q_c and O VI abundance as a function of T_e along with a comparison of intensity ratio profile for two different T_e. The intensity ratio is only slightly affected by the large difference in T_e. This small difference arises from the change in q_c and not from the change in abundance. Both the collisional and radiative components (equations 2.3 and 2.4) contain the same term for ion density therefore the intensity ratio is totally insensitive to changes in that density.

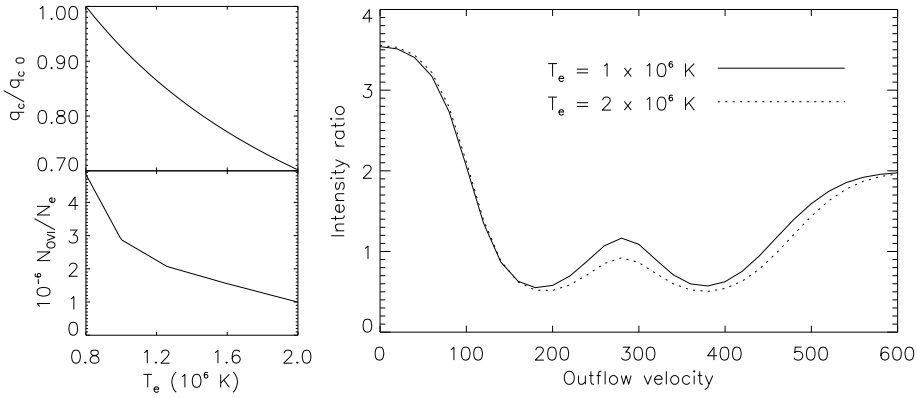

Figure 2.11: *Left* - q_c (top) and ion density relative to electron density (bottom) as a function of T_e. *Right* - Intensity ratio as a function of outflow velocity calculated for 2 different T_e. The calculations were conducted for the same set of parameters as described in the previous section for figure 2.7 at a height of $3R_\odot$ with a temperature anisotropy of $T_\parallel = 0.01T_\perp$.

2.6.3 Electron Density

The collisional component has a direct dependence on electron density. Figure 2.12 shows the intensity ratio profile for two different N_e. The first value for N_e is typical for the given height in large coronal holes. We have doubled this value for the next set of calculations. As expected, the intensity ratio is sensitive to N_e, with a less exaggerated profile with increasing N_e as the collisional component becomes more dominant.

2.7 Conclusions

Doppler dimming and pumping are conceptually simple processes. However, the equations of collisional and radiative coronal UV emission contain many parameters which add considerable com-

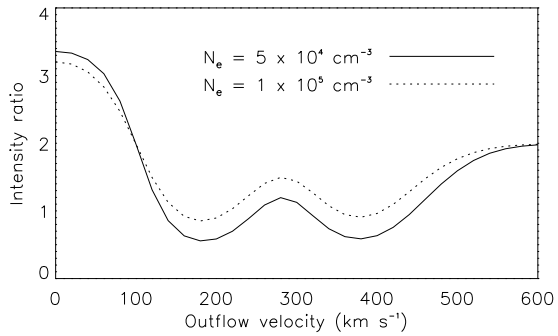

Figure 2.12: Intensity ratio as a function of outflow velocity calculated for 2 different N_e. The calculations were conducted for the same set of parameters as described in the previous section for figure 2.7 at a height of $3R_\odot$ with a temperature anisotropy of $T_\parallel = 0.01T_\perp$.

plexity to the modelling of coronal emission lines. In this chapter, the analytical forms of the equations are introduced. These form the core of an extremely efficient IDL line emission code which will play a central role in the empirical modelling of UVCS observations (chapter 4) and in a parameter study of O VI linewidth (chapter 5). In this chapter, a more basic modelling of lines from typical coronal hole conditions showed the power of the O VI intensity ratio as a diagnostic tool for outflow velocity. The modelling showed evidence of a $T_\parallel < T_\perp$ anisotropy, in agreement with previous observations of coronal holes by UVCS.

An important result of investigating the sensitivity of intensity ratio to various parameters is the impact of introducing a contribution from sunspots in the incident disk spectrum. The O VI intensity ratio at velocities below ~180 km s^{-1} is strongly affected by the sunspot contribution. This subject will be discussed further in chapter 4.

Chapter 3

Instrumentation, Observations and Data Analysis

3.1 Introduction

The UVCS instrument was introduced briefly in chapter 1. Section 3.2 of this chapter describes the UVCS instrument in more detail. Section 3.3 explains how UVCS makes measurements of the corona and describes the type of observation possible. Basic data processing is introduced in section 3.4, with spectral analysis and reduction techniques described in section 3.5. A discussion on the interpretation of the width of O VI coronal lines as a measure of temperature is given in section 3.6. Methods for creating contour maps of UVCS observables across large regions of the corona are given in section 3.7. Finally, an inversion method for obtaining electron density from polarized brightness measurements made by the Mauna Loa Mk IV coronameter and the LASCO C2 coronagraph, both introduced in chapter 1, is given in section 3.8.

3.2 The Instrument

A brief description of the UVCS instrument is given here. A full description can be found in Kohl et al. (1995). UVCS is aboard the SOHO spacecraft, which orbits the L1 Lagrangian point between Earth and the Sun. Figure 3.1 shows the layout and major parts of the UVCS instrument. Light enters through the entrance aperture onto the telescope mirrors, which focus images of the corona onto the entrance slits of the spectrometer assembly. Direct light from the Sun's disk is suppressed

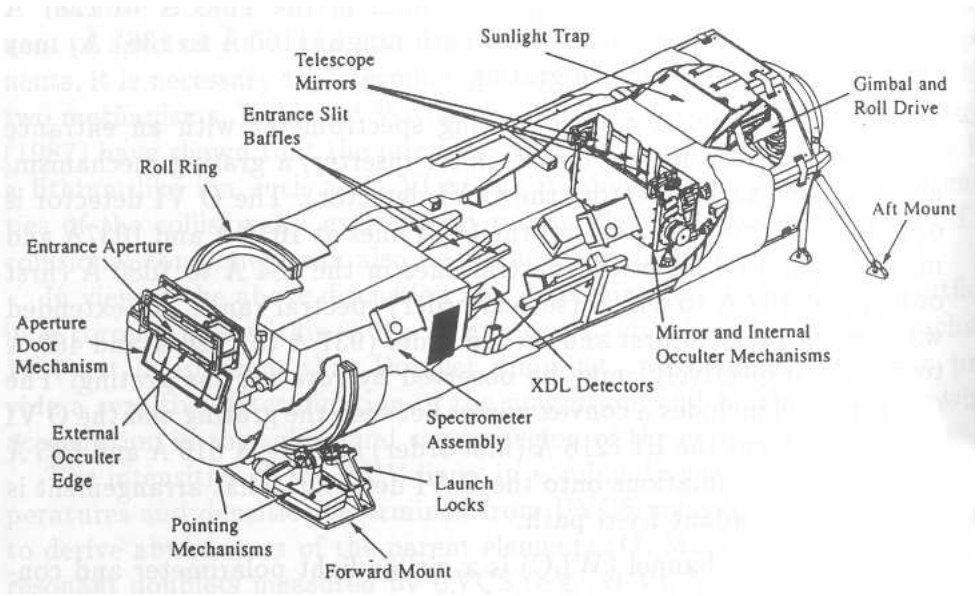

Figure 3.1: Diagram of the UVCS instrument with all major parts labeled (Kohl et al., 1995)

by the external and internal occulters. Internal reflection of unwanted light within the instrument is reduced by the sunlight traps. Light diffracted by the entrance aperture edges is prevented from reflecting off the telescope mirrors by an internal occulter mechanism placed in front of each mirror. Baffles on the entrance slits of the spectrometer further reduce unwanted light thus achieving the stray light suppression necessary for observations of UV spectral lines in the extended corona.

Two toric gratings and a visible light polarimeter form the three channels of the spectrometer - the Ly-α, O VI and the white light channel. The O VI channel is optimised for measurements of the two O VI lines at 1031.9 and 1037.6 Å. The light is dispersed by the grating onto a two dimensional photon counting detector. The detector is digitized to 1024 (spectral) $\times$ 360 (spatial) pixels. To improve the signal to noise ratio (SNR) or due to telemetry limitations, most observations combine these pixels into larger bins. For example, binning 6 spatial pixels together produces 60 spatial bins across the whole detector. A convex mirror between the grating and the O VI detector enables the simultaneous measurement of the H Ly-α line at 1216Å. This is called the redundant Ly-α path.

3.3 Observations

The field of view (FOV) of UVCS is defined as the portion of the corona's image that enters through the entrance slits into the spectrometer. Figure 3.2 (left panel) shows the FOV of the UVCS O VI channel. The FOV has a length of 40′, therefore we can see a $\sim 2.5R_{\odot}$ slice of the corona. The FOV

is always perpendicular to the solar radial direction at pixel number 200 (out of 360). The height of the FOV in the corona can be moved between 1.2 and 10 $R_\odot$ by moving the telescope mirrors. The position angle or latitude* can be changed to any angle by rolling the telescope assembly around its lengthwise axis. Light detectors within the sunlight traps of UVCS along with the stepper motors of the roll and mirror mechanisms determine the position of the FOV relative to Sun center.

A typical UVCS observational sequence is to observe at the same position angle over many heights consecutively. This is shown in figure 3.2 (right panel). Since the FOV is perpendicular to solar radial we can see how conditions change across different coronal structures. Viewing many heights consecutively allows the study of how conditions change with height within a certain structure.

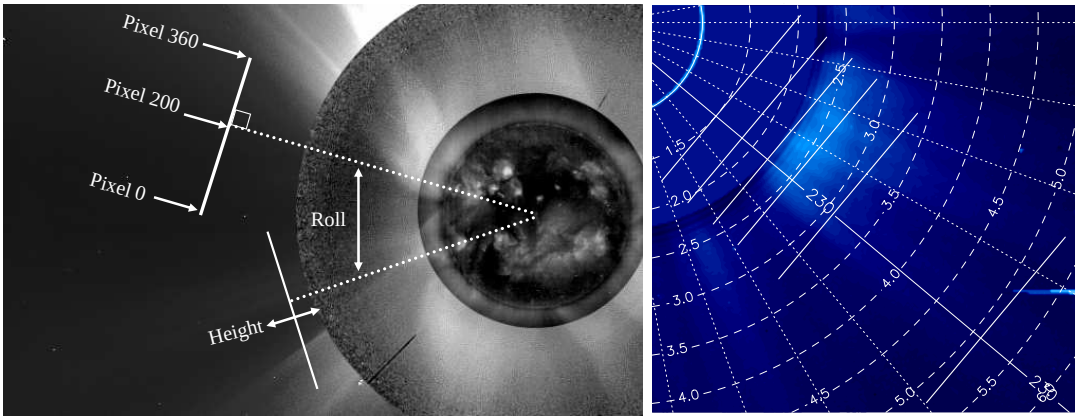

Figure 3.2: *Left* - the UVCS field of view (FOV) drawn on a nested image of the corona in white light. The FOV is the solid white line. The dotted line shows the radial line from Sun center to the FOV. Two possible positions of the FOV are shown. *Right* - a typical UVCS observing sequence.

Accumulated detector photon counts are collected in an exposure. Exposure time can vary but is often around 2 minutes or longer. Several exposures are collected in an observation and can be integrated during data analysis to improve the SNR. Figure 3.3 shows a detector image, obtained from a total integrated exposure time of 1.5 hours from an observation with a FOV of height 2.5$R_\odot$. Observations made of regions further out in the corona or in lower density coronal structures require longer integrated exposure times in order to get a decent SNR. It is possible also to adjust the width of the entrance slit, allowing a higher rate of photons in low intensity observations, or a lower rate if observing near the Sun.

*Position angle is measured in degrees counter-clockwise from solar North. Latitude is measured in degrees counter-clockwise from solar east. A measurement in position angle is the same as latitude minus 90°.

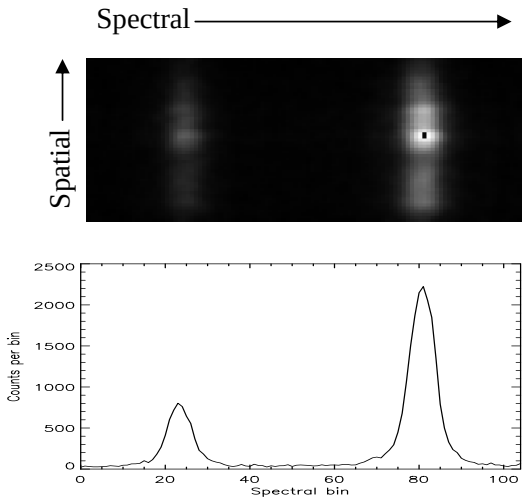

Figure 3.3: *Top* - UVCS O VI detector image from a total exposure time of 1.5 hours observed at a height of $2.5R_{\odot}$. Lighter shades mean more counts and the two O VI lines are clear in the image. *Bottom* - a spectrum obtained by summing over the 10 central spatial bins in the detector image.

3.4 Basic Data Processing

UVCS observations are available for analysis as spectral data files. The files are in FITS format and contain essential information on the observation as well as the uncalibrated detector data. In this section we summarize the steps necessary to convert the UVCS spectral files into meaningful data appropriate for analysis.

All calibration and other procedures discussed in this chapter may be conducted by using the standard UVCS Data Analysis Software (DAS) package, written for the Interactive Data Language (IDL). The flat field and calibration files are all included in the same analysis package available from the SOHO online archive or from *http://cfa-www.harvard.edu/uvcs/*.

3.4.1 Calibration and Flat Field Correction

Prior to analysis, there are three main steps of calibration which need to be made on the UVCS files: pointing, wavelength and radiometric calibration. The pointing calibration converts information such as the measured mechanical position of stepper motors or UVCS position relative to the SOHO spacecraft into meaningful measurements of FOV height and position angle. Wavelength calibration translates spectral detector bins into physical units of wavelength (Å). Radiometric calibration translates detector counts into physical units of intensity (photons s^{-1} cm^{-2} Ω^{-1} $Å^{-1}$). The accuracy of UVCS radiometric calibration has been tested in laboratories pre-flight and with

comparisons of observations of the UV emission of stable stars with observations made by other telescopes in flight (Gardner et al., 2002). The uncertainty of radiometric calibration of first order lines is between 20 to 22% depending on the observed height and the year of the observation (the detectors degrade slowly with age). In this work, the uncertainties of absolute intensities includes the 22% calibration uncertainty. This does not affect measurements of linewidths or line intensity ratios.

Different regions of the O VI detector have different gain responses and this bias is removed by dividing the detector counts with a flat field calculated from averaged synoptic data and observations of stars. Further discussion of UVCS efficiency arising from variations in the toric gratings is given by Gardner et al. (2000).

3.4.2 Combining Data

By combining exposures and spatial bins, the photon count per bin, n, is increased and the Poisson uncertainty in the number of counts, $\sqrt{n}$, becomes small compared to n. It is necessary to combine many exposures to obtain a decent SNR. This is easily done although there are occasionally contaminated exposures which need to be removed. The contamination involves spikes in the data, or single detector pixels with extremely high counts. Often a contaminated exposure will contain many of these spikes. They can be caused by energetic particles entering through the UVCS shielding and hitting the detector. The automated exposure combining software of DAS identifies spikes by finding detector bins which have a count greater than around 6.6×10^4. It is also possible to view the exposures by eye and identify the bad exposures which have a flurry of white pixels. These are removed prior to combining. Observations that are seriously deteriorated due to a high proportion of bad exposures are rare.

To further improve the SNR it is often necessary to combine spatial bins. Spatial resolution is sacrificed in order to reduce uncertainties although at low heights in streamer or quiet Sun regions this may not be necessary. At high heights in coronal holes all spatial bins across the slit may need to be combined. In figure 3.3, 10 spatial pixels are combined in order to obtain the high photon counts shown in the lower panel. The weaker O VI 1037 line has a peak count of $\sim$ 800, giving a good relative uncertainty $\sqrt{n}/n$ of 3.5% for that spectral bin. The spatial edges of the detector image are unreliable therefore a few spatial bins at the extremities of the slit are always discarded.

3.4.3 Correcting the Spectrum

The spectrum measured by UVCS is a convolution of the original coronal spectrum with various instrumental effects which serve to redistribute the original intensity and widen spectral features (Kohl et al., 1997). Many of these instrumental effects are well modeled through pre-launch laboratory tests, observations of the weak and narrow interplanetary Hydrogen Ly-α line and comparisons between UVCS and results from other instruments. The known instrumental broadening functions are illustrated in figure 3.4, along with their effect on a Gaussian function. Gardner et al. (2000) found variations in replicas of the UVCS toric grating in a direction perpendicular to the grating grooves. These variations could significantly affect the interpretation of observations although at present the effect cannot be removed from the data without further investigation.

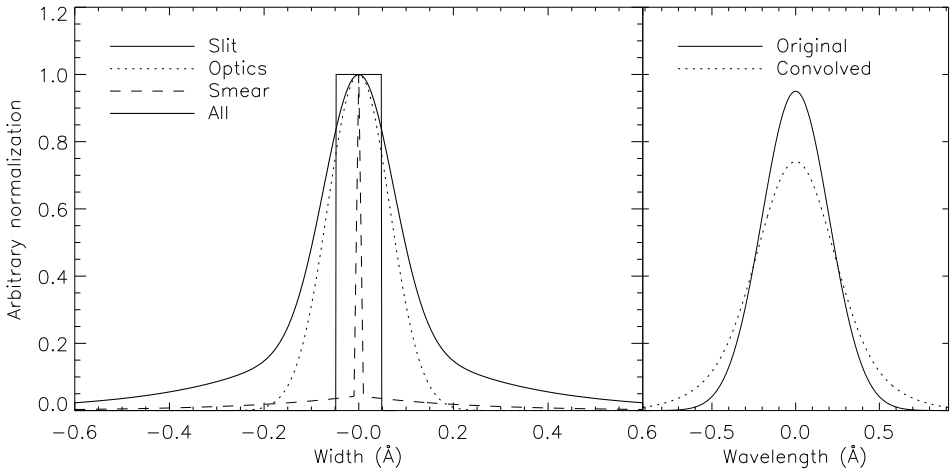

Figure 3.4: *Left* - Model profiles of known UVCS instrumental broadening functions (all normalized to unity). The labels in the legend refer to the following. 'Slit' refers to the slit profile, a rectangular function with width equal to the slitwidth. 'Optics' is a Gaussian function which includes the point spread function of the spectrometer and digitization of the incident dispersed spectrum on the detector. 'Smear' is an instrument characteristic that smears spectral features so that broad wings extend to their sides, with an amplitude of 1-3% of the peak feature intensity (Kohl et al., 1997). For illustration purposes only, we have exaggerated the amplitude of the wings. 'All' is a convolution of all the above-mentioned effects. *Right* - The effect of the model instrumental broadening on a Gaussian function. As with all convolutions, the intensity is redistributed but the total intensity is conserved.

Smear

This effect is an unexpected UVCS characteristic that smears spectral features so that broad wings extend to their sides, with an amplitude of 1-3% of the peak feature intensity (Kohl et al., 1997).

Observations of the narrow interplanetary H Ly-α helped model this feature. The correcting function was validated by comparing UVCS chromospheric Ly-α observations with observations from other instruments. The UVCS DAS corrects for this effect using an iterative convolution with a zero integral function. Although generally reliable, noisy input occasionally results in corrections with negative intensities. Gold's method of deconvolution (Gold, 1964) is an iterative deconvolution algorithm which does not allow such non-physical results. Tested on clean UVCS data, it gives results virtually identical to that of the zero-integral function. On noisier data, negative intensities are avoided although the corrected profiles are smoothed. The smoothing is a necessary symptom of the iterative method which helps avoid amplification of noise. The use of a smoothing window of width 3 spectral bins smooths the high frequency noise while spectral features wider than 3 bins are preserved. Lines in the UVCS spectrum are much wider than 3 spectral bins so the deconvolution process can not affect the final results significantly. Jansson (1997) gives a comprehensive introduction to deconvolution of spectra.

Optical Broadening

This effect includes the broadening due to the point spread function of the spectrometer and digitization of the incident dispersed spectrum on the detector. It may be removed by deconvolution but in practice, since it is well approximated by a Gaussian, the UVCS spectrum may be left uncorrected. After fitting the spectral line with Gaussian functions, the optical broadening may be subtracted in quadrature from the fitted linewidths: $\Delta\lambda^2_{corr} = \Delta\lambda^2_{fit} - \Delta\lambda^2_{optical}$.

Slit Broadening

The UVCS entrance slit is of course not a one-dimensional line, and the narrow spatial width of the slit lies in the same direction as the spectral dimension of the detector therefore there is an intrinsic broadening of the spectrum which depends on the variable width of the entrance slit. This broadening function is shown as a rectangular function in figure 3.4 with a width equal to the entrance slit. In reality, one side of the entrance slit FOV is closer to the Sun than the other and has a higher intensity. In the case of an observation which has a steep intensity gradient, that is, observations made close to the Sun, the slit profile needs to be modeled as a trapezoid, with the gradient of the trapezoid's roof reflective of the intensity gradient across the UVCS slit. DAS compensates for this

broadening as part of the Gaussian fitting routine (to be described below). The fitting algorithms fit the spectral lines with Gaussians pre-convolved with the appropriate trapezoid slit function rather than pure Gaussians. To obtain information on the intensity gradient, observations at 2 close heights are needed.

3.4.4 Stray Light

Despite the advanced design of UVCS, some stray light from the Sun's disk reaches the spectrometer and contaminates the coronal data. The level of contamination can be determined in-flight from a knowledge of both the disk intensity of a low-charge state ion and the intensity of that line observed by UVCS in the corona. The presence of a line from such an ion in UVCS coronal observations must be completely due to stray light since these ions are formed at low temperatures and do not survive in the hot corona. This is shown in the top right plot of figure 3.5. This plot shows the fraction of carbon and silicon that is twice ionized as a function of the electron temperature. Both ions are extinct at temperatures of $\sim 3 \times 10^5$ K. These values are tabulated in the CHIANTI atomic database from calculations by Mazzotta et al. (1998). The ratio of the UVCS measured line intensity over the measured disk intensity gives a stray light fraction at the observed height.

Figure 3.5 (left) shows some measurements of stray light fraction against height. As described in Gardner et al. (2002), the pre-flight laboratory measurements were made with only one optical configuration equivalent to observing the corona at a height of $2.7R_\odot$. The stray light fraction estimate obtained from the laboratory test is the square plotting symbol in figure 3.5. The other measurements were obtained from Si III and C III intensities.

A good fit to the measured stray light fraction is given by

$$\frac{6.4 \times 10^{-8}}{(r-1)^{3.4}} > 2 \times 10^{-9}$$

where r is the height in $R_\odot$. This is the value used by the UVCS DAS. The stray light fraction is then multiplied by the disk intensity of a line to acquire the stray light intensity. The inset in the left plot of figure 3.5 shows the estimated stray light of O VI 1032 and 1037 as a function of height. The bottom right plot compares 84 observed O VI 1032 intensities with the estimated stray light. The intensities were gathered from 28 observations of different coronal structures at various heights, position angles and dates. It is clear from this plot that the stray light can be neglected at heights

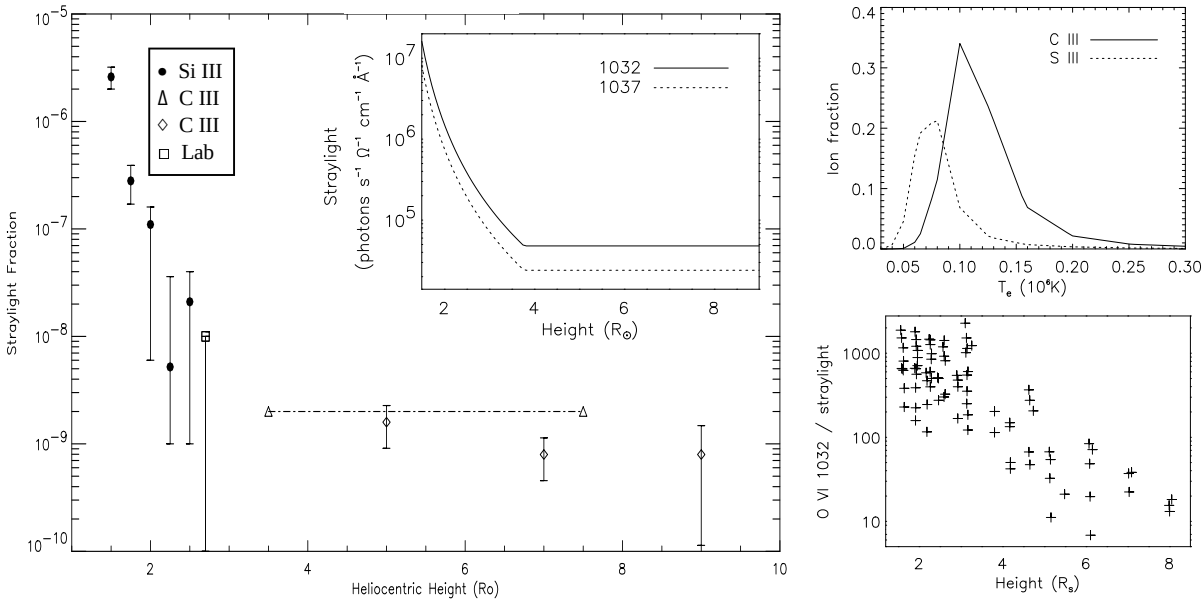

Figure 3.5: *Left* - Calculations of the stray light fraction at various heights. Values of the stray light fraction measured inflight are shown as filled circles (Si III), triangles (CIII by R. Suleiman) and diamonds (C III by J. Raymond). The square is a laboratory measurement. The inset plot shows O VI 1032 and 1037 straylight obtained by a line fitted to the straylight fraction measurements multiplied by the O VI disk intensities (see text). *Top right* - the fraction of carbon and silicon that is twice ionized as a function of electron temperature, as tabulated in the CHIANTI database from calculations by Mazzotta et al. (1998). *Bottom right* - 84 O VI 1032 intensities gathered from 28 UVCS observations of various structures at various heights, position angles and dates, divided by the O VI 1032 stray light estimate.

below 5 $R_\odot$. Observations of low intensity structures at heights above this can have a 10% or more contribution from stray light. In this work we neglect stray light in O VI observations at heights below 4 $R_\odot$. Above 4 $R_\odot$, we remove the stray light estimate from intensities and add an uncertainty equal to the stray light estimate to the intensity uncertainty.

The bulk of the stray light comes from the portion of the Sun's disk directly below the position of the UVCS observation in the corona (L. Gardner, private communication). Chromospheric O VI lines are stronger by a factor of 60 or more in sunspots (see section 2.6.1 in chapter 2) therefore any observations made directly above sunspots will contain a much greater intensity of stray light.

3.5 Spectral Analysis

The analysis of UVCS O VI spectra involves the fitting of the O VI spectral lines to Gaussian functions and a constant background. The assumption of a constant background is valid since the

wavelength range of the O VI spectrum is narrow and the background is fit well by a constant. From the fitted Gaussian functions, useful values such as total intensity and linewidth are obtained. There are many good text books on data reduction and error analysis that give comprehensive descriptions of the techniques included in this section, for example Bevington & Robinson (1992) or Barford (1985).

3.5.1 χ^2 Goodness of Fit

It is important to realize that fitting the coronal lines with Gaussians implies the use of a basic model. The line profiles contain contributions from a line of sight (LOS) through the corona. Fitting a single Gaussian to such a profile implies either that the bulk contribution to the line comes from the plane of sky (POS) or that the plasma along the LOS is static and isothermal. In many observations, fitting a line to a single Gaussian is valid since the observed line is very close to a Gaussian shape. This can be tested by a reduced χ^2 goodness of fit. For data points y_i with uncertainties σ_i and modeled values y_x we have

$$\chi^2 = \frac{1}{N-M} \sum_{i=1}^{i=N} \frac{(y_i - y_x)^2}{\sigma_i^2} \tag{3.1}$$

where N is the number of data points and M the degrees of freedom. The degrees of freedom are the number of free parameters needed to describe the model, for example a single Gaussian function has three degrees of freedom since only 3 parameters describe a Gaussian (peak intensity, line center and linewidth). A good reduced χ^2 value is close to 1. Values much larger than 1 imply that the model is inappropriate for the data.

3.5.2 Minimizing χ^2

If the minimum of the χ^2 distribution in relation to the fitting parameters can be found, the best possible fit between model and data is found. A computationally efficient way of finding a minimum in a χ^2 distribution is to find a point where $d\chi^2/dz_j = 0$, where z_j is a Gaussian or background parameter. This is the Gauss-Newton method of least-squares fitting. $d\chi^2/dz_j$ is readily computed from equation 3.1 for each fitting parameter z_j. Equating each $d\chi^2/dz_j$ to zero gives a set of equations that can be solved to find a minimum in the χ^2 distribution. Uncertainties in a fitted Gaussian parameter z_j are given intuitively by the sum over all data points of the products of the data uncertainties and

the sensitivity of z_j to changes in the data values (all squared):

$$\sigma_{z_j}^2 = \sum_{i=1}^{i=N} \sigma_i^2 \left(\frac{dz_j}{dy_i} \right)^2 . \tag{3.2}$$

These uncertainties, once a best fit is found, are multiplied by the reduced χ (square root of equation 3.1). The UVCS DAS uses a Levenberg-Marquardt χ^2 minimization algorithm to fit Gaussian functions to spectral lines. The Levenberg-Marquardt method is a modification of the Gauss-Newton method, but is more robust and can be used on non-linear functions. Least-square fitting of this type is computationally efficient but can sometimes find a local minimum in the χ^2 distribution rather than the global minimum. Genetic algorithms are far less susceptible to getting trapped in a local minimum and are very successful in finding global minima given noisy data. As computers become faster, genetic algorithms are becoming more popular in fitting Gaussians to complex spectra containing many spectral lines which often overlap, such as a SUMER spectrum (McIntosh et al., 1998). It is redundant to use such a slow procedure on the more clear cut UVCS spectra, but it can be used here to test the accuracy of the DAS fitting software. Comparison between DAS and the genetic algorithm are given in table 3.1 for 3 UVCS O VI 1032 Å lines observed at different heights. Lines 1, 2 and 3 are observed at 1.5, 2.2 and 3.1 $R_\odot$ in different coronal regions, and become more noisy with height. Since the genetic algorithm contains random methodology, each fit has been repeated five times and the mean and standard deviation of each parameter is given here for each line. The DAS gives a considerably better fit for the cleanest spectrum of line 1. The genetic algorithm gives a better fit for the noisier line 3 although the Gaussian parameters are almost identical, with the major difference being in the background. It is safe to conclude, from this test and general use, that the DAS line-fitting software gives excellent results with a reasonably clean UVCS spectrum. Care must be taken with noisier spectra. In general, if the data is so noisy that DAS does not give reliable results, we should not consider using those data for analysis.

3.5.3 Fitting Lines with Multiple Gaussians

Fitting any spectral line with two Gaussians rather than one will almost always result in a better fit due to the doubling of the degrees of freedom. However, modeling spectral lines with multiple Gaussians is only meaningful if all fitted Gaussians have a significant intensity, and an appropriate

Table 3.1: Comparison of Gaussian parameters fitted to 3 O VI 1032 spectral lines using UVCS DAS and a genetic algorithm. I is the total intensity in 10^8 photons s^{-1} cm^{-2} sr^{-1} $Å^{-1}$ and the $1/e$ halfwidths and line centers λ_0 are in Å. I_{bg} is the background intensity in 10^6 photons s^{-1} cm^{-2} sr^{-1} $Å^{-1}$. The values and ranges given in the genetic algorithm fitting parameters are means and percentage standard deviations for 5 runs. If no range is given, it is less than 1%. Spectra 1, 2 and 3 are described in the text.

	UVCS DAS					Genetic Algorithm				
	χ^2	I	λ_0	$\Delta\lambda$	I_{bg}	χ^2	I	λ_0	$\Delta\lambda$	I_{bg}
1	11.9	223	1031.86	0.31	665	16.4 ± 4	213	1031.86	0.31	577 ± 4
2	19.4	11.7	1031.84	0.32	81.7	20.7	11.4	1031.84	0.31	69.3 ± 2
3	6.4	1.25	1031.94	0.58	6.96	4.6	1.25	1031.94	0.57	6.20

interpretation of the multiple Gaussian profile can be given. If an observed line has an obvious 2 Gaussian profile and we cannot allocate physical reasons for this, the two sets of Gaussian parameters are useless values. In practice, UVCS O VI observations often have a 2 Gaussian profile, and from viewing such profiles it is obvious that fitting with only one Gaussian is not satisfactory. Unfortunately the reasons behind such profiles are not always apparent.

As an example, consider the work of Miralles et al. (2001), a study of a large high-latitude coronal hole. A 2 Gaussian fit was made to the O VI lines in order to distinguish between contributions along the LOS from the coronal hole and contributions from the surrounding medium. In this case, the use of 2 Gaussians is obvious and useful. UVCS data from the same coronal hole analysed by Miralles et al. (2001) from 2001 February 12 observed at a slit height of $2.0R_\odot$ and slit position angle $6°$* are shown in the left panel of figure 3.6. The wide O VI 1032 Å profile has a large linewidth of 0.96Å indicative of the high O VI temperatures in the coronal hole and the narrow component has a linewidth of 0.19Å. In the right panel are UVCS data from a coronal region which does not contain a large coronal hole along the LOS. This was determined from EIT images in various lines, LASCO and Mauna Loa MK IV white light images and HeII 10830Å low resolution coronal hole maps produced by the Kitt Peak NSO Vacuum Telescope. Despite this apparent absence of a coronal hole, a 2 Gaussian profile fits each line comfortably. In this case, the wide O VI 1032 Å profile has a linewidth of 0.71Å and the narrow component a width of 0.15Å. The simple geometrical LOS argument for fitting 2 Gaussians in the presence of coronal holes given by Miralles et al. (2001) is not valid here. Even if a small coronal hole was situated along the LOS, it would be highly unlikely

*Slit height and slit position angle refers to the average height and position angle of the portion of the slit analysed.

to give such a strong contribution to the profile. In general analysis, the work in this thesis avoids such profiles. It would be inaccurate, for example, to fit an obvious 2 Gaussian profile with a single Gaussian and claim the linewidth as a measure of ion temperature.

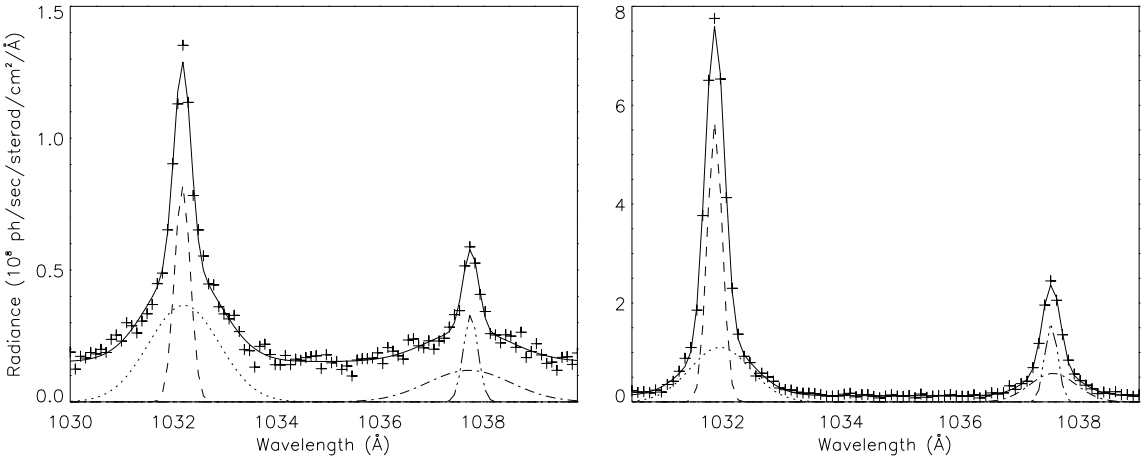

Figure 3.6: *Left* - O VI data (crosses) from 2001 February 12 observed at a slit height of $2.0R_\odot$ and slit position angle 6° above a large coronal hole. All UVCS slit pixels were combined to achieve this clean spectrum. The fit to two Gaussians per line and a background is shown as the solid line. The dotted and dashed lines show the four Gaussians. *Right* - O VI data (crosses) from 2000 May 6 observed at a slit height of $2.7R_\odot$ and slit position angle 136°. 14 slit bins are combined here, and each slit bin contains 6 pixels.

The UVCS DAS line-fitting software allows the user to place constraints on one or more of the fitting parameters, and this is most often used when fitting 2 Gaussians to each O VI line. For example, Miralles et al. (2001) use geometrical arguments to place a constraint on the fitting of 2 Gaussians to each line so that the separation between the wide components of the 1032 and 1037 lines ($\sim$ 5.6Å) should be the same as the separation of the narrow components. A more common usage of parameter constraint is to couple the widths of the wide and narrow components of each line. This is the default setting for the software when fitting 2 Gaussians to each line. This constraint is based on the belief that the wide part of the line is caused exclusively by the collisional component and the narrow by the radiative component. No constraints of this kind are placed on the fitting in this thesis.

3.5.4 Uncertainties

The final uncertainties in the Gaussian parameters given in this work are propagated from the initial Poisson counting statistics, fitting uncertainties and χ^2 goodness of fit. The value of absolute total

line intensity has then the additional uncertainties of the background intensity, stray light and the prominent 22% uncertainty of the radiometric calibration. The derived 1032/1037 intensity ratio does not include the calibration uncertainty.

3.6 Interpreting UVCS Linewidths

It is convenient to express line profiles as a velocity distribution rather than a spectral length:

$$V = \frac{c\lambda}{\lambda_0} \tag{3.3}$$

where λ_0 is the theoretical line center, λ is the wavelength and c is the speed of light. From this profile and the fit to Gaussians, $V_{1/e}$ gives the most probable speed of ions along the LOS. Kohl et al. (1997) state that equation 3.3 is precise to ±10% for a spherically symmetric distribution of ions along the LOS, or for ions situated in the POS.

Models of coronal plasmas generally use temperatures rather than spectral widths or $V_{1/e}$. Observed $V_{1/e}$ contains not only information on ion temperatures (thermal motions) but also a dependence on velocities of the bulk of the plasma such as outflow velocity or microturbuluence (non-thermal motions). Therefore an effective temperature can be obtained directly from UVCS spectral lines by

$$2kT_{eff} = \frac{mV_{1/e}^2}{8} \tag{3.4}$$

where k is Boltzman's constant and m the ion mass (Withbroe et al., 1982). An estimate of the velocity component due to non-thermal motions, ξ, allows an estimate of the true temperature:

$$2kT = m\left(\frac{V_{1/e}^2}{8} - \xi^2\right) \tag{3.5}$$

Outflow velocity can change the width of UVCS lines not only by the component of outflow velocity along the LOS but also by changing the relative contributions of radiative and collisional components. The collisional and radiative components have different widths due primarily to their different density dependence - the collisional component is proportional to $n_i n_e$ whereas the radiative component is proportional to n_i only, both integrated along the LOS. Withbroe et al. (1982) found an increased width of 12.8% in the H Ly-α line with a radial outflow of 400 km s^{-1} at a height

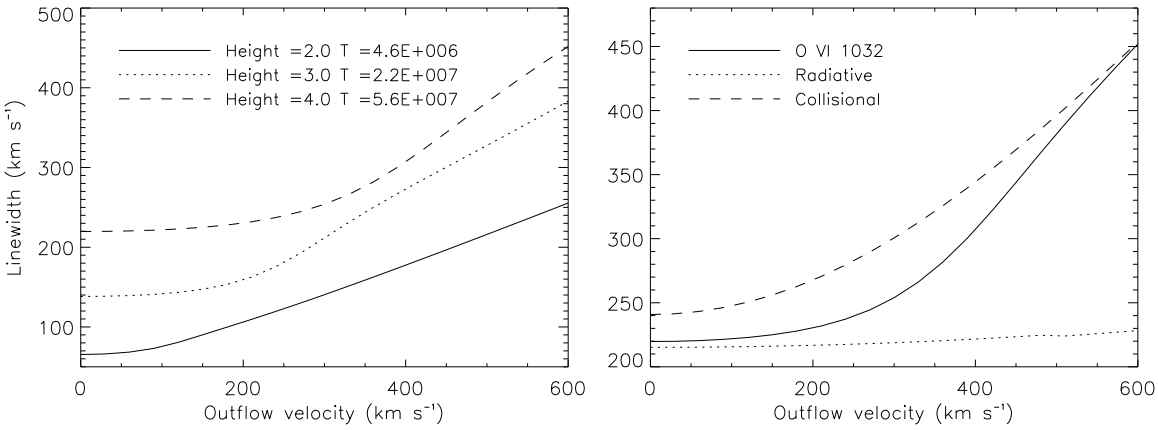

Figure 3.7: *Left* - Sensitivity of O VI 1032 linewidth to outflow speed at 3 heights. In the legend, heights are in $R_\odot$ and temperatures in K. *Right* - A more detailed plot of linewidth as a function of outflow speed at height 4 $R_\odot$, with the linewidths of the collisional and radiative components plotted separately.

of $4R_\odot$ and a temperature of 1.5×10^6 K. The left panel of figure 3.7 shows modelled O VI 1032 linewidths as a function of outflow speed for three heights. The model uses a simple isothermal and isotropic temperature distribution and constant radial outflow velocity along each LOS. (See section 1.5 of chapter 2 for more details of the modelling such as electron density and temperature). The ion temperatures used here are those used in chapter 2 multiplied by 0.7. The temperatures used in chapter 2 are effective temperatures derived from a coronal hole observation, and the factor of 0.7 used here is a crude estimate of the true temperature, sufficient to show the general behaviour of linewidth as a function of outflow speed.

It is clear that the O VI linewidth is far more sensitive to outflow speed than the results Withbroe et al. (1982) found for the Ly-α line. At a height of $4R_\odot$ and an outflow of 400 km s^{-1}, the model shows a 40% increase in the O VI 1032 linewidth compared to no outflow. The right panel of figure 3.7 shows in greater detail the linewidth as a function of outflow speed at height $4R_\odot$. Also shown are the widths of the collisional and radiative contributions to the line. Less than 10% variation is seen in the width of the radiative component. The sensitivity of the line to outflow velocity is almost entirely due to the collisional component. The Ly-α line is formed almost completely by radiative excitation which results in a much lower sensitivity to the outflow speed.

The removal of line broadening due to outflow velocity from the observed effective temperature is possible using an iterative procedure. This procedure iteratively improves on an initial estimate of outflow velocity using an observed O VI intensity ratio while simultaneously improving on an

estimate of the actual ion temperature using the observed linewidth. Such a procedure is described in chapter 4. The procedure does not remove any broadening due to other non-thermal motions such as waves or turbulence.

3.7 Sliding Windows and Contour Maps

Section 3.4.2 states the necessity of combining spatial UVCS detector bins to obtain a statistically acceptable photon count. Analysis of large coronal hole observations at heights above $\sim 2.5R_{\odot}$ usually involves the integration of a large number of spatial bins. Generally, there is no need to combine so many bins, and this allows the possibility of using a type of sliding window average during analysis to integrate bins across the slit.

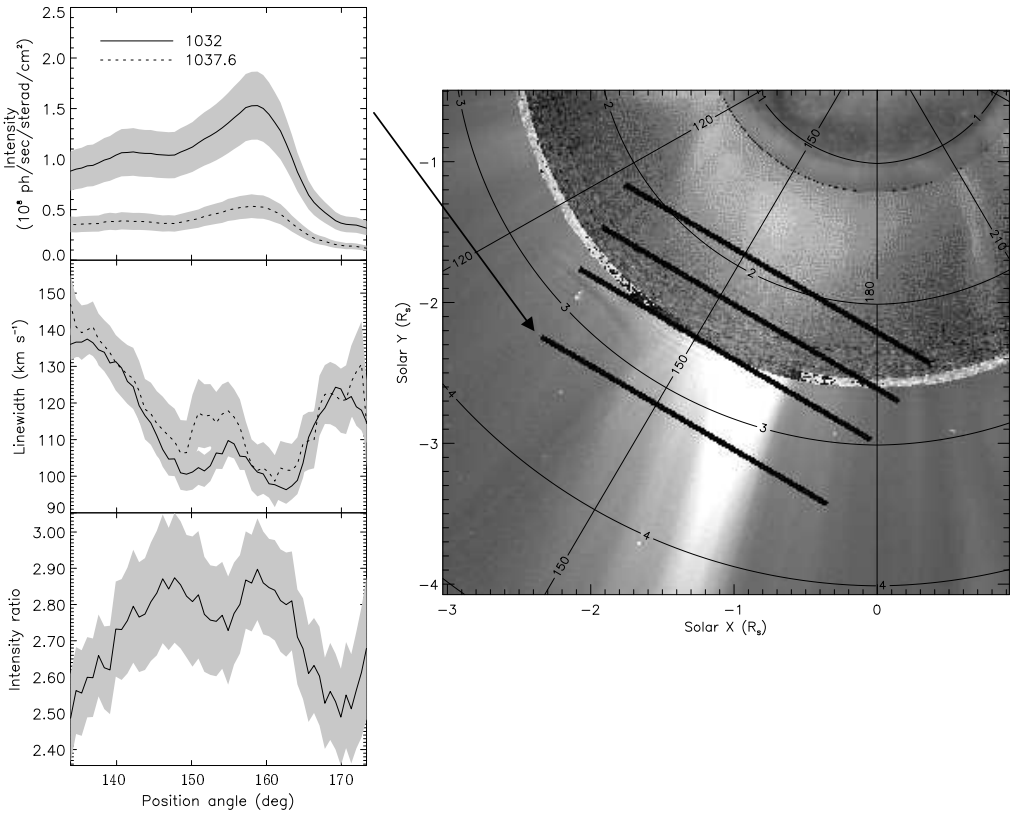

Figure 3.8: *Left* - O VI 1032 and 1037 intensity (top), linewidth (middle) and the 1032/1037 intensity ratio (bottom) obtained using a sliding window to combine spatial bins. Shaded areas show the one sigma uncertainties. The intensity uncertainty includes the 22% radiometric calibration uncertainty. *Right* - Positions of 4 consecutive UVCS observations made during 2000/05/06 (thick black lines) overlaid on an EIT 284 Å image of the lower corona and Mauna Loa MK IV and LASCO C2 white light images of the extended corona. The observation at the largest height of 3.1 $R_{\odot}$ (indicated by the arrow) is the one used for the results on the left.

The left panel of figure 3.8 shows an example of the results when using a sliding window prior to spectral analysis. The position of the observation, as shown in the right panel, is at slit height $3.1R_{\odot}$ and position angle 150°. The ~ 4 hour observation started at 22:16 on 2000/05/06 and collected exposures over 3.5 hours. The observational spectral binning is 6 pixels, giving 60 bins across the whole FOV prior to discarding the unreliable pixels at the slit extremes. A sliding window of 9 bins is used here - each bin takes the spectral parameters obtained from integrating the photon counts from the surrounding ±4 bins. The edges of the slit are truncated, that is, the first slit bin is combined with the next 4 bins, and the second bin is combined with the previous 1 bin and the next 4 bins, and so on. A wider window is sometimes used at the slit edges due to the deterioration of statistics.

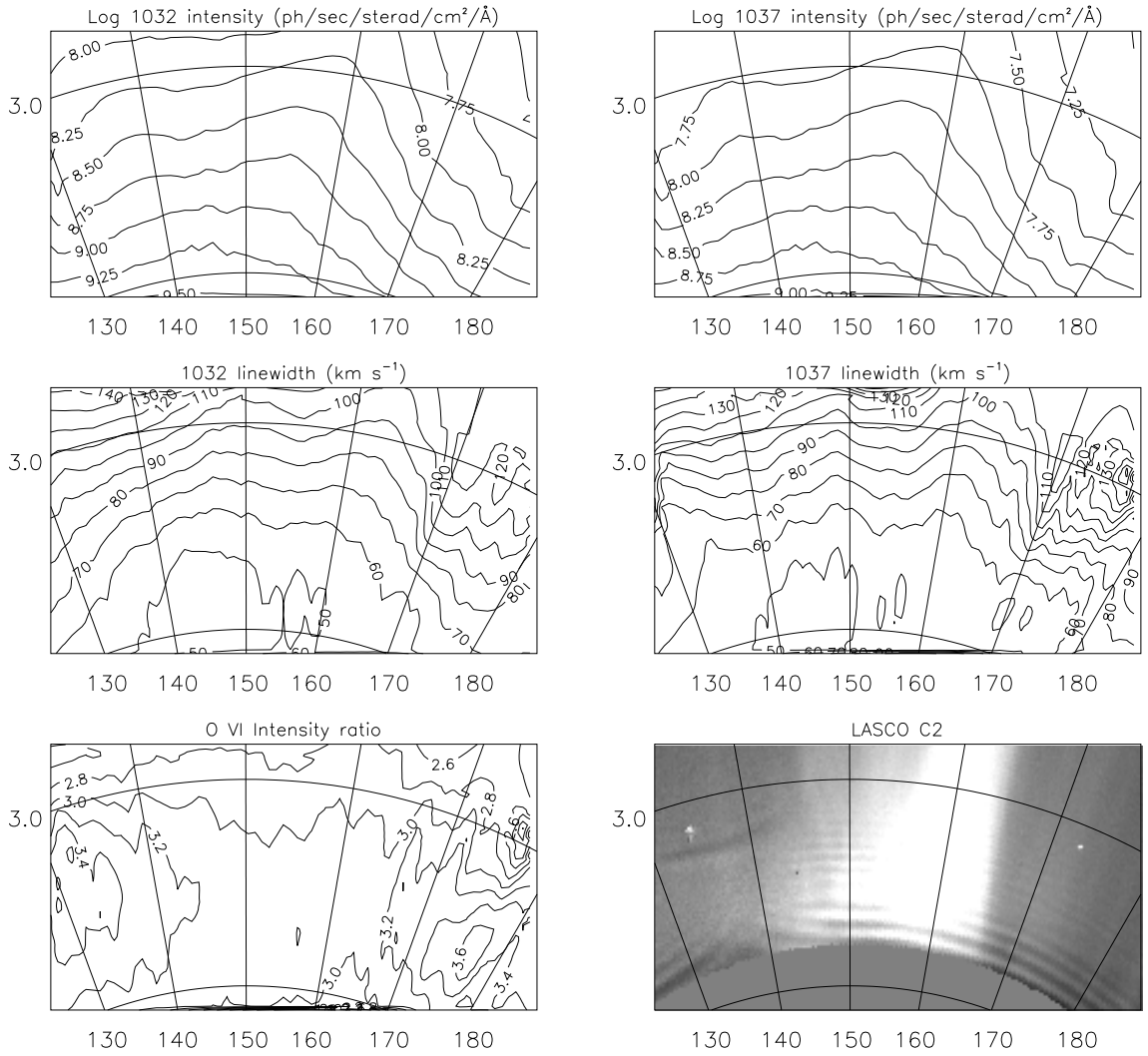

Figure 3.9: Contour maps created from the sequence of observations shown in the right panel of figure 3.8. The bottom right plot shows the relevant region of the corona extracted from a LASCO C2 white light image. The x-axis labels position angles in degrees and the y-axis labels heights in $R_{\odot}$.

When using this technique on observations which have a wide range of different intensities, for example, observations encompassing a streamer and a coronal hole, the width of the sliding window may be adjusted across the slit according to the changing photon count. The sliding window provides good statistics and a measurement for each slit bin, but also smears features across the slit. For example, streamers will appear wider than they should.

Applying the sliding window analysis to a series of consecutive observations made at different heights but at a similar position angle enables the creation of contour maps of spectral observables across large areas of the corona. Consider for example the observation sequence shown in figure 3.8. The observations were made consecutively over the course of 16 hours at closely separated heights. Movies of the corona compiled from the white light images of LASCO C2 show that the region observed was stable over this period, i.e. there were no large scale changes in structure or explosive events to disturb the region. Sliding windows are applied at each height, with a window width of 5 bins at the lowest height, increasing to 9 at the highest height to obtain values such as intensity and linewidth across the slit. The IDL TRIANGULATE procedure (Delaunay triangulation) is used to interpolate for values in the regions between the observations. The interpolation is made in latitude and height space rather than the simpler solar x and y space since a radial expansion is typical of most coronal structures.

Results for the 2000/05/06 observation sequence are shown in figure 3.9. The streamer centered at position angle 160° is the dominant structure in this region. The high density and low ion temperature of the streamer results in the higher intensity and narrower linewidth around position angle 160° in the UVCS maps. Maps such as these will be used in chapter 4 as a base for modeling coronal conditions across large regions of the corona.

3.8 Electron Density from LASCO C2 Observations

Polarized brightness (pB) maps of the whole corona in the height range $\sim 2 - 6R_{\odot}$ made by the LASCO C2 coronameter are available online from *http://lasco-www.nrl.navy.mil/retrieve/polarize/*. Polarized brightness in the height range $\sim 1.4 - 2.4R_{\odot}$ is observed by the Mauna Loa MK IV coronameter and these data are available from *http://mlso.hao.ucar.edu/*. The pB data from both instruments have been calibrated at their time of processing and are suitable for quantitive analysis. The left panel of figure 3.10 shows the corona in white light observed with both LASCO C2 and

Mauna Loa Mk IV on 2000/05/05. The two right panels shows electron density obtained from the Mauna Loa MK IV (bottom) and LASCO C2 (top) pB measurements. The inversion method used for deriving the electron density is detailed in Quémerais & Lamy (2002) and only a brief description is given here. Quémerais & Lamy (2002) applied the inversion to LASCO C2 data and found the method robust and in agreement with electron densities obtained by other instruments and analysis methods.

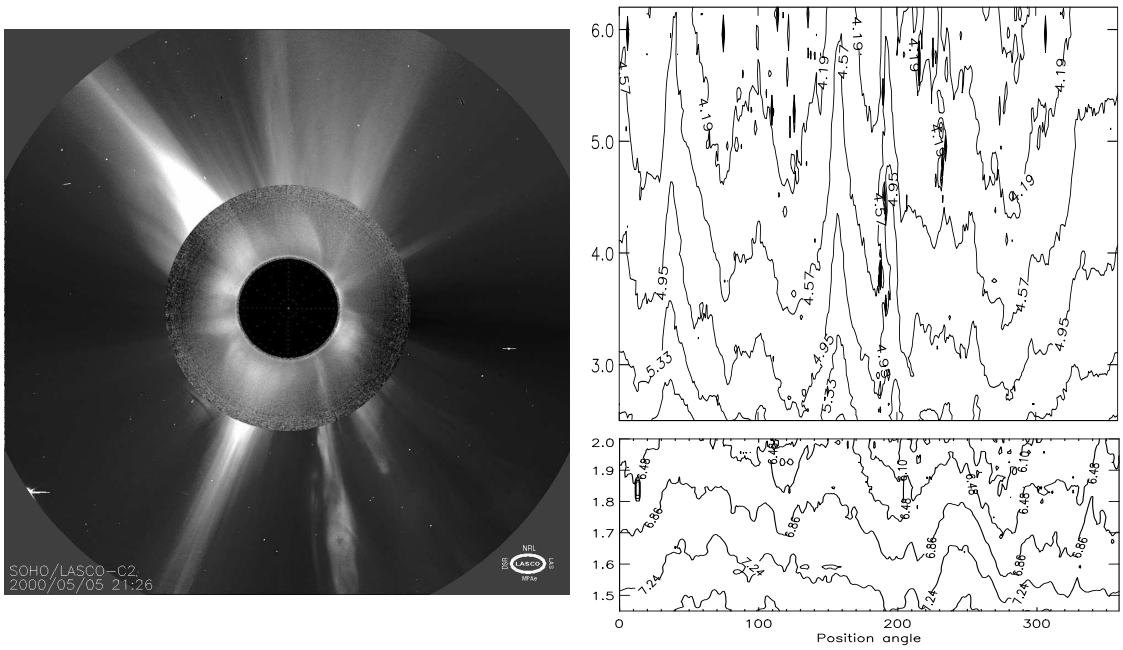

Figure 3.10: *Left* - the corona in white light observed on 2000/05/05. The nested images of the corona are from the LASCO C2 (outer) and Mauna Loa Mk IV (inner) coronagraphs. *Right* - electron density in the corona for date 2000/05/05 obtained from LASCO C2 (*top*) and Mauna Loa MK IV (*bottom*) pB data. The y-axis show heliocentric height in $R_\odot$ and the contours are in units of log cm^{-3}.

Electron densities are derived from an inversion of the pB data. The pB intensity emitted from the optically thin corona is proportional to the electron density integrated along a LOS. An initial estimate of the electron density profile along a LOS can give a synthesized value of pB at the point where the LOS intersects the coronal plane of sky. Synthesized pB is calculated for two neighboring points along a radial direction from the Sun. The density profiles are iteratively adjusted until the synthesized pB and the pB radial gradient matches the observed. The inversion therefore assumes a local spherical symmetry to the electron density. In the case of figure 3.10 the inversion is applied to the whole corona. In general, good agreement is found between the inversion of the Mauna Loa MK IV and LASCO C2 data. The reliable height range for Mauna Loa MK IV is usually around 1.4 to

$2.0R_\odot$. The lowest reliable height for LASCO C2 is $2.5R_\odot$. The highest reliable height range varies with position angle since LASCO has a square field of view centered on the Sun. At 0, 90, 180 and 270° the height is restricted to $6R_\odot$ while in the corners, at 45, 135, 225 and 315°, the field of view extends to $8R_\odot$. Occasionally the inversion fails and this is due usually to anomalies such as spikes or zero readings in the pB data. Otherwise the method is as robust as suggested by Quémerais & Lamy (2002).

3.9 Conclusion

In this chapter a brief description of the UVCS instrument and a detailed description of UVCS data correction and reduction procedures are given. There have been almost eight years of near-continuous observations of the corona made by UVCS, from the end of solar minimum in 1996/97 throughout the peak of the recent solar maximum. The IDL data analysis software supplied by the UVCS team, coupled with user written software and the graphical abilities of IDL enable accurate and swift analysis of observations. This chapter has also introduced a method for obtaining electron density estimates from LASCO C2 polarized brightness observations. Armed with these tools, the following chapter aims to couple the results of both UVCS and LASCO observations and the UV line emission model described in chapter 2. A successful coupling leads to constrained values of ion outflow velocities, densities and temperatures based on certain assumptions. Such a comprehensive analysis would of course be impossible without the high quality data presented by UVCS.

Chapter 4

Coupling Observations with Models

4.1 Introduction

Chapter 2 described the theory behind the formation of the O VI doublet in the corona and introduced an O VI line emission code. Given a solar wind model, this code synthesized O VI emission lines for a specified line of sight. Chapter 3 described the UVCS instrument and the data from which observed O VI lines are obtained, as well as briefly describing an inversion technique to obtain electron density from coronal pB measurements. This chapter employs an iterative inversion technique which successfully couples UVCS O VI observations with the results of the solar wind model, a coupling which, given a specified geometry, enables the calculation of ion outflow velocities, densities and temperatures. This approach proves to be extremely powerful despite its simplicity and the techniques are applied to observations of the solar maximum corona.

Semiempirical modelling is based on the principle of constraining some model parameters by observation, while others are free to take different values. Previous semiempirical modelling of UVCS observations (Cranmer et al., 1999; Strachan et al., 2000; Zangrilli et al., 2002, to name but a few) use observed O VI intensity ratios as a constraint on ion outflow velocities while ion temperatures perpendicular to the solar radial direction are obtained directly from the O VI 1032 linewidth, and ion densities are fixed proportionally to electron density. The scheme used in this chapter adjusts initial estimates of ion outflow velocity, temperature and density until the emission lines obtained from the model closely match the lines of UVCS observations. Thus, in contrast to previous semiempirical modelling, the iterative scheme determines ion density directly from the O

VI intensity, independent of the electron density. The contribution of ion outflow velocity to the linewidth is also absent from the modelled ion temperature.

The iterative scheme is described in section 4.2. It is applied to solar maximum observations of a narrow streamer and a neighboring quiet region in section 4.3. The use of mass flux as a constraint on temperature anisotropy and incident disk spectrum is made in section 4.4, in the context of a large solar maximum active region streamer. Conclusions are given in section 4.5.

4.2 An Iterative Scheme

The iterative scheme can be thought of as an inversion of the line emission equations introduced in chapter 2. In simple terms, the O VI intensity ratio is a function of outflow velocity, the absolute O VI intensity is a function of ion and electron density and O VI linewidth is directly related to the component of temperature along the LOS ($T_\perp$). This is the basis for matching observations with coronal models. Figure 4.1 is a flowchart which illustrates the iterative algorithm. As shown in the 'Given' box in the figure, many parameters are fixed throughout the iterative scheme. Initial estimates of the ion model parameters (ion outflow velocity, density and temperature) are adjusted until a best match between the synthesized and observed lines is found. Complexity arises from the tangled dependence of the parameters - for example, absolute intensity is a function of outflow velocity as well as density and linewidth is a function of outflow velocity as well as temperature (see section 3.6 of chapter 3). Despite this, the algorithm is generally very fast to converge.

If the observed line is well-fitted by a Gaussian, the iterative scheme can be configured to match the 2 main parameters describing the Gaussian (peak intensity and linewidth) and only 3 wavelength points for each line need to be computed at each iteration- the center wavelength λ_0 and the two surrounding wavelengths given by $\lambda_0 \pm \lambda_{1/e}$. For the computed profile to match the target profile, the intensity at the center wavelengths should match the peak intensities of the target profiles and the intensities at the two surrounding points should be $1/e$ of the peak intensity. Computing the whole profile at many wavelengths is therefore redundant, although this is done once after convergence is achieved to obtain the full profile. This greatly improves the efficiency of the algorithm.

Conceptually, this algorithm is similar to that presented by Strachan et al. (2000). However, only the iteration of outflow velocity to match intensity ratio was conducted by the algorithm of Strachan et al. (2000). Their ion temperatures and densities were obtained initially from observed

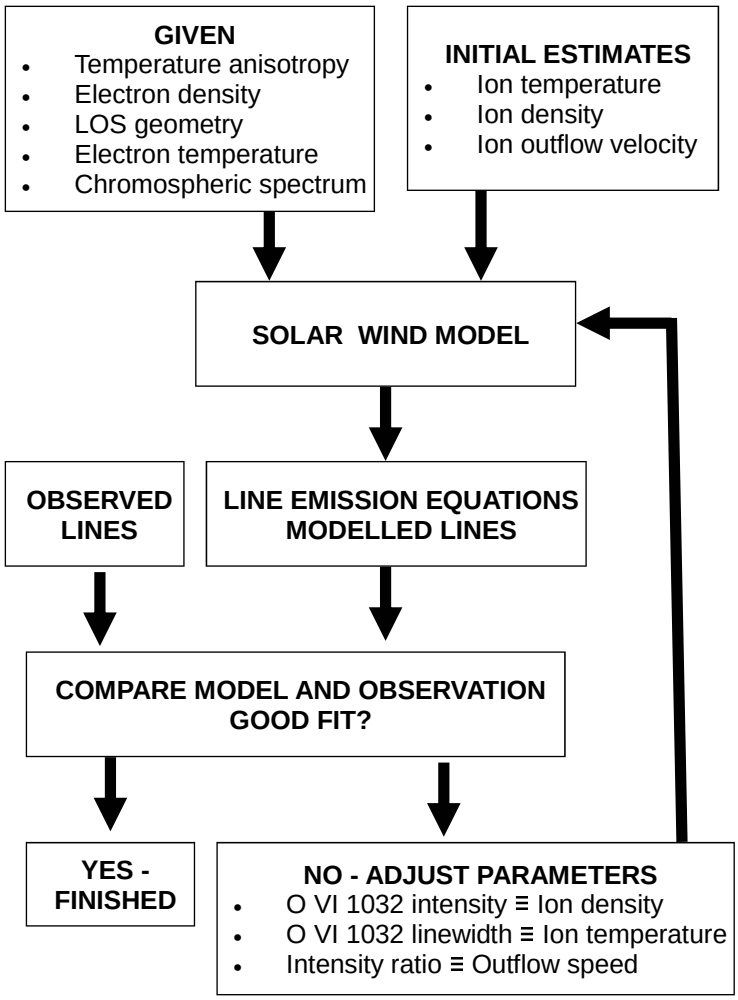

Figure 4.1: A flowchart illustrating the iterative scheme which can derive coronal O VI conditions given some assumed parameters.

linewidths and electron densities, and remained fixed during iteration.

4.2.1 A Brief Test of the Method

The iterative scheme may be tested using contrived line profiles created by the line emission code from a known set of ion parameters. The contrived line profiles are fed into the iteration scheme as targets along with a set of highly inaccurate initial estimates for the ion parameters. Figure 4.2 shows the convergence of the modelled line parameters toward the desired fit of 100%, along with the original and solution line profiles. The solution ion parameters (density, velocity and temperature) match the target ion parameters within 0.3%. This is achieved in 11 iterations.

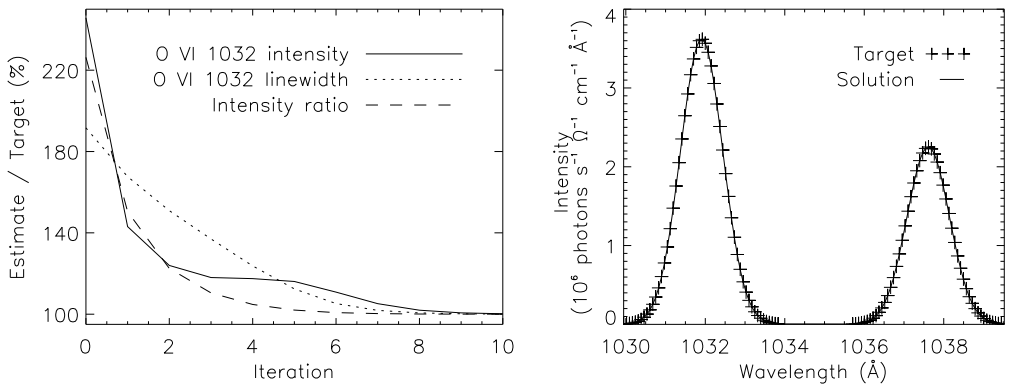

Figure 4.2: *Left* - Convergence of O VI 1032 intensity, linewidth and the 1032/1037 intensity ratio toward the target (100%) as ion parameters are adjusted with each iteration. *Right* - Target profile fed into the iteration model (plus signs) and the resulting solution profile (solid line) found by the iterative scheme.

4.2.2 Non-uniqueness of the Solution

A basic problem with the iterative scheme is the non-uniqueness of the intensity ratio as a function of outflow velocity. In general, if the observed intensity ratio is below 2, there can be 2 or more possible outflow velocities that give the same intensity ratio (see for example figure 2.7 of chapter 2). *A priori* knowledge must be used in these cases and certain constraints placed on the search space of the iterative procedure. Usually, the modelling of several observed heights in the corona can give this knowledge - that is, the outflow velocity is not expected to decrease with increasing height, neither is it expected to shoot up discontinuously. The large difference between two possible solution velocities makes it easy to choose the correct one.

4.3 Plane of Sky Approximation

The plane of sky (POS) approximation refers to a type of geometry that can be used with the solar wind model. The line of sight is ignored in this approximation, under the general physical argument that the largest LOS contribution to the intensity, linewidth and intensity ratio comes from the point closest to the Sun, or in the POS. This approximation is further justified if the object of interest is a high density streamer embedded in the POS and surrounded by regions of lower emission.

This section uses POS geometry to calculate ion densities, outflow velocities and temperatures in a solar maximum south polar streamer and the neighboring region. Firstly, we take two radial slices of the UVCS observations - one within and another outside the streamer. The iterative scheme

is applied to both, with results and the range of uncertainty calculated and discussed. Secondly, we apply the method to 2D contour maps of O VI observables (see section 3.7 of chapter 3) to map modelled ion parameters throughout the region.

4.3.1 Observations

During 2001/01/18-20 observations of a narrow streamer were made by UVCS directly above the south pole. Table 4.1 gives details of the observations and the left panel of figure 4.3 shows the FOV positions overlaid on a white light coronal image. Although useful for placing UVCS observations in their coronal context such a figure can be misleading. The UVCS positions were observed sequentially from the lowest to highest over a period of almost 3 days, while the underlying white light image is a snapshot of the corona taken during 2001/01/19. The solar maximum corona during this period was very active, and from observing movies made from LASCO C2 images, this narrow streamer seemed to be buffeted somewhat by a small ejection around midday on the 19^{th}. Such ejections are commonplace in the solar maximum corona and the streamer remains stable although, as will be discussed, the linewidth of the observation at $5.1R_{\odot}$ seems to be affected. Midday on the 20^{th} sees the beginning of the end for the streamer - it widens and becomes less distinct from the surrounding medium. Three LASCO C2 images are shown in the right panel of figure 4.3. A darker region of lower intensity is seen to the east of the streamer. From EIT images and low resolution coronal hole maps derived from Kitt Peak Helium 10830Å observations there is no obvious sign of a coronal hole in this region.

Two radial slices of the corona are chosen for detailed analysis. The first lies along the axis of the streamer which we label ‘streamer’, the second to the east which we label as ‘non-streamer’. Spatial bins are combined within the streamer and non-streamer regions for each observation. The boundary between the streamer and non-streamer regions is obvious for the three lowest observations from viewing the UVCS O VI intensity across the slit. The boundary is somewhat less clear in the $6.1R_{\odot}$ observation. As can be seen in the bottom right white light image of figure 4.3, the streamer becomes less distinct from the surrounding medium, particularly to the western edge of the UVCS FOV. Nevertheless, there is a distinction between the streamer and the eastern non-streamer region, which is the region chosen for analysis. There is also a peak in intensity in the slit center which shows us the largest streamer contribution at this height. Therefore it is possible to define a streamer

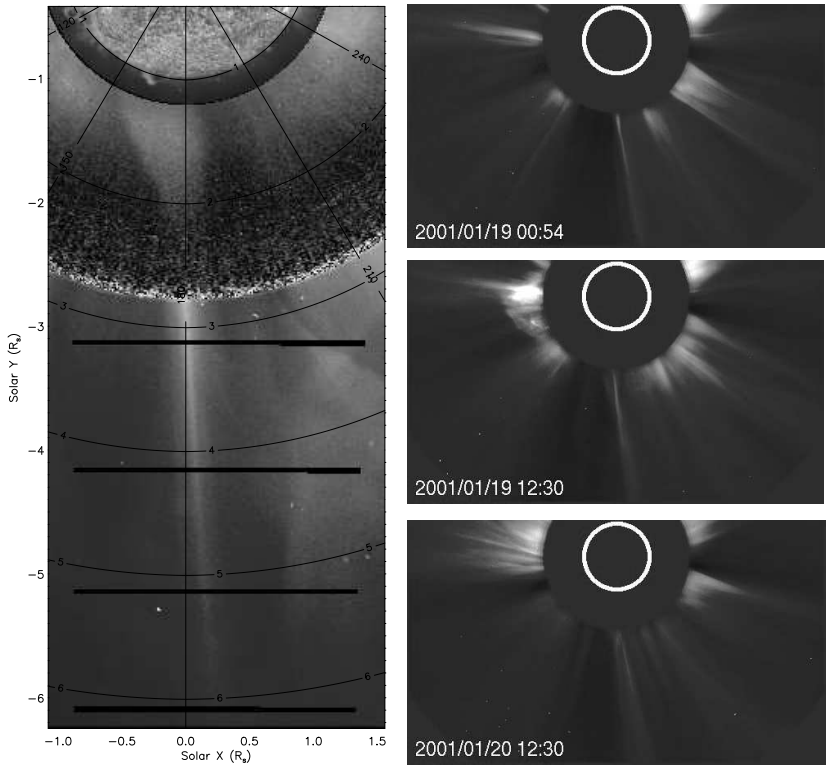

Figure 4.3: *Left* - FOV positions of an UVCS observational sequence conducted during 2001/01/18-20 at slit position angle 180° and heights 3.1, 4.1, 5.1 and 6.1 $R_\odot$. The images of the underlying corona were all observed on 2001/01/19. The white light images are from LASCO C2 (highest region of corona > $2.7R_\odot$) and the Mauna Loa MK IV coronameter (inner region $1.1 - 2.7R_\odot$). The chromosphere is an EIT image of He II at 304Å. A large coronal loop can be seen at the base of the streamer in the EIT image. *Right* - 3 LASCO C2 images of the south corona taken at different times during the 3 days of UVCS observations. From top to bottom - 00:54 on the 19^{th}, 12:30 on the 19^{th} and 12:30 on the 20^{th}. The top image corresponds to the UVCS observations at 3.1 and 4.1 $R_\odot$ and the middle and top to the 5.1 and 6.1 $R_\odot$ observations respectively. The streamer has become wider and more diffuse in the bottom image, 2 hours prior to the end of the final UVCS observation.

and non-streamer region although care must be taken in interpreting results for this observation.

Figure 4.4 shows O VI 1032 and 1037 intensity, 1032 linewidth and the 1032/1037 intensity ratio for both the streamer and non-streamer regions. These will be the values and uncertainties used as targets for the iterative procedure. O VI 1037.6 linewidth is not shown here since it is not a parameter considered in the inversion. The intensity ratio and in particular the linewidth measured in the streamer at height $5.1R_\odot$ are somewhat inconsistent with the measurements at neighboring heights. Figure 4.5 shows the time series of O VI 1032 intensity for the $5.1R_\odot$ streamer observation. There is no abrupt increase and decrease of intensity in this observation that would be conclusive evidence of contamination by a CME. A similar analysis for all the heights observed gives the same null result. Despite this, the conditions in the streamer do change and the LASCO C2 white light

Table 4.1: Details of UVCS observations 2001/01/18-20. Ht and PA are the heights and position angles of the FOV closest to the Sun. Tot exp is the total integrated exposure time. Spat and spect are the spatial and spectral binning respectively. Heights are in $R_\odot$, spatial binning in arcseconds, spectral binning in Å and slit widths in Å.

Start date/time	End date/time	Ht	PA	Tot exp	Spat	Spect	Slit width
18-JAN-2001 16:29	18-JAN-2001 20:32	3.1	180	3 h 42 m	42	0.099	0.6
18-JAN-2001 20:33	19-JAN-2001 02:20	4.2	180	5 h 33 m	42	0.099	0.6
19-JAN-2001 06:22	19-JAN-2001 16:12	5.1	180	9 h	42	0.099	0.6
19-JAN-2001 16:14	20-JAN-2001 02:04	6.1	180	9 h	42	0.099	0.6

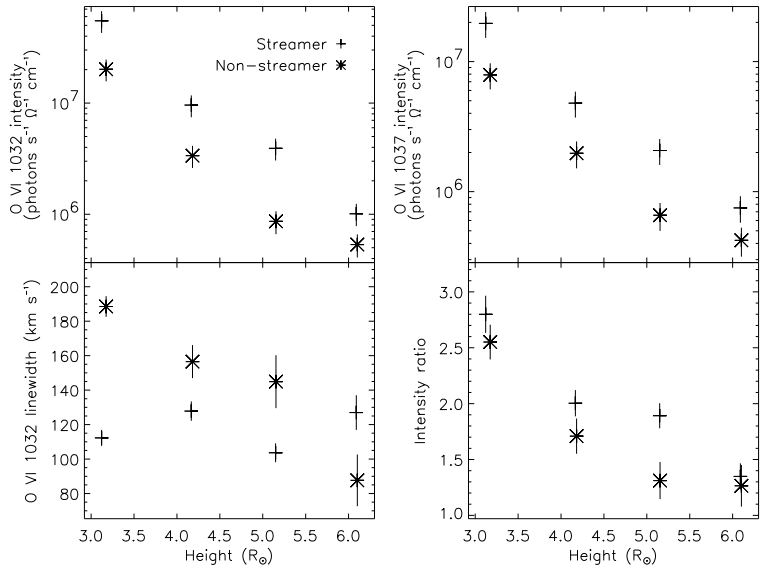

Figure 4.4: O VI 1032 and 1037 intensity, 1032 linewidth and 1032/1037 intensity ratio in the streamer and non-streamer regions for the 2001/01/18-20 observational sequence.

images show the streamer being buffeted by small ejections from 12:00 to 21:00 during 2001/01/19. The smoothed time series in figure 4.5 does show variation which may be due to the small mass ejections seen in white light.

4.3.2 Other Parameters

Electron density is obtained by inversion of LASCO C2 pB measurements made on 2001/01/19 and 20 assuming local spherical symmetry using the methods of Quémerais & Lamy (2002) described in chapter 3. Figure 4.6 shows the electron density obtained in the streamer and non-streamer regions. The UVCS spectral data is integrated over several spatial bins, or a FOV of several arcminutes. For each UVCS observation, electron densities are calculated for many points across the relevant region

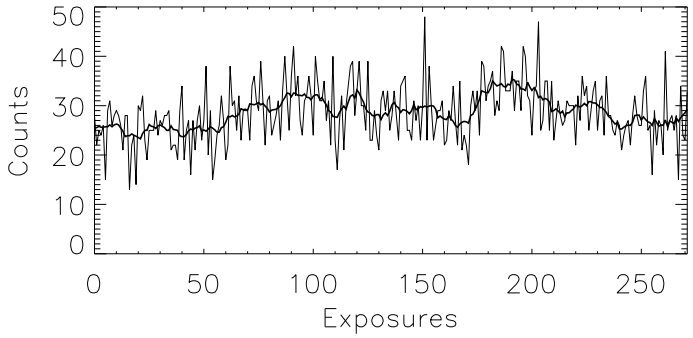

Figure 4.5: O VI 1032 intensity time series for the streamer observation at height $5.1R_{\odot}$. The faint line is the raw counts for each exposure integrated over the streamer spatial bins and the spectral extent of the 1032 line. The thick line is the time series smoothed with a window of 11 exposures. The time series shows no abrupt jump in intensity which would be conclusive evidence of contamination by an ejection.

of the corona. These values give the mean and standard deviation in electron density.

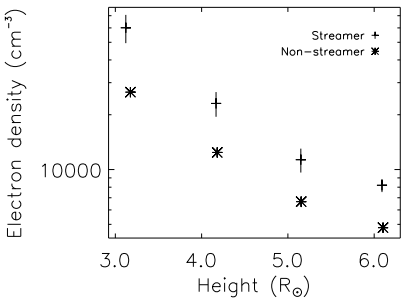

Figure 4.6: Electron density in the streamer and non-streamer regions obtained from LASCO C2 pB measurements.

Electron temperature is set at 1.2×10^6K at all heights. The chromospheric spectrum used is that of the Sumer solar atlas quiet Sun (Curdt et al., 2001) corrected for instrumental broadening as described in chapter 2. The collisional excitation rate coefficients and oscillator strengths are obtained from the Chianti atomic database, also described in chapter 2.

4.3.3 Results and Discussion

Figure 4.7 shows ion densities, outflow velocities and temperatures for both the streamer and non-streamer regions for three different temperature anisotropies, $T_{\parallel} = 0.1T_{\perp}$, $T_{\parallel} = T_{\perp}$ and $T_{\parallel} = 2T_{\perp}$. The model does not allow ion temperature to drop below that of the electrons which is of relevance to the $T_{\parallel} = 0.1T_{\perp}$ case. The uncertainties are calculated directly from the data uncertainties. As an example, the uncertainties in density are not only determined by the uncertainties in 1032 intensity

but also, to a lesser extent, by the uncertainties in intensity ratio and linewidth. Therefore a complete exploration of the limits defined by all the observed uncertainties (1032 intensity and linewidth, intensity ratio and electron density) is made. It is rare for the inaccuracy between observed targets (intensity, intensity ratio and linewidth) and the calculated solutions to be above 0.1%. Any inaccuracy larger than this is due to the inversion attempting to converge to a zero solution, for example, the lower uncertainty calculated for the streamer outflow velocity at height $3.1R_{\odot}$ and the anisotropy of $T_{\parallel} = 2T_{\perp}$ converges to zero and the synthesized intensity ratio has an inaccuracy of about 6%.

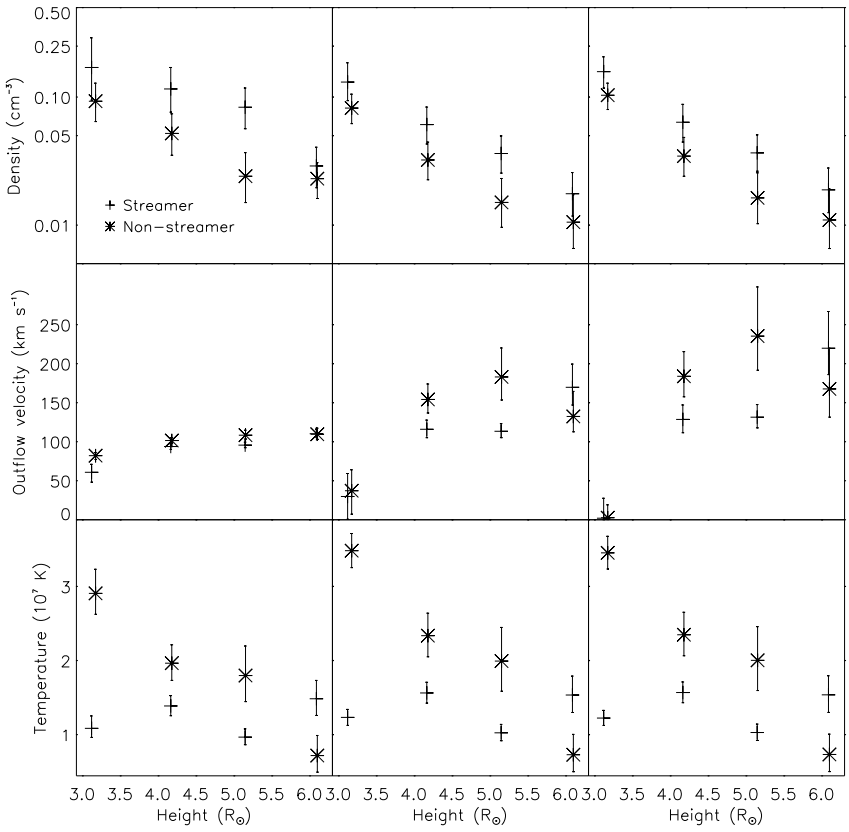

Figure 4.7: Ion densities (top row), outflow velocities (middle row) and temperatures (bottom row) calculated from the 2001/01/18-20 observations. The calculations have been made for three temperature anisotropies, $T_{\parallel} = 0.1T_{\perp}$ (left column), $T_{\parallel} = T_{\perp}$ (middle column) and $T_{\parallel} = 2T_{\perp}$ (right column).

Published work on semi-empirical modelling of solar minimum UVCS observations indicate large contrasts between streamer and coronal hole conditions which are absent in these solar maximum observations. These results show a slow but significant outflow velocity in both streamer and non-streamer regions. A contrast in outflow between the two regions is only apparent at heights of 4.1 and 5.1 $R_{\odot}$ and anisotropies of $T_{\parallel} = T_{\perp}$ and $T_{\parallel} = 2T_{\perp}$. There is no significant difference

between the streamer and non-streamer outflow with a $T_{\|} = 0.1T_{\perp}$ anisotropy since such a low $T_{\|}$ makes the intensity ratio very sensitive to outflow. Temperature remains more or less constant with height in the streamer but decreases by a factor of 4 or more in the non-streamer region. Indeed, the non-streamer temperature at a height of $6.1R_{\odot}$ is around half of that in the streamer.

A further diagnostic which is easily derived from the outflow velocity and density is the mass flux. If a radial expansion of the corona is assumed, the product of mass flux and height squared should remain constant with height. Figure 4.8 shows this mass flux continuity diagnostic for the three modelled anisotropies. The diagnostic seems not to favor an anisotropy of $T_{\|} = 2T_{\perp}$ for either region. An anisotropy of $T_{\|} = 0.1T_{\perp}$ fits the non-streamer well, while the streamer mass flux is most constant with an isotropic temperature. However, the assumption of a radial expansion in a streamer is arguable.

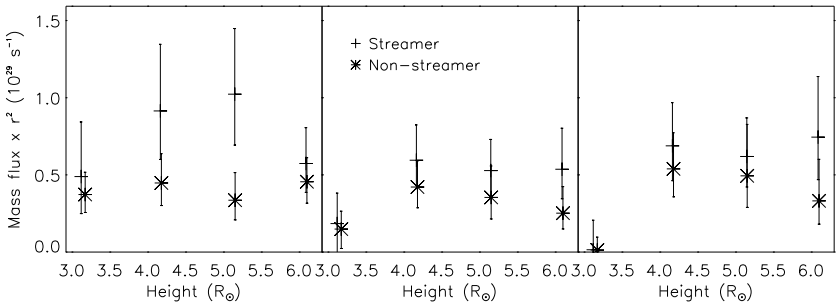

Figure 4.8: Mass flux (density × velocity) multiplied by height squared. The calculations have been made for three temperature anisotropies, $T_{\|} = 0.1T_{\perp}$ (left), $T_{\|} = T_{\perp}$ (middle) and $T_{\|} = 2T_{\perp}$ (right). If a radial expansion is expected of the corona, this value should remain constant at all heights.

The standard approach in the semi-empirical modelling of UVCS observations is to assume a constant ratio of ion to electron density. That is, in the line emission equations of chapter 2 the ion density is usually expressed as the electron density times a constant abundance, A_{i+}. Ion density is a free parameter in the inversion method and it is interesting to compare the derived ion densities with the electron density, as shown in 4.9. For this figure, the electron density is multiplied by A_{i+} so, if the assumption of a constant A_{i+} is correct, the comparison should be close to unity at all heights.

The $T_{\|} = 0.1T_{\perp}$ anisotropy (left plot) has resulted in rather large variations in ion to electron density ratio, particularly in the streamer values. The isotropic and $T_{\|} = 2T_{\perp}$ cases (middle and right plots) show values close to unity given the uncertainties for both streamer and non-streamer regions. There is a downward trend in ion over electron density ratio with height in the non-streamer region. This can be expected if the O VI ions are accelerated more than the electrons. The steeper radial

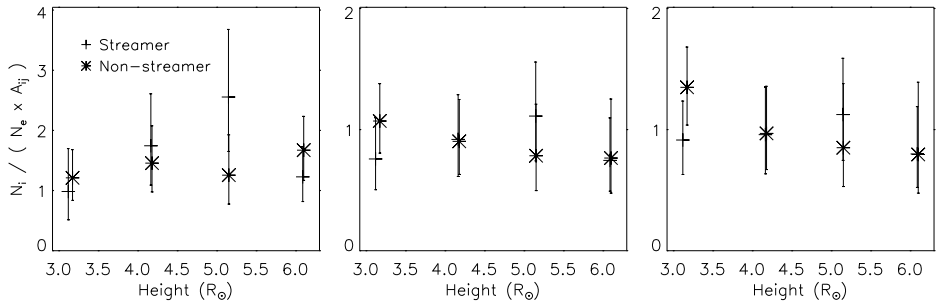

Figure 4.9: The ratio of ion density to electron density times A_{i+}. The calculations have been made for an electron temperature of 1.2×10^6K and three ion temperature anisotropies, $T_\parallel = 0.1T_\perp$ (left), $T_\parallel = T_\perp$ (middle) and $T_\parallel = 2T_\perp$ (right).

outflow velocity gradient would mean a lessening of the abundance of O VI ions in comparison to the background plasma. In light of this statement, the ion to electron density ratio should be lower than the tabulated value of A_{i+} at a height of $3.1R_\odot$ if there has been preferential acceleration of O VI ions below this height.

The ion to electron density ratio given by the inversion method, although reassuringly close to the tabulated values of the Chianti database abundances and ion equilibria, is sensitive to the choice of certain assumed parameters. The tabulated values of ion to electron density ratio A_{i+} is a function of electron temperature which has been assumed for these calculations as 1.2×10^6K. A lower T_e of 10^6K would mean a ~27% increase in A_{i+}. The collisional excitation rate coefficient q_c is also a function of T_e and the collisional component has higher intensity with decreasing T_e. Despite this, repeating the inversion calculations with a T_e of 10^6K results in ion densities, outflow and temperatures very close to those calculated for the higher T_e. Therefore a 27% increase in A_{i+} at a lower T_e results in a similar decrease of the values plotted in figure 4.9.

4.3.4 Conclusion

The inversion method has been successful in calculating ion densities, outflows and temperatures in a solar maximum streamer and a neighboring non-streamer region. Both regions have a slow but significant ion outflow which increases between 3.1 and $5.1R_\odot$. Using the calculated mass flux and an assumption of a radially expanding corona, a $T_\parallel = 2T_\perp$ ion temperature anisotropy is shown to be unlikely. A $T_\parallel = 0.1T_\perp$ anisotropy gives the best mass flux constant for the non-streamer region. The mass flux is not so well preserved in the streamer. This may be due to the non-radial expansion of the streamer or due to disturbances caused by the small ejections discussed earlier. The inversion

derives ion densities directly from the O VI 1032 line intensity, and a comparison with the standard abundance value for O VI has shown a non-constant ion to electron density ratio with height which may reflect a preferential acceleration of the heavy ions.

The complex structure and dynamic nature of the solar maximum corona makes the interpretation of results difficult in comparison to studies of the solar minimum corona. As shown, there is far less contrast between streamers and surrounding regions. The non-streamer region of this study does not possess coronal hole conditions, but is significantly different from the streamer in most parameters. Some regions of the solar maximum corona can not, in UVCS observations, be associated with coronal holes nor streamers, and may best be defined as the quiet corona. The modelling of quiet coronal regions and of the solar maximum corona in general is lacking, and warrants far more analysis of the observations already made by UVCS.

4.3.5 2D Maps of Ion Parameters

Measurements of the 2001/01/18-20 South pole streamer positions are slightly different in the pre-processed LASCO and UVCS data. This is due to the different dates of observation, the changing nature of the corona and calibration uncertainties. A good co-registration of the electron map to the UVCS observations is made possible using a cross correlation between O VI 1032 intensity and the LASCO pB. A few degrees adjustment of the original LASCO latitude is needed to align the streamer with each UVCS observation. Figure 4.10 shows contour maps of UVCS observables and electron density for the whole south polar region between 3.1 and $5.1R_{\odot}$. The UVCS maps have been created using the techniques of UVCS FOV spatial sliding windows and interpolation described in chapter 3. The electron density map is created from the LASCO C2 2001/01/20 pB observation. Using the plane of sky inversion these maps of observables will be used to create maps of modelled ion parameters across the whole region.

Given a good spatial co-registration between UVCS and LASCO observations a secondary concern is the integration of UVCS spatial bins, particularly with the higher observations, which widens coronal features such as streamers across the slit. Because of this, the streamer is far narrower and distinct in electron density compared with the O VI intensity and the electron density gives a truer impression of the coronal structure. The combining of UVCS spatial bins is essential to achieve a good signal to noise. This is why the $6.1R_{\odot}$ observation has been omitted from the contour maps

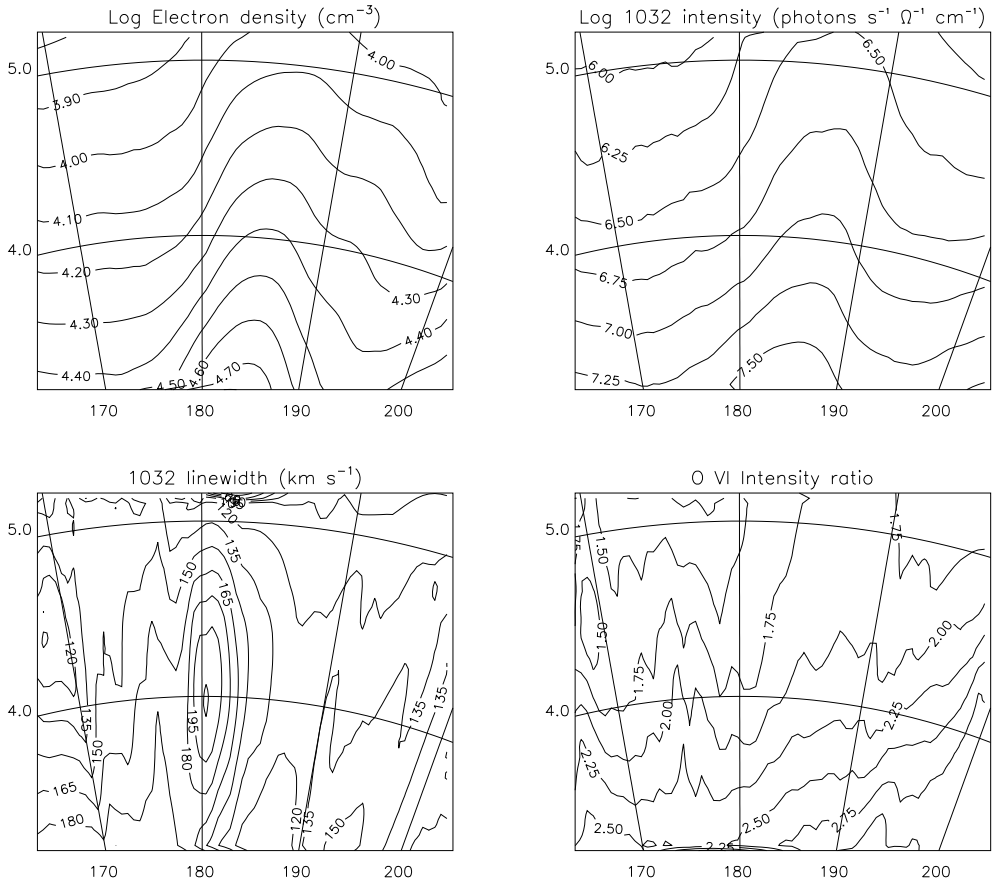

Figure 4.10: Contour maps of LASCO electron density and UVCS observables for the south polar region of 2001/01/18-20. The electron density is smoothed to be consistent with the necessary smoothing of the UVCS data (see text) and the original LASCO co-ordinates have been adjusted to achieve the best spatial co-registration with UVCS. The x-axis labels are position angles and the y-axis labels are heights.

- the streamer is almost indiscernible due to the wide spatial binning. An attempt to deconvolve the effect of combining spatial bins, similar to a spectral deconvolution, leads to unphysical results and further research needs to be done on this matter. In particular, a method that uses the LASCO pB profile as a guide to sharpening spatial features in the UVCS data can be envisaged but is not attempted here. A simple but somewhat unsatisfactory approach to achieve consistency is to smooth the LASCO data in a similar way to UVCS.

Figure 4.11 shows ion density, outflow, temperature and radial mass flux continuity for the south polar region. Ion parameters show considerable variation between the streamer and areas to lower latitudes ($< 180°$). The areas at lower latitudes coincide with the darkest areas of the white light images of figure 4.3. As expected, the ion density profile closely resembles the O VI intensity and electron density. The outflow velocity at latitudes higher than the streamer ($> 190°$) is interesting in

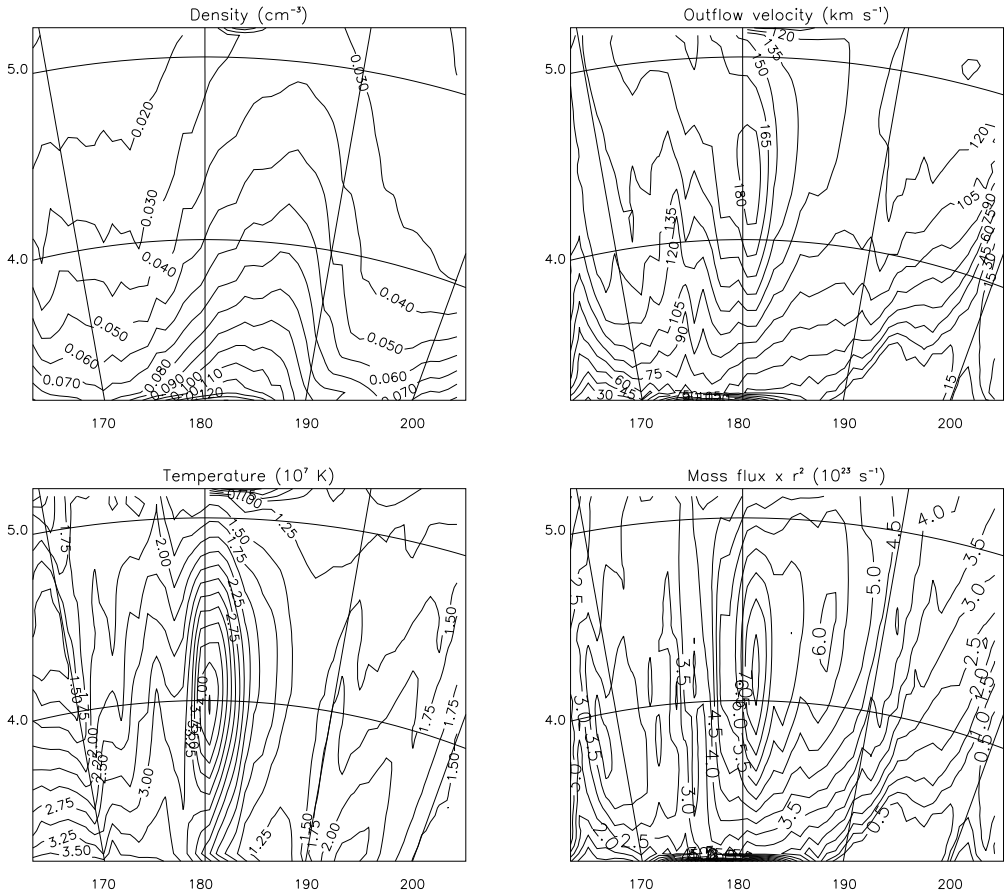

Figure 4.11: Maps of ion density, outflow velocity, temperature and radial mass flux continuity times height squared calculated by inversion from the observables in figure 4.10 under the assumption of isotropic temperature distribution. The x-axis labels are position angles and the y-axis labels are heights.

that it reaches a minimum at latitudes of $\sim 200°$. It can be seen in the white light images of figure 4.3 that this minimum in outflow coincides with the edge of a broad streamer. There is also an increase in ion and electron density to this side of the maps. The contours of mass flux continuity ($n_i u r^2$ where u is outflow velocity and r is the height) should all follow radial paths if the assumption of radial expansion is true. In this case most of the region has reasonably radial contours. Repeating the inversion with different temperature anisotropies may improve the mass flux continuity, although, as mentioned previously, the solar maximum corona should not be expected to expand radially in all regions.

Maps of large regions of the corona interpolated from UVCS observations are useful for discerning large scale coronal features and enable swift comparison with white light images. Applying the plane of sky inversion to such maps results in detailed images of heavy ion conditions. These

images are a powerful extension of spectral observations and can offer a new frame of reference for the recent advances in 2D numerical models of the corona.

4.4 Mass Flux as a Constraint on Assumed Parameters

This section follows the same format as the previous section and applies the same techniques to solar maximum UVCS and LASCO observations of a large North-Eastern streamer complex. It is shown that the model fails completely to match observation at lower heights except with a temperature anisotropy of $T_| = 0.1T_\perp$. Other temperature anisotropies lead to intensity ratios that are far too low compared to the observed and the inversion attempts to converge to zero velocities regardless of the choice of electron temperature. However, incorporating emission from sunspots into the incident disk radiation greatly increases the modelled intensity ratio at low velocities. This allows the model to easily converge to non-zero velocities. A study of the mass flux through all the observed heights allows us to constrain the degree of contribution from sunspots in the disk spectrum. At low heights, derived ion outflow velocities and densities are very sensitive to the incident disk spectrum and the mass flux proves to be useful in improving the solar wind diagnostics.

4.4.1 Observations

During 2000/01/28-29 UVCS made five observations of a wide streamer 35° North of solar East. Table 4.1 gives details of the observations. Figure 4.12 shows the positions of the UVCS FOV overlaid on white light images of the corona. In the processed white light image, the streamer or streamer complex is very broad and extends radially outwards covering a > 30° range of latitudes and filling the UVCS FOV completely. The O VI lines are therefore reasonably clean even at a height of $8R_\odot$. UVCS observations at these heights are rare and only useful in a streamer.

Table 4.2: Details of UVCS observations 2000/01/28-29. See table 4.1 for description of terms and units.

Start date/time	End date/time	Ht	PA	Tot exp	Spat	Spect	Slit width
28-JAN-2000 23:15	29-JAN-2000 00:51	3.1	55	1 h 24 m	46	0.099	0.1
29-JAN-2000 00:54	29-JAN-2000 03:30	4.6	55	2 h 30 m	46	0.099	0.2
29-JAN-2000 03:32	29-JAN-2000 07:36	6.1	55	3 h 48 m	46	0.099	0.3
29-JAN-2000 07:38	29-JAN-2000 17:07	7.0	55	6 h	46	0.099	0.3
29-JAN-2000 17:09	30-JAN-2000 04:00	8.0	55	10 h 6 m	46	0.099	0.3

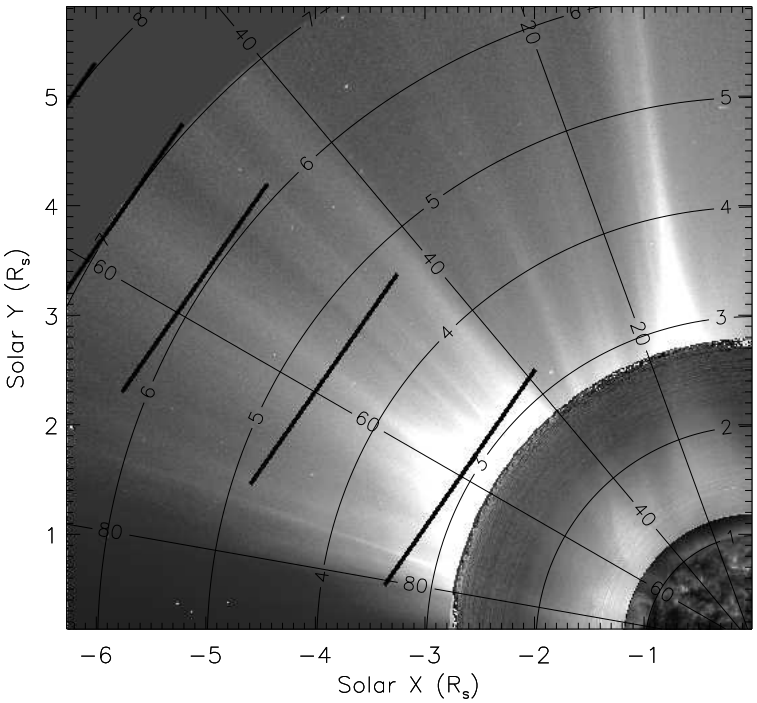

Figure 4.12: FOV positions of an UVCS observational sequence conducted during 2001/00/28-29 at slit position angle 55° and heights 3.1, 4.6, 6.1, 7.0 and 8.0 $R_{\odot}$. The white light images are from LASCO C2 and the Mauna Loa MK IV coronameter, both observed on the 29^{th}. The chromosphere is an EIT image of Fe IX/X at 171Å observed on the 28^{th}. Unfortunately the UVCS FOVs at 7.0 and 8.0 $R_{\odot}$ extend beyond the FOV of LASCO C2.

The streamer remains stable throughout the observation and from viewing LASCO C2 movies there are no evident signs of coronal ejections. Due to solar rotation, the bulk of the streamer is moving slowly to higher latitudes throughout the observational period. This suggests that it is aligned toward the observer and rooted at the near side of the Sun. This general upward movement only becomes apparent on the 28^{th}. On the 26^{th} and 27^{th} there is no apparent large-scale movement and prior to the 26^{th} the bulk of the streamer moves slowly to lower latitudes. Assuming a radial extension of the streamer from the Sun, this crudely places the main base of the streamer at the limb of the Sun during 2000/01/26-27. Figure 4.13 (top) shows a daily sequence of EIT He II 304Å images starting on 2000/01/30 which shows an intense active region moving from the limb toward the central meridian. Quarter of a solar rotation is just under 7 days and the active region seen in the EIT images reaches the central meridian early on 2000/02/03, most clearly seen in the meridianal Carrington map of EIT 284Å (middle figure of 4.13). This strongly associates this active region with the main streamer activity seen in the LASCO C2 images. Associated with the active region is a large sunspot complex seen in the Michelson Doppler Imager (MDI) image of figure 4.13. The

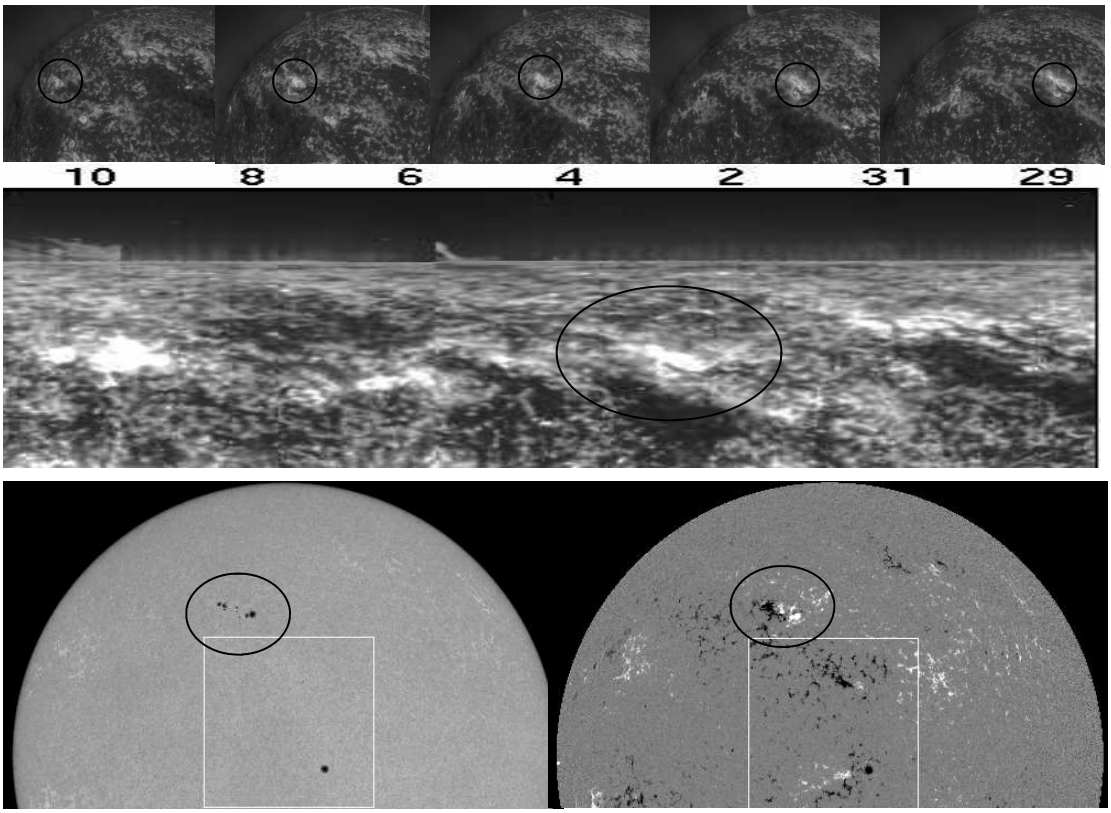

Figure 4.13: *Top row* - Sequence of EIT He II 304Å images of the North-East chromosphere taken daily from 2000/01/30 - 2000/02/03. The circled active region moves with solar rotation from the limb toward the meridian. *Middle* - meridian Carrington map of EIT He II 304Å from dates 2000/01/29 to 2000/02/11. Only the North hemisphere is shown. *Bottom* - two images of the Northern disk taken by the Michelson Doppler Imager (MDI) aboard SOHO on 2000/02/02. The left image is intensity centered on the Ni I photospheric absorption line at 6768Å, useful for seeing the position of sunspots at the base of the active region. The right image is a magnetogram which shows magnetic activity and polarity. The active region of interest is circled in all images.

LASCO C2 images show a large angular extent to the streamer. It is also apparent from C2 movies that the whole streamer complex does not move with solar rotation in the same way. It would be wrong therefore to associate all the streamers in the North-Eastern corona with the one obvious active region circled in the EIT images. The Carrington map shows other regions of activity leading and following the one under discussion.

UVCS spatial bins are integrated from the section of the FOV surrounding the 55° position angle. The data have a decent photon count even at large heights due to the long observation times and high streamer intensity, although a larger section of the FOV is integrated at the higher observations to compensate for the drop in intensity. Figure 4.14 shows O VI 1032 and 1037 intensity, 1032 linewidth and 1032/1037 intensity ratio for the UVCS observations and electron density obtained

from observations of pB by LASCO C2 on 2000/01/29. $V_{1/e}$ has a slow linear increase from 90 to 150 km s^{-1}. The intensity ratio has an interesting profile in that the value at $7R_\odot$ has a very similar value to the observation at $6.1R_\odot$ before decreasing for the $8R_\odot$ observation. At first glance, this may be a sign of a low parallel temperature and an outflow velocity above $\sim$ 300 km s^{-1}, both of which are needed to create a double-trough profile to the intensity ratio as a function of outflow (see for example figure 2.7 of chapter 2).

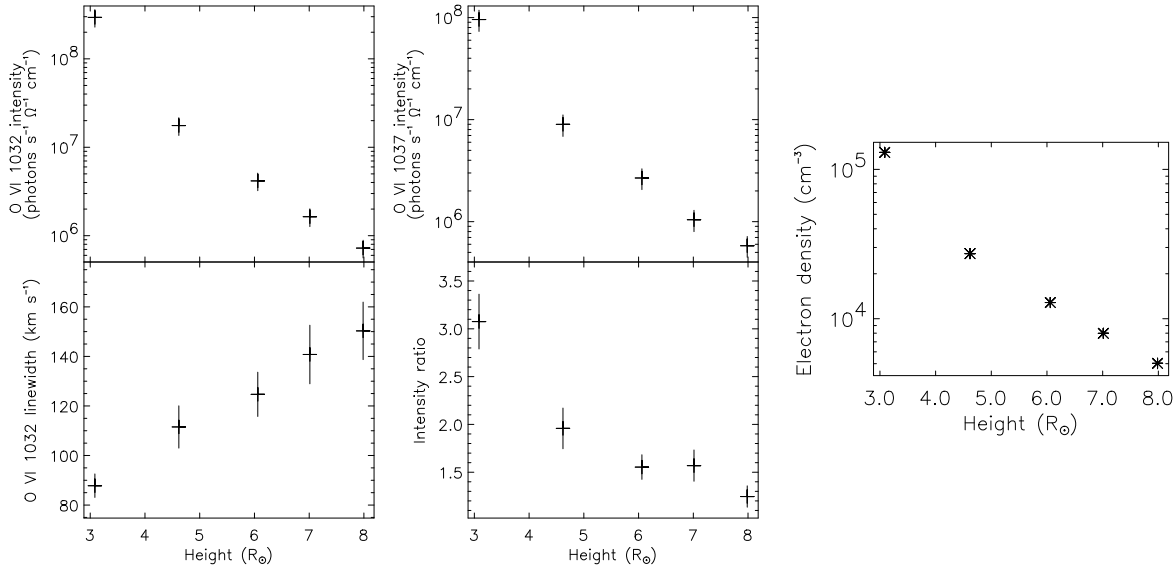

Figure 4.14: *Left and middle columns* - O VI 1032 and 1037 intensity, 1032 linewidth and 1032/1037 intensity ratio for the 2001/01/18-20 observational sequence. *Right* - electron density obtained by inversion of LASCO C2 pB measurements.

4.4.2 Results and Discussion

Figure 4.15 shows O^{5+} density, outflow velocity and mass flux calculated by inversion of the 2000/01/28-29 data using a POS approximation, the quiet Sun incident spectrum of the SUMER solar atlas, a T_e of 1.2×10^6K and a temperature anisotropy of $T_\parallel = 0.1T_\perp$. Other temperature anisotropies ($T_\parallel > 0.1T_\perp$) do not converge at the lowest height and a $T_\parallel = 0.1T_\perp$ anisotropy only converges to the lower uncertainty in the observed intensity ratio. The observed intensity ratio is $3.1 \pm 9\%$ and the model fails to reach a value of 3.1 even at zero velocities. Raising the electron temperature decreases the collisional component, and can change the behaviour of intensity ratio with outflow velocity (see section 2.6 of chapter 2). Repeating the calculations with various electron temperatures between $1.2 - 2.5 \times 10^6$K does not improve the fit at the lowest height. This is because

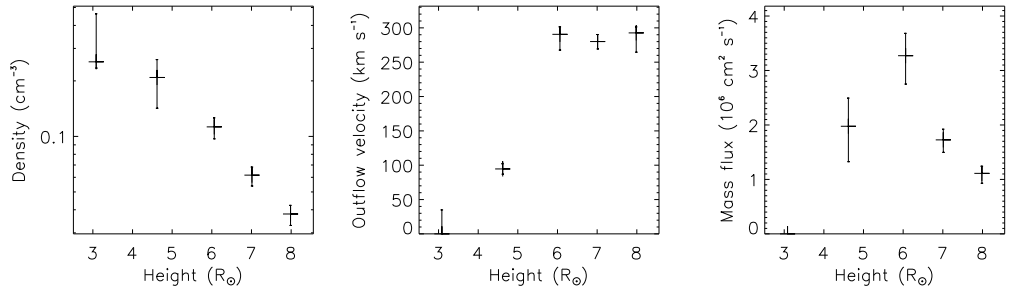

Figure 4.15: Ion density (left), outflow velocity (middle) and mass flux (right) calculated from the 2000/01/28-29 observations. The calculations have been made for a temperature anisotropy of $T_{\parallel} = 0.1T_{\perp}$. Other temperature anisotropies ($T_{\parallel} > 0.1T_{\perp}$) do not converge at the lowest height. Note that we show here the actual mass flux and not mass flux times height squared as in section 4.3.

the intensity is radiatively dominated regardless of T_e at these heights in streamers. The mass flux shown in figure 4.15 is also unconvincing. It increases to a maximum at $6R_{\odot}$ before decreasing in a more physical manner. Note that figure 4.15 shows the actual mass flux ($n_i u$, where u is the outflow velocity and n_i is density) and not radial mass flux continuity ($n_i u r^2$, where r is height).

Limb brightening is an increase in the intensity of the disk emission from the center of the Sun toward the limb. In a uniform Sun, there is a $1/\cos\theta$ increase in intensity (Gabriel et al., 2003), where θ is the angle between the local normal to the surface and the radial line from Sun center to the emission volume in the corona. At a height of $3R_{\odot}$, $1/\cos\theta$ has a maximum value of 1.05 and incorporating limb brightening in our calculations does not increase the modelled intensity ratios enough to significantly improve the mass flux diagnostic.

The O VI disk emission measured from a sunspot is drastically different from the quiet Sun emission (Curdt et al., 2001). The lines are around 60 times more intense, and the peak 1032/1037 intensity ratio is increased from 2 to 2.5 or higher while the C II lines remain largely unchanged from the quiet Sun spectrum. The increase in the intensity ratio of the O VI doublet suggests that non-collisional excitation processes are taking place in the locality of sunspots. Curdt et al. (2000) discuss the possibility of a continuous stream of material flowing into sunspots under the high magnetic field conditions, and colliding with denser material. The MDI images shown in figure 4.13 show clearly the presence of a sunspot region which can be associated with the observed streamer. Since the sunspot spectrum is so intense in O VI, even a small area of sunspots makes a large difference in the modelling of the coronal lines. We recalculate ion parameters with varying degrees of contributions from sunspots included in the disk spectrum. Including a sunspot contribution in

the incident radiation of the model increases the values of the intensity ratio at low velocities and allows the model to converge to non-zero outflow.

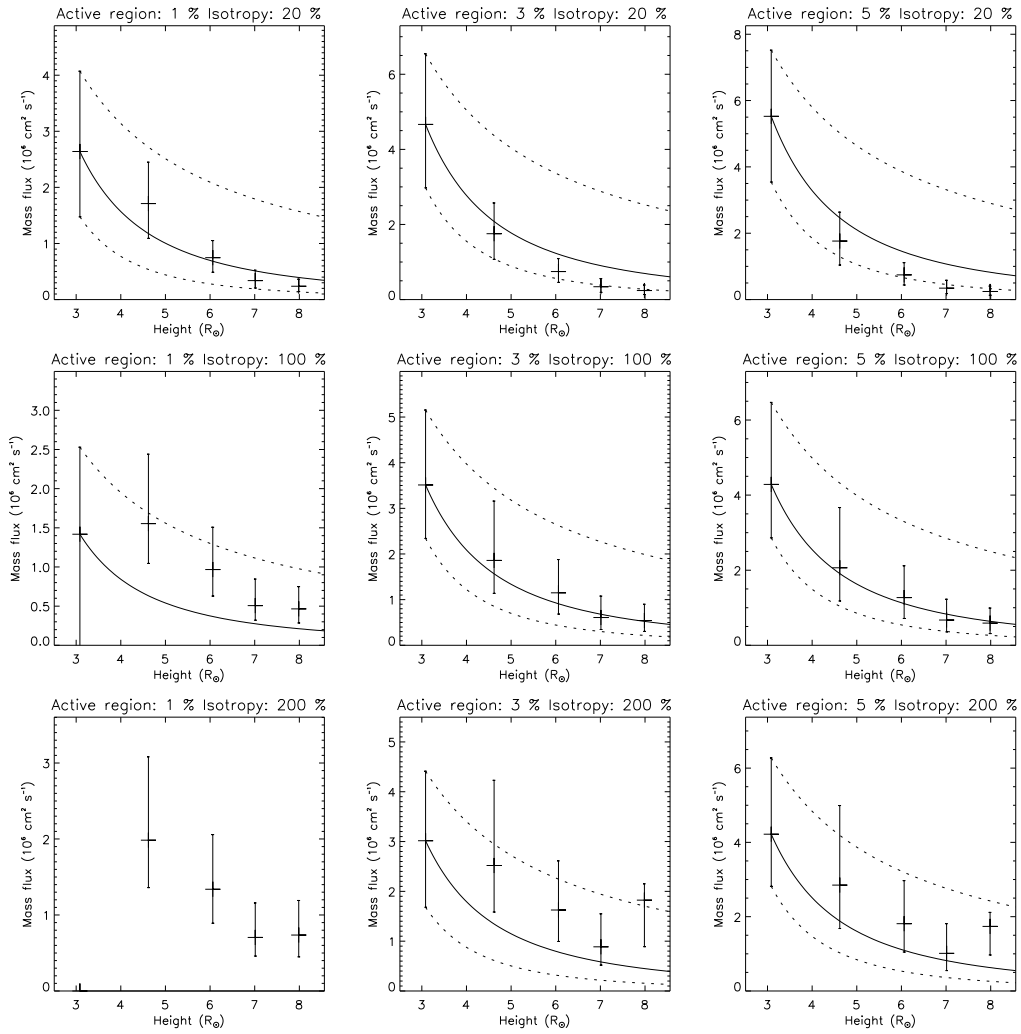

Figure 4.16: Mass flux calculated for 3 different temperature anisotropies and 3 varying degrees of contributions from sunspots. The plot titles refer to percentage of the disk radiation given by the sunspot emission and the percentage of $T_{\parallel}$ compared to $T_{\perp}$. The solid line shows the expected mass flux from a r^{-2} (radial) expansion of solar wind, with a boundary value given by the calculated mass flux at $3.1R_{\odot}$. The upper dashed lines show mass flux from a r^{-1} (sub-radial) expansion with a boundary value of the higher uncertainty of the mass flux at $3.1R_{\odot}$. The lower dashed lines show mass flux from a $r^{-2.5}$ (super-radial) expansion with a boundary value of the lower uncertainty of the mass flux at $3.1R_{\odot}$. Physical solutions of O VI parameters will give a mass flux which falls within the dashed lines at all heights. The solution for outflow velocity at $3.1R_{\odot}$ for the lower left plot has not converged.

Figure 4.16 shows mass flux calculated for various permutations of temperature anisotropy and degree of contribution from sunspots. The two dashed lines shown in each plot give the extreme limits of mass flux continuity and are described in the caption. Physical solutions of O VI parameters

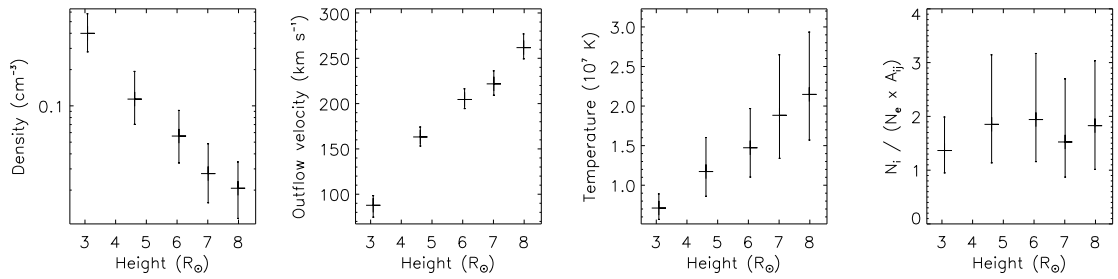

Figure 4.17: *Left to right* - Ion density, outflow velocity, temperature and ion density over electron density times the theoretical abundance calculated from the 2000/01/28-29 observations. The calculations have been made for isotropic temperatures, a T_e of 1.2×10^6K and a chromospheric spectrum with 3% contribution from sunspots.

should fall within these lines at all heights. Additionally, the mass flux should not increase with height. This discounts a temperature anisotropy of $T_{\parallel} = 2T_{\perp}$ (bottom row) at all values of sunspot contributions and discounts an isotropic temperature with a 1% sunspot contribution. Temperature anisotropies of $T_{\parallel} = 0.2T_{\perp}$ are valid but show a super-radial expansion. This is not expected from the traditional views of streamer geometry. An isotropic temperature distribution with a 3 or 5% contribution from sunspots fits the radial expansion curve closely.

The constrained values of disk emission (3% contribution from sunspots) and velocity distribution (isotropic) are used to calculate the O VI parameters of figure 4.17. The outflow velocity and temperature increase linearly with height even up to the highest observation at $8R_{\odot}$ which suggests that energy is deposited in the streamer plasma even this far from the Sun. The O VI abundances are significantly above the theoretical values of the CHIANTI database. The electron temperature of 1.2×10^6K used for the calculations is likely to be at the lower limit for streamers. Increasing T_e decreases the theoretical abundance and has only a small effect on our calculations due to the dominance of the radiative component at these low velocities. Therefore, using a higher streamer value for T_e would increase the difference between the calculated and theoretical O VI densities. There is no consistent decrease of the ion to electron density ratio with height. It is likely therefore that there is no preferential acceleration of the O VI compared to the electrons in this streamer.

4.4.3 Conclusions

As discussed in chapter 1, previous modelling of UVCS solar minimum streamer observations has suggested that there is no significant outflow of O VI above 20 km s^{-1} in solar minimum equatorial streamers below heights of ~$3.5R_{\odot}$ (Strachan et al., 2002). Such modelling has also shown an abrupt

increase in the outflow velocity above this height. These published results have been used to support the standard view of streamer magnetic field structure - the O VI ions have zero outflow below $3.5R_{\odot}$ in the streamer due to closed magnetic field structures, and the abrupt rise in outflow is due to plasma escaping above the streamer cusp. In future work, these solar minimum observations should be re-examined using the iterative inversion techniques presented in this chapter. The presence of active regions or sunspots on the disk may well result in non-zero outflow velocities at lower heights in solar minimum streamers.

This section has shown that any realistic modelling of observed coronal O VI lines must include a sunspot contribution in the incident disk spectrum if sunspots are known to be present. Sunspots on the disk are a far more important consideration than factors such as limb brightening, particularly at these heights. In the streamer observations modelled here, a contribution from sunspots in the incident disk radiation gives solutions that have a consistent and realistic mass flux with increasing height. Without a sunspot contribution, outflow velocities converge to zero at low heights.

Computing the mass flux for many permutations of temperature anisotropy and sunspot contribution leads to constraints on these previously assumed values. These constraints give better confidence in the resulting ion parameters and it is shown that the abundance of O VI in the streamer is significantly higher than theoretical values at all heights, despite the low value of electron temperature used in the calculations. O VI outflow and temperature increase linearly with height within the streamer up to the highest range of observation, $8R_{\odot}$. There is no evidence of preferential acceleration of O VI in this streamer.

4.5 Conclusions

The iterative inversion scheme is only possible due to the corona being optically thin. The decrease of density with height has also allowed the use of a plane of sky approximation which greatly reduces computational complexity and time. This approach is most valid when modelling observations of streamers, since their intensity dominates the line of sight. The strength of the iterative scheme in comparison to other semiempirical models is that it makes full use of the data, therefore minimizing the dependence of modelling on assumed parameters. At large heights in the corona, which preferentially accelerates heavy ions, it is logical to believe that the ion densities should not be directly proportional to the electron densities. The inversion method allows us to test such state-

ments simply by comparing ion and electron densities. Mass flux becomes a diagnostic which can constrain temperature anisotropy and improve the assumed value of disk emission.

The weakness of the inversion technique lies in its use of the observed absolute intensities to derive ion densities. This places a heavy dependence on the radiometric calibration of the instrument. The 22% calibration uncertainty of UVCS leads directly to at least a 22% uncertainty in derived ion densities. Line of sight geometry is another problem area with the inversion. In this chapter, the POS approximation is used mostly with streamer observations. This approximation is not a good one to use with coronal hole or quiet coronal observations. In such cases a spherically symmetric geometry would be more appropriate. This is discussed in the following chapter.

Chapter 5

The Linewidth Ratio of the O VI 1032 and 1037.6 Å Doublet

5.1 Introduction

A significant difference in the linewidths of the O VI doublet at 1031.9 and 1037.6 Å can often be seen in UVCS observations. An exploration of the linewidth ratio of the doublet is made through the calculation of coronal line emission from a spherically symmetric solar wind model. It is shown that many combinations of outflow velocity and temperature anisotropy can lead to considerable differences in linewidths due primarily to the different balance of radiative and collisional components in each line. This balance changes with Doppler dimming and pumping so the linewidth ratio is sensitive to outflow velocity. The linewidth ratio is also sensitive to the temperature anisotropy and the gradient of outflow velocity along the line of sight (LOS). In the previous chapter it was shown that an inversion technique using a geometrical plane of sky (POS) approximation could derive O VI density, outflow velocity and temperature by satisfying the observational constraints of O VI 1032 intensity, linewidth and the 1032/1037 intensity ratio. The modelled 1037 linewidths however do not fall within the constraints of the observed values and the result of the parameter study conducted in this chapter suggests that the 1032/1037 linewidth ratio may provide an extra constraint in extending the inversion technique to a more complex LOS geometry.

Using the Doppler dimming technique, the O VI intensity ratio can be used as evidence of bulk outflow velocity of O VI ions from the Sun (Kohl & Withbroe, 1982; Withbroe et al., 1982; Noci et

al., 1987; Li et al., 1998). The modelling of coronal line emission can lead to large uncertainties in the final estimation of outflow velocity since some parameters are not directly measured by present observations and these values must be assumed (Antonucci et al., 2004; Frazin et al., 2003; Strachan et al., 2002; Zangrilli et al., 2002). Most notably, temperature parallel to the predominately radial coronal magnetic field must be assumed since observed linewidths only give a measure of the temperature along the LOS perpendicular to the magnetic field. The intensity ratio can in some cases give some constraint to the values of temperature anisotropy but any additional constraint would be valuable in the interpretation of UVCS O VI observations.

Frazin et al. (2003) note a significant difference in the linewidths of the O VI doublet lines in an equatorial streamer and postulate the following two physical causes: 1. Inhomogeneity in ion temperature along the LOS coupled with different radiative to collisional contributions to the line or 2. non bi-Maxwellian velocity distributions.

The ratio of the 1032 linewidth over the 1037.6 linewidth is a value which facilitates exploration of the linewidth difference. Line emission is simulated from a LOS through a spherically symmetric solar wind model. It is shown that the linewidth ratio is strongly affected by Doppler dimming and pumping due simply to the different widths of the collisional and radiative components and regardless of temperature inhomogeneities along the LOS. With bi-Maxwellian velocity distributions and no temperature gradients or inhomogeneities the linewidth ratio can vary as a function of outflow speed from ~0.8-1.3 at a height of $3R_{\odot}$. Examples of observed difference in linewidth are given in section 5.2. The model is described in section 5.3. Linewidth ratio is calculated as a function of various parameters and the results are presented and discussed in section 5.4. Implications for the inversion technique introduced in chapter 4 are given in section 5.5 and concluding remarks are made in section 5.6.

5.2 Observation

Figure 5.1 shows the slit position of an UVCS observation from 2000/05/07 overlaid on a composite EIT 284Å LASCO C2 and Mauna Loa MK IV coronameter vignetted white light images. EIT and LASCO C2 movies indicate no explosive events to disturb the relevant regions of the corona during the 156 minute observing period. The center of the UVCS field of view is at a height of $3.1R_{\odot}$ and position angle 170°. Data were collected using the O VI channel with a spectral binning of

1 pixel (0.0993 Å). The slit width is 153μm. The spatial binning is 6 pixels (42”), thus yielding 60 spatial bins across the slit. The few spatial pixels at the extremities of the slit, which give unreliable readings, are rejected. The observation consists of a series of 2 minute exposures which are combined. It is necessary to improve signal to noise by combining slit bins. A sliding window of 9 pixels is used in this case. The sliding window and all other relevant data analysis techniques are described in chapter 3.

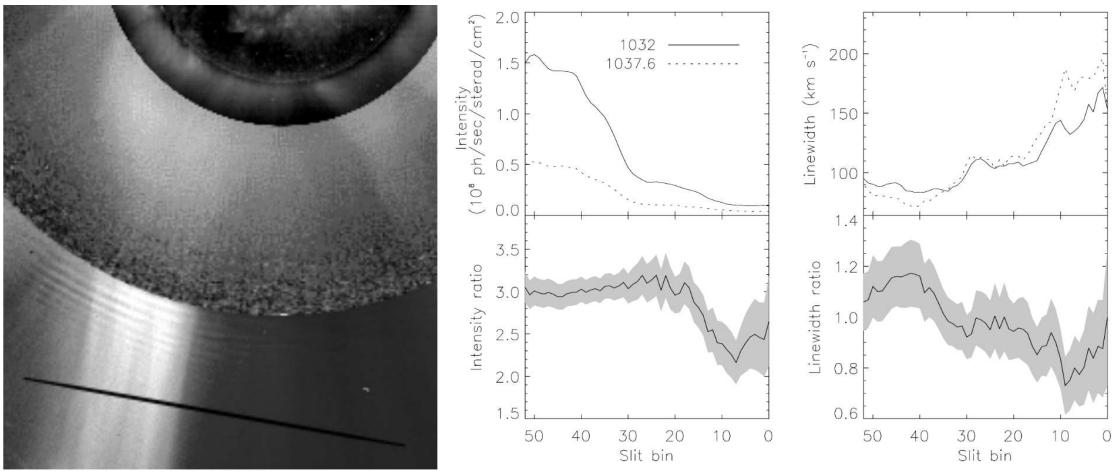

Figure 5.1: Left - nested EIT 284Å Mauna Loa MkIV Coronameter and LASCO/C2 images showing the south corona on 2000/05/07. The black line shows the UVCS field of view. Right - plots showing intensity, linewidth, intensity ratio and linewidth ratio plotted across the UVCS slit. The shaded regions in the ratio plots indicate the uncertainties.

Comparison between the white light image and the spectral data shows the expected increase in intensity at the position of the streamer (slit bin 30-50). Linewidth is at a minimum of ~90 km s^{-1} in the streamer rising to a maximum of ~170 km s^{-1} at slit bins 0-10. Intensity ratio is ~3 in the streamer, decreasing to a minimum of ~2.1 at slit bins 5-10. The linewidth ratio varies from 1.17 ±11% to 0.73 ±16%. It is significantly larger than 1 in the streamer and drops significantly below 1 at slit bins 0-10.

The observation shown here is not an isolated example. A significant difference in the linewidths of the O VI doublet can be found in many UVCS observations. Figure 5.2 shows data from over 100 O VI profiles gathered from 56 UVCS solar maximum observations made at various heights and latitudes during 2000/05/5-16. The data include observations of streamers and the quiet corona. The linewidths show the expected increase with height and the intensity ratio shows an increase between the lowest observations and $\sim 3R_{\odot}$ before decreasing in the highest observations, characteristic of

slower wind. Many of the linewidth ratio values are significantly above or below unity. Linewidth ratio plotted against intensity ratio shows some correlation - lower values of the intensity ratio tend to lower values of the linewidth ratio.

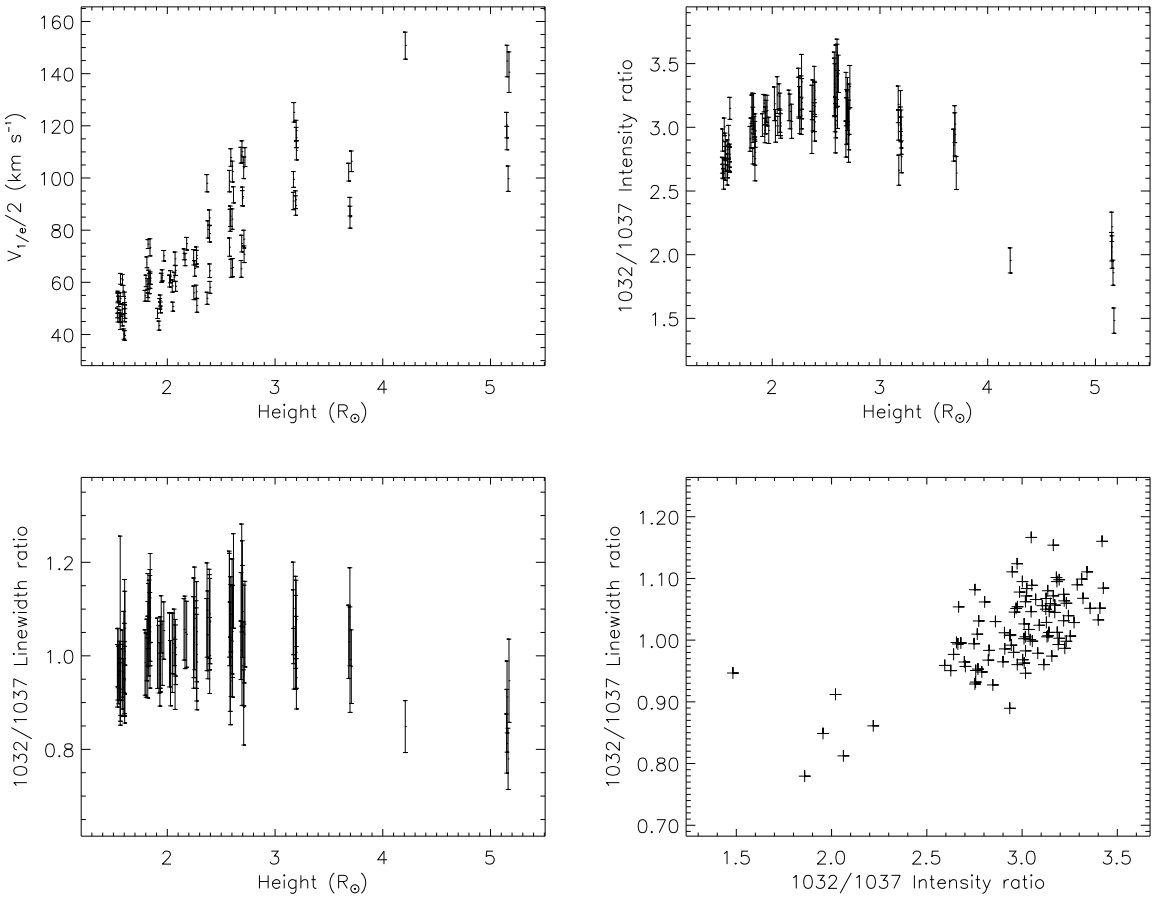

Figure 5.2: Data from over 100 O VI profiles gathered from 56 UVCS observations made at various heights and latitudes during 2000/05/5-16. Plotted against height are O VI 1032 linewidth (*top left*), 1032/1037 intensity ratio (*top right*) and 1032/1037 linewidth ratio (*bottom left*). *Bottom right* - linewidth ratio plotted against intensity ratio.

5.3 The Model

Line emission is modelled along a LOS with a plane of sky (POS) height (referred to sometimes as the impact parameter) of $3R_\odot$. The LOS is extended to a height of $4.8R_\odot$ in both directions, at which point the emission is very small relative to the POS emission. Emission is integrated along the LOS for each wavelength bin. The resulting profiles for the O VI doublet are each fitted with a Gaussian to provide intensity and linewidth. Solar wind parameters can be adjusted along the LOS,

for example velocity can be increased as a function of height to simulate the solar wind acceleration. An example of one set of solar wind conditions is shown in figure 5.3, along with the lines calculated from those conditions.

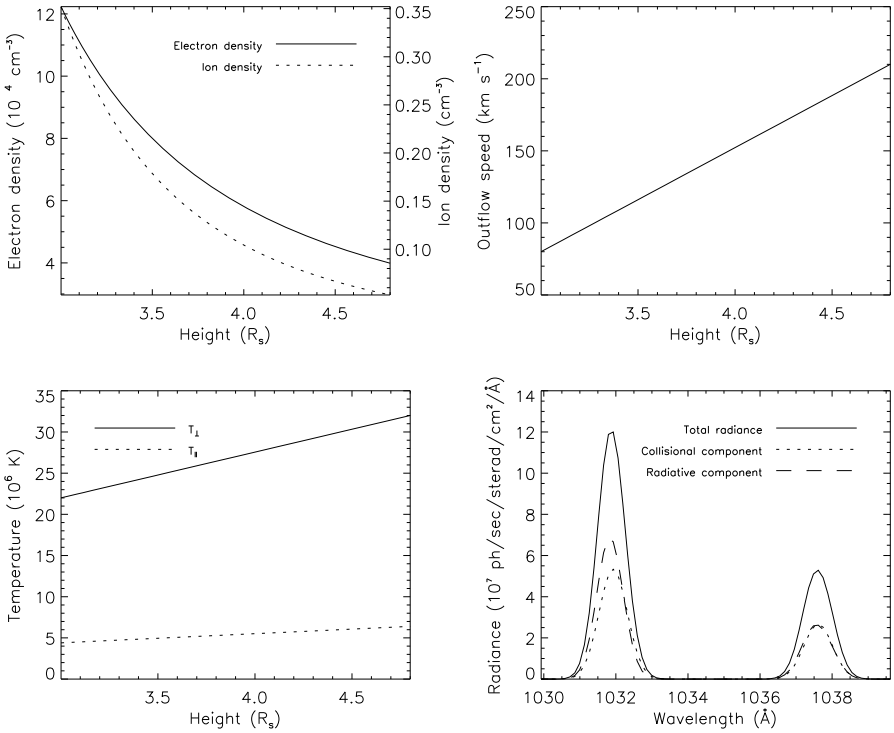

Figure 5.3: A set of solar wind parameters and the resulting spectral lines.

Coronal electron density as a function of height is given by the expression of Guhathakurta & Holzer (1994) multiplied by a factor of 1.7:

$$N_e(r) = 1.7\left[1.4\times10^6(1/r)^{2.8} + 8\times10^7(1/r)^{8.45} + 8.1\times10^7(1/r)^{16.87}\right]$$

where r is the height in solar radii. This expression gives good general agreement with observed electron densities in the quiet corona, that is, regions not associated with streamers or coronal holes. The electron temperature is kept constant at a million degrees K. Ion density is calculated from the electron density at the POS height using the ionization equilibria of Mazzotta et al. (1998) and the oxygen abundances of Feldman et al. (1992), both tabulated in the Chianti atomic database. The ion density profile is extrapolated from the POS along the LOS maintaining a particle flux constant for spherical expansion and the prescribed velocity gradient. The ion temperature distribution is bi-Maxwellian. In this work the perpendicular to radial temperature ($T_\perp$) at the POS is fixed at

$2.2 \times 10^7 K$, in agreement with observed O VI effective temperatures in quiet coronal regions. Three extreme cases of temperature anisotropies will be considered, $T_{\|} = T_e$, $T_{\|} = T_{\perp}$ (isotropic) and $T_{\|} = 2T_{\perp}$

The radiative and collisional components are calculated using the formulations presented in chapter 2. The disk intensities for the O VI and the two C II lines (1037.0 and 1036.3 Å) are those provided by the Solar Ultraviolet Measurements of Emitted Radiation/SOHO (SUMER) solar atlas. These are averaged from SUMER observations of the quiet Sun (Curdt et al., 2001). The Sun is not approximated as a point source and limb brightening is not included in the model disk intensity.

5.4 Results and Discussion

Figure 5.4 shows calculated intensity and linewidth ratios as functions of POS outflow velocity for 3 different velocity gradients along the LOS and for 3 different extremes of temperature anisotropy. The close relationship between the intensity and linewidth ratio can be seen clearly in the top pair of plots, which has an extreme temperature anisotropy of $T_{\|} = T_e$. Such a low $T_{\|}$ makes both spectral lines very sensitive to Doppler dimming and pumping effects. In this case the minima of intensity ratio at outflow speeds of 180 and 380 km s^{-1} correspond to maxima in the linewidth ratio. At these points the 1032 line is ~15-30% wider than the 1037.6 line. This is due simply to the maximum Doppler pumping of the 1037.6 line by the two CII lines at these outflow speeds. Doppler pumping increases the strength of the radiative component and, since this component is narrower than the collisional component, the line is narrowed. The opposite applies to the 1032 line: the collisional component becomes increasingly dominant with increasing outflow velocity since there is no pumping of the radiative component. This is why the second peak in linewidth ratio at 380 km s^{-1} is higher than the first at 180 km s^{-1}. The linewidth ratio minimum at ~280 km s^{-1} corresponds to a local maximum in the intensity ratio, where the 1032 line is more radiatively dominated than the 1037 line.

An anisotropy of $T_{\|} \geq T_{\perp}$ lessens the sensitivity of the linewidth ratio to outflow velocity, as seen in the middle and bottom pairs of the plots in figure 5.4. The linewidth ratio is generally under unity for outflow velocities under ~350 km s^{-1} as the 1037 line is being pumped over a wide range of outflow velocities due to the high $T_{\|}$.

Repeating the calculations for the same parameters but with a radial temperature gradient of

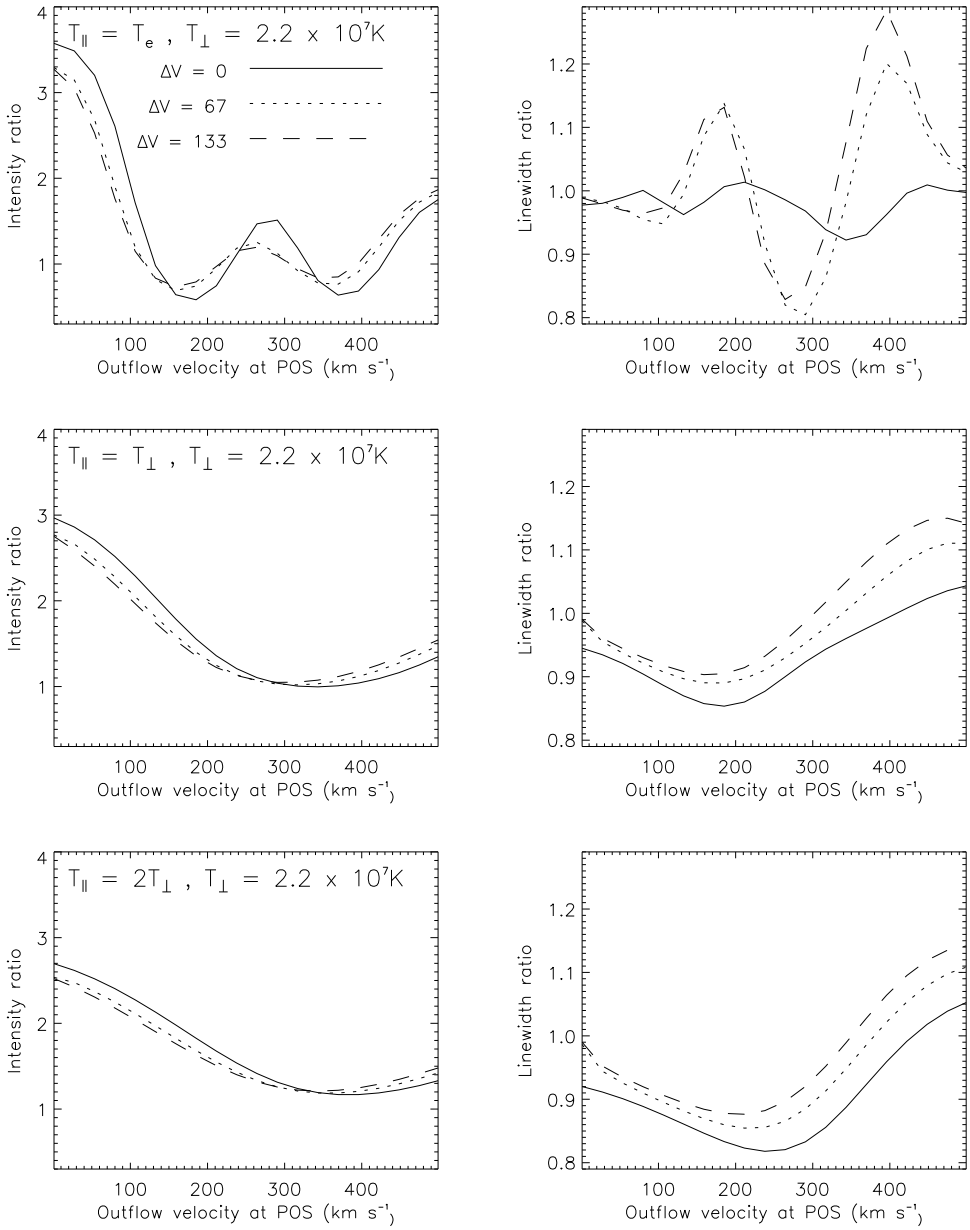

Figure 5.4: Intensity ratio (left column) and linewidth ratio (right column) as functions of POS outflow velocity for 3 different velocity gradients along the LOS and for 3 different extremes of temperature anisotropy. The x-axis is the outflow velocity at the POS height ($3R_\odot$). The different lines in each plot correspond to different radial velocity gradients, as indicated by the ΔV in the legend of the top left plot. The ΔV are in units of km s^{-1} $R_\odot^{-1}$. From top to bottom, the three pairs of plots have temperature anisotropies of $T_\parallel = T_e$, $T_\parallel = T_\perp$ and $T_\parallel = 2T_\perp$

$5 \times 10^6 K R_\odot^{-1}$ leads to very small variations in the linewidth ratio with a maximum difference, when compared to results without a temperature gradient, of under 0.5%. The intensity and linewidth ratios are totally insensitive to any value of ion abundance used at $3R_\odot$ since a term for ion density is in both the collisional and radiative equations. The profile of ion density along the LOS does

have an effect on the balance of collisional and radiative components and therefore on intensity and linewidth ratios. However, multiplying this profile by any constant makes no difference.

The large differences in linewidth which arises from the combination of a radial outflow velocity gradient and a low $T_{\parallel}$ is most easily understood by studying the emission contribution in the LOS and wavelength dimensions simultaneously. Figure 5.5 shows contour plots of O VI 1032 and 1037 collisional and radiative emission contribution for each wavelength and LOS model grid point. These have been calculated for a POS height of $3R_{\odot}$, a radial outflow velocity gradient of 100 km $s^{-1}R_{\odot}^{-1}$, a low $T_{\parallel}$ (1.2×10^6K) and an outflow velocity of 180 km s^{-1} at the POS height.

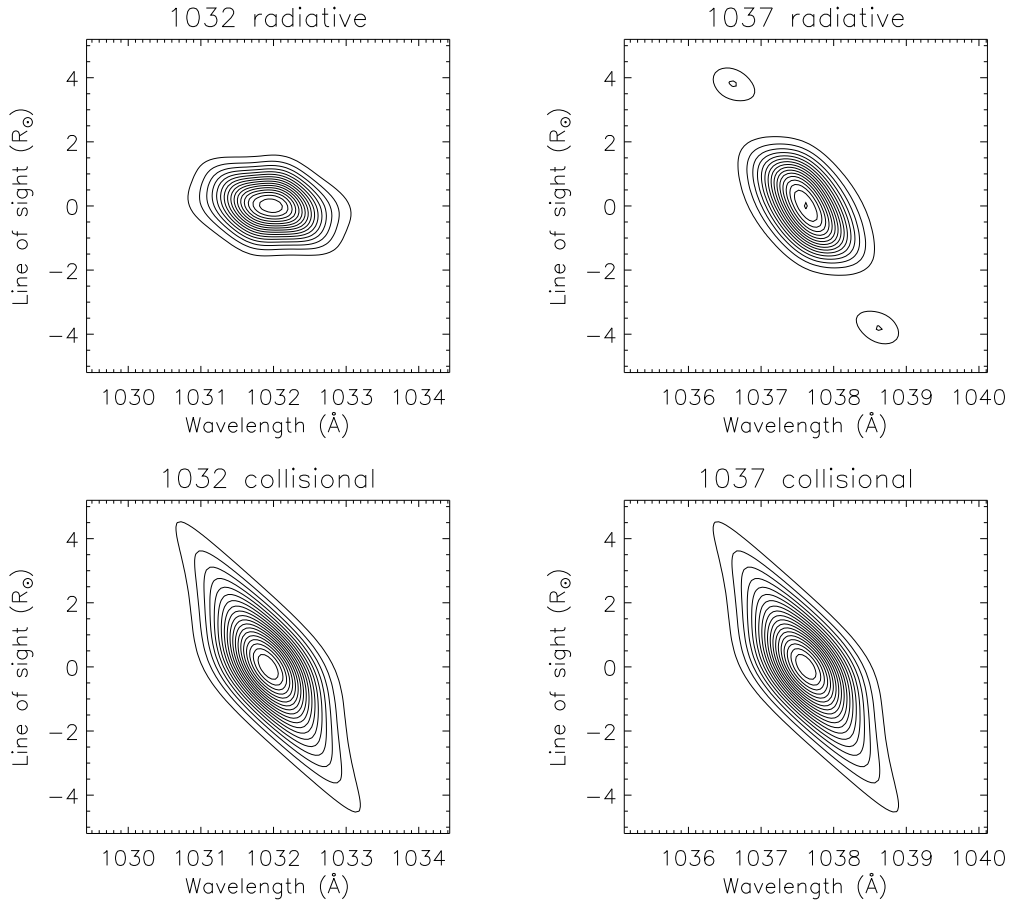

Figure 5.5: Contour plots showing the O VI emission at each wavelength and LOS grid point. The emission is calculated for a POS height of $3R_{\odot}$, a radial outflow velocity gradient of 100 km $s^{-1}R_{\odot}^{-1}$, a low $T_{\parallel}$ (1.2×10^6K) and an outflow velocity of 180 km s^{-1} at the POS height. The *y*-axis shows the distance along the LOS, with zero corresponding to the point closest to the Sun at the POS.

All the emission profiles are limited to a LOS range centered at points nearest to the Sun. This is of course to be expected due to the drop in density. The collisional emissions are proportional to $n_i n_e$ while the radiative components are proportional to n_i. This in itself guarantees a difference in

emission profile between the collisional and radiative components. The 1037 collisional emission is half the intensity of the 1032 collisional emission but their profiles are identical. The collisional components extend further along the LOS than the radiative ones which results in a collisional spectral profile that is wider than the radiative one. The emission profiles of figure 5.5 are skewed due to the finite outflow velocity along the LOS.

The profiles of the radiative emissions show their sensitivity to Doppler dimming and pumping. The 1032 profile is limited to a narrow LOS range due to the radial outflow velocity gradient. As the outflow velocity increases along the LOS, the 1032 radiative component is Doppler dimmed. In contrast, the 1037 line has 2 regions of increased pumping at $\pm 4R_{\odot}$ along the LOS. This leads to a 1037 line profile with small peaks on the Gaussian wings. At outflow velocities which involve Doppler pumping and dimming, the 1037 radiative component is generally wider than the 1032 radiative component.

Figure 5.5 also shows that a LOS must be included in the modelling of the O VI lines to see any appreciable difference between their linewidths. At the POS (zero on the *y*-axis), all the components share a similar wavelength range. Modelling the O VI lines using a POS approximation results therefore in a 1032/1037 linewidth ratio close to unity.

5.5 Implications for the Inversion Method

In the previous chapter, a plane of sky (POS) inversion method used observed electron density, O VI 1032 intensity and linewidth along with the O VI 1032/1037 intensity ratio to provide O VI densities, outflow velocities and temperatures. In particular, the method was applied to a set of UVCS observations of a solar maximum streamer made during 2000/01/28-29 and mass flux was used to suggest a 3-5% sunspot contribution to the incident disk radiation and an isotropic O VI temperature distribution. The inversion technique resulted in modelled 1032 profiles with linewidth virtually identical to the observed values. However, the observed and modelled linewidth of the 1037 line was ignored at all stages of the inversion.

The left plot of figure 5.6 shows the observed linewidths of the 1032 and 1037 lines for the 2000/01/28-29 observations, along with the modelled 1037 linewidths resulting from the POS inversion. It is clear that the observed 1037 linewidths are significantly different from the observed 1032 linewidths at most heights, but the modelled 1037 linewidths closely match the observed 1032

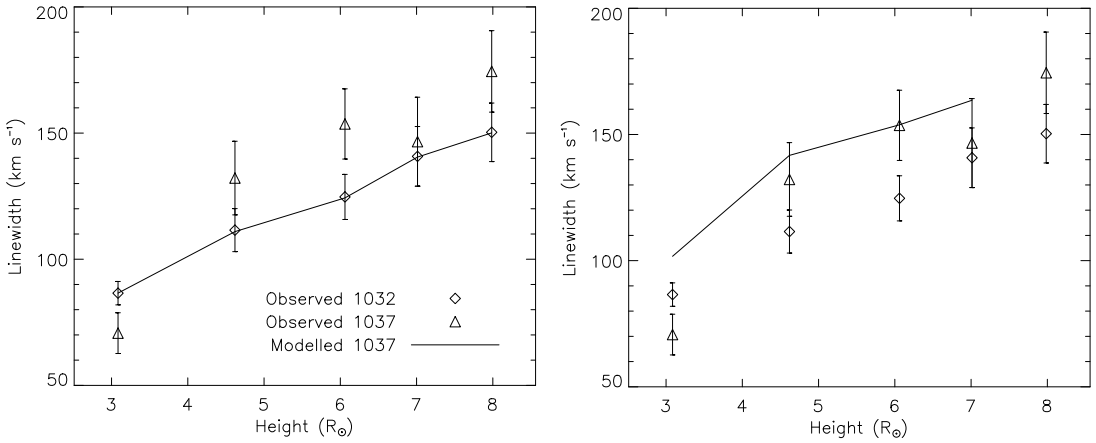

Figure 5.6: *Left* - observed 1032 and 1037 linewidths for the 2000/01/28-29 observations and the modelled 1037 linewidths resulting from the inversion technique introduced in chapter 4 using a POS approximation. *Right* - the same but with the 1037 linewidths resulting from a spherically symmetric model.

linewidths rather than the observed 1037 linewidths. This highlights a failing in the POS inversion.

The right plot of figure 5.6 shows the same set of observed linewidths, with the modelled 1037 line calculated using a spherically symmetric LOS based on the ion parameters found using the POS approximation. That is, the O VI densities, outflow velocities and temperatures calculated from the POS inversion, at all observed heights, are used to create a linearly-interpolated spherical symmetric model of the corona from which extended line of sights are chosen to create O VI profiles. Note that the 1037 linewidth cannot be modelled for the highest observation since we cannot create a LOS at this height constrained by observations at larger heights. Introducing a spherically symmetric LOS causes the modelled 1037 linewidth to deviate considerably from the modelled 1032 linewidths and an improved fit is seen between the modelled and observed 1037 linewidths at heights of 4.6 and $6.1 R_{\odot}$.

An improvement in fit between observed and modelled line profiles is made simply by introducing a spherically symmetric LOS. An iterative algorithm is envisaged which makes a spherically symmetric inversion of UVCS observations as follows:

1. Calculate initial O VI parameters using a POS inversion at heights $h_1, h_2, ..., h_n$.
2. Create initial spherically symmetric coronal model from the ion parameters.
3. Set $i = 0$.
4. $i = i + 1$. Current height is $h_{(n-i)}$.

5. Calculate new O VI profiles by taking an extended LOS through the spherically symmetric model at current height.

6. Compare modelled profiles with the observed. If a good fit is found go to 4 (or until all heights are finished). If fit is unsatisfactory then go to 7.

7. Adjust ion parameters at current height, $h_{(n-i)}$, keeping the values fixed at $h_{(n-i+1)}$. Interpolate for heights along the LOS between $h_{(n-i)}$ and $h_{(n-i+1)}$ maintaining spherical symmetry. Go to 5.

This algorithm should lead to a spherically symmetric model of ion parameters yielding O VI profiles which match observed profiles at all heights except for the highest observed height. The modelled 1037 linewidths shown in the right plot of figure 5.6 are created, in essence, from the first iteration of the algorithm. It is a computationally demanding scheme compared to the POS inversion due to the extended LOS. It is impractical to attempt the calculations on a standard desktop computer and future work will concentrate on implementing the algorithm on a more powerful machine.

It is anticipated that the observed 1032/1037 linewidth ratio will in some cases provide an additional constraint on the spherically symmetric inversion and will lead to improved estimates of assumed parameters, most notably the temperature anisotropy. For example, a spherically symmetric inversion of O VI profiles observed by UVCS at heights of 3 and $4R_{\odot}$ could constrain outflow velocity, $T_{\perp}$, outflow velocity radial gradient and the $T_{\perp}$ radial gradient for the $3R_{\odot}$ observation. A comparison of the modelled and observed linewidth ratio could then give a constraint on $T_{\parallel}$, and the calculations repeated for an improved estimate of $T_{\parallel}$. This process could be repeated until the modelled and observed linewidth ratio agreed closely.

5.6 Conclusions

A study of O VI profiles calculated from a finite LOS in a spherically symmetric model of the corona leads to a simple explanation for the difference in linewidths so often seen in observations. The differences in observed linewidths are primarily due to the varying balance of collisional and radiative components in each line, a balance which depends on Doppler dimming and pumping. Any difference in width between the 1032 and 1037 radiative profiles caused by outflow velocity gradients are secondary effects. Temperature gradients or inhomogeneities are also secondary in

importance. The linewidth ratio will in many cases serve as an additional constraint on the semi-empirical modelling of UVCS observations, particularly in inversions which include a finite LOS.

Chapter 6

Hydrogen Ly-α Intensity Oscillations Observed by UVCS/SOHO

This chapter was published as an article in the Astrophysical Journal in April 2004 (see Morgan et al. (2004)). A new approach to UVCS spectroscopic data is taken here - a detailed time analysis of UVCS observations of Ly-α intensity. Its contents therefore are quite different from other the chapters. However, the detection of density waves at heights observed by UVCS and the calculation of O VI densities, outflow and temperatures are diverse subjects which share a common goal. This goal is to provide observational impetus for models of coronal energy deposition.

6.1 Introduction

The study of oscillations in ion intensity in the chromosphere and off-limb atmosphere is a well-established field and there exists a large body of literature on results from instruments such as TRACE (Rutten & Krijger, 2003; McIntosh et al., 2003; Muglach, 2003), SUMER/SOHO (Wang et al., 2003) and CDS/SOHO (Marsh et al., 2003; Banerjee et al., 2001), to list but a few recent studies. The high intensities of emission lines close to the Sun enable these instruments to acquire data at a high temporal resolution with a reasonable signal to noise ratio. Observations by UVCS/SOHO starting at 1.5 $R_{\odot}$ are less well suited for temporal analysis and the problems posed by a low signal to noise ratio, particularly at larger heliocentric distances in non-streamer regions, are considerable. Temporal studies of UVCS emission line observations at the highest observational frequencies are

therefore rare, although detailed studies of oscillations in polarized brightness from the UVCS white light channel have been made (Ofman et al., 1997, 2000).

Standard spectroscopic analysis of UVCS data involves integrating photon counts over many exposures. Combining many short exposures lessens Poisson uncertainties in photon counts and produces spectral profiles that easily accommodate fitting to Gaussian functions. In this chapter no attempt is made to use this standard approach to the data. Preservation of signal at the highest spatial and temporal resolution forces the use of raw photon counts with the minimum of pre-processing. Wavelet analysis is applied to the data and an appropriate test employed which reveals the presence of significant oscillations. The method is applied to a set of UVCS observations of Hydrogen Ly-α taken in June 2002 at a range of heights above the south polar region and southeast mid-latitude streamers. A description of the observations is given in section 6.2, the analysis techniques are explained in section 6.3, results are presented in section 5.4, followed by a discussion in section 6.5 and concluding remarks in section 6.6.

6.2 Observations

Spectroscopic observations of the Hydrogen Ly-α line were obtained using the redundant Ly-α channel on the UVCS Oxygen VI detector on June 20 to 21, 2002. From 23:00 on June 20 until 06:00 on June 21 the position angle of the UVCS slit center was 150° counter-clockwise from north. Data were collected sequentially at heights of 2.0, 2.2, 1.8 and 1.5$R_\odot$, during the seven hours of observations. Table 6.1 gives the start and end times and number of exposures for each height observed. For these observations, there are 60 spatial bins along the UVCS slit, giving a minimum spatial resolution of 42 arcsec. Each observation has an average time of 130s between exposures.

Table 6.1: Details of UVCS observations 2002/06/20-21. Ht and PA are the heights and position angles of the FOV closest to the Sun. Tot exp is the total integrated exposure time. Spat and spect are the spatial and spectral binning respectively. Heights are in $R_\odot$, spatial binning in arcseconds, spectral binning in Å and slit widths in Å.

Start date/time	End date/time	Ht	PA	Tot exp	Spat	Spect	Slit width
20-JUN-2002 23:00	21-JUN-2002 01:01	2.0	150	1h 48m	42	0.099	0.3
21-JUN-2002 01:02	21-JUN-2002 03:21	2.2	150	2h 7m	42	0.099	0.3
21-JUN-2002 03:21	21-JUN-2002 04:48	1.8	150	1h 20m	42	0.099	0.3
21-JUN-2002 04:49	21-JUN-2002 05:58	1.5	150	1h 4m	42	0.099	0.3

Figure 6.1a shows a UVCS/LASCO C2 and UVCS/EIT composite image of the southeastern corona from June 21, with lines drawn to indicate the different slit positions. The slit extends from above the south pole to cross the mid-latitude streamers at ~150°. Note that the streamers are partially obscured near 135° in the figure due to the mount of the LASCO occulting disk. Low resolution Kitt Peak coronal hole maps indicate the presence of a coronal hole over the south pole during the time of the observations. Although June 2002 was a time of considerable activity in the solar corona the data in this paper were not affected by CME activity. The mid-latitude streamers remained stable throughout the seven hours of observations, with some slow movement due to solar rotation.

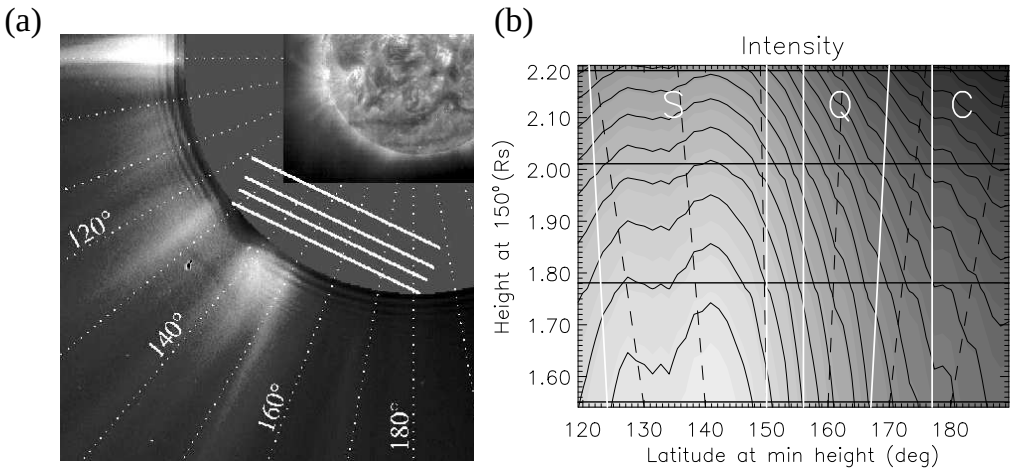

Figure 6.1: (a) Composite LASCO C2 and EIT image from June 21. White lines indicate positions of the UVCS slit. Dotted white lines indicate position angle. (b) Ly-α intensity interpolated into a contour plot of the observed region. Streamer, quiet sun and coronal hole regions are labeled S, Q and C and are bounded by the white lines. The dotted lines are lines of constant position angles. Higher intensities have lighter shading. The intensity contours start at $\log_{10}$ 11.3 photons s^{-1} Ω^{-1} cm^{-2} $Å^{-1}$ at the lowest height and decrease by $\log_{10}$ 0.065 photons s^{-1} Ω^{-1} cm^{-2} $Å^{-1}$.

Intensity is obtained at all 4 slit heights from the time integrated Ly-α profiles. Figure 6.1b is constructed from interpolating between the log of intensity at all heights observed. Fitting errors are avoided and signal to noise ratio is greatly improved by employing a sliding window of 5 slit pixels. Cubic convolution is used to interpolate for the heights between the slits. The observed heights are shown by the horizontal unbroken dark lines in figure 6.1b while lines of constant latitude are shown by the dashed dark lines. The vertical axis denotes the heliocentric height at a latitude of 150° and the horizontal axis denotes the latitude for the 1.5 $R_\odot$ observation. It is not an easy or exact matter to identify structures in the corona from UVCS data due to the sharp intrinsic drop of

intensity with height. However, from the LASCO C2 image in figure 6.1a, the daily LASCO C2 movie, the Kitt peak coronal hole map and figure 6.1b, three distinct regions covered by the UVCS FOV have been identified and labeled. The streamer is most easily identified as the region of high intensity, labeled S and bounded by white lines in figure 6.1b. We can see two intensity peaks in the streamer, one lying approximately radially at ~143° and the other varying in latitude from 128-134° with increasing height. The coronal hole, labeled C, is identified by the drop in intensity which varies in latitude from just under 180° at 1.5$R_\odot$ to 172° at 2.2 $R_\odot$. An area between the streamer and coronal hole, labeled Q, is identified with the quiet sun, with intensity smoothly decreasing with increasing latitude.

6.3 Data Analysis

The nature of the search for significant oscillations in UVCS data allows many standard techniques usually associated with the instrument to be disregarded. Since relative temporal fluctuations of intensity are of interest here instrumental influences on line profile and intensity that remain constant in time such as slit profile deconvolution and detector flat field correction are ignored. No estimated correction for stray light or light from interplanetary hydrogen is made, under the assumption that these unwanted contributions change only slowly.

The Ly-α 1216Å line is identified in the appropriate UVCS detector mask and the photon counts are integrated over the wavelength range of the line. Since the position and width of the Ly-α line on the detector can vary due to physical and instrumental causes, the appropriate wavelength range is estimated separately for each pixel along the slit. The range is estimated from the mean wavelength and linewidth of the time integrated line profile for that pixel. The few unreliable spatial pixels at the extremities of the UVCS slit are discarded.

After integrating over the line profile, a time series of Ly-α photon counts for each UVCS pixel along the slit is obtained. The exposure time for these observations is a constant 120s. There is however a pause of approximately 10s between each exposure, a pause which can vary by a second or two throughout an observation. The cadence is therefore ~130s, with data being collected for only 120s of each 130s time step. Since the pauses between exposures are small compared to the cadence (< 10%), a count rate during the pause equal to the count rate of the preceding exposure is assumed. Since the variance in pause time between exposures is very small compared to the total

exposure time (< 1%) no attempt is made to interpolate to a constant time step - the average time step (~130s) is used as a constant for the whole observation. The uncertainties in photon counts arising from the gaps in observation are unavoidable but acceptable. The uncertainties due to the varying time steps are negligible.

Intensity time series are transformed into time-frequency space using the widely used discrete Morlet transform provided by Torrence & Compo (1998). Taking the modulus squared of the transform a power spectrum is obtained for each pixel. Figure 6.2 shows an example of a power spectrum of a dummy observation consisting of a superposition of two sine waves of equal amplitude and periods 12 and 34 minutes and Gaussian noise with standard deviation one and a half that of the sinusoidal signals. The wavelet power spectrum identifies bands of higher power at these periods throughout the time series. The white contours surround areas of the spectrum with coefficients below the 5% significance level in comparison with a background noise level described below. The 12 minute signal is often indistinguishable from the background noise although the 34 minute signal is clearly identified through most of the time series. The thick dashed line in the wavelet spectrum is the cone of influence which indicates where the spectrum may be influenced by edge effects. Features below this line (at longer periods) should be interpreted with care. The global power spectrum shown in figure 6.2 is the time averaged wavelet power spectrum. The global spectrum is similar to the result one would obtain from a smoothed Fourier transform. The peaks at 12 and 34 minutes are seen clearly in the global spectrum.

Coefficients of wavelet power can be compared with the power expected from a background of Gaussian noise, and an appropriate confidence level established as a test of significance. This is, in general, the standard significance test used in wavelet analysis of geophysical data and a full description is given in Torrence & Compo (1998). Since the test is performed directly in the time-frequency space of the wavelet power spectrum it is useful for identifying sporadic or non-stationary signals. The significance test assumes a Gaussian distribution of background noise while it would be expected that both Poisson statistical and Gaussian instrumental noise would dominate UVCS data. However, the Gaussian model is valid for the observations of Ly-α at the low coronal heights in this study since the photon counts are high enough to ensure that the Poisson noise distributions are very similar to Gaussian distributions.

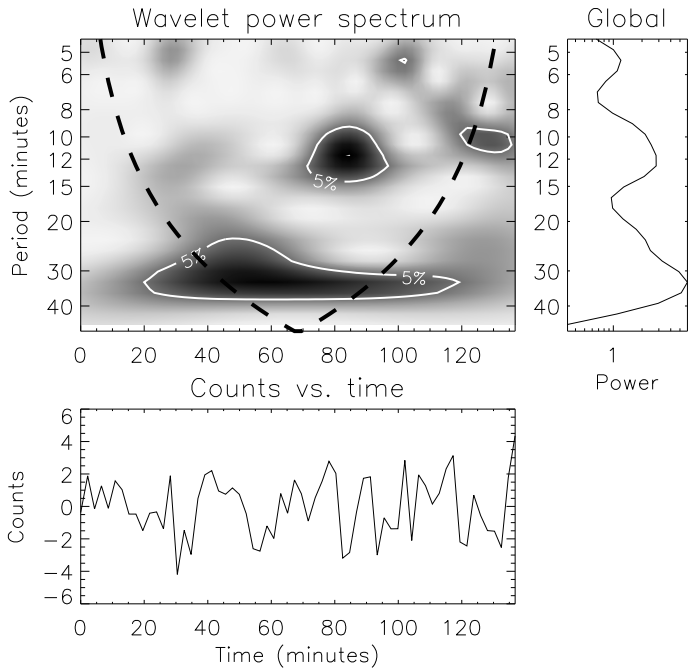

Figure 6.2: Example of wavelet and global power spectrum for a contrived time series of 2 sine waves and Gaussian noise.

6.4 Results

6.4.1 Significant Oscillations

Figure 6.3 contains intensity time series, wavelet power spectra and global power spectra from the streamer, quiet sun and coronal hole regions of the UVCS slit. Figure 6.3a is from a latitude of 137° and a height of $1.85R_{\odot}$, near the local trough in intensity between the two streamer peaks (see figure 1(b)). The periodic oscillation in intensity is clearly seen in the time series starting at ~30 minutes into the observation time and continuing for at least 50 minutes. The wavelet power spectrum confirms the significance of this oscillation and the global spectrum shows the high power at a period of 14 minutes. Figure 6.3b comes from the quiet sun region at a latitude of 154° and a height of $2.0R_{\odot}$. A significant 20 minute oscillation starts 10 minutes into the observation and continues for 50 minutes. The period of oscillation then lengthens to 28 minutes and continues for 40 minutes. Figure 6.3c is from the coronal hole region at latitude 182° and height $1.77R_{\odot}$. The strongest feature is the 13 minute oscillation continuing from 30 to 60 minutes. There is another oscillation of significance at the shorter period of 6-7 minutes at the start of the observation.

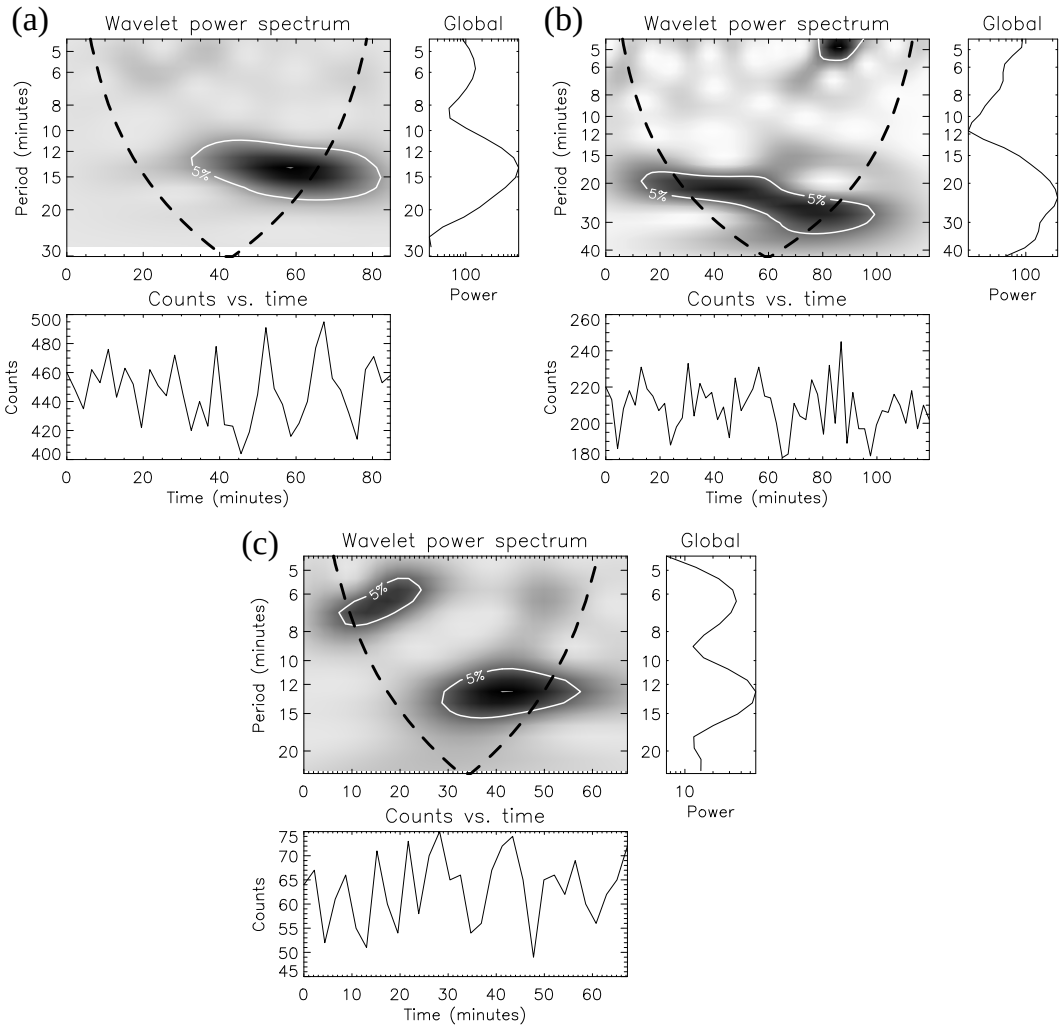

Figure 6.3: Time series and power spectra at (a) height 1.54$R_\odot$, latitude 137° (streamer), (b) height 2.0$R_\odot$, latitude 154° (quiet sun), (c) height 1.77$R_\odot$ latitude 182° (coronal hole).

6.4.2 Similar Spectra at Neighboring Heights

It is interesting to find strong correlations between global spectra at similar latitudes but different heights. Reasonable correlations may be found provided that the coronal structures across the slit remain relatively stable. This is the case for the observations in this study. Figure 6.4 shows two sets of examples. Figure 6.4a consists of four global spectra from the four different observed heights, all from pixels at latitudes 136-137°, which, from figure 6.1b, can be seen near the trough in intensity between the two streamer peaks. The power for each plot is scaled between 0 and 1 to enable comparison between the spectra. Correlations between consecutive observations are: 0.39 (2.0-2.2$R_\odot$), 0.82 (2.2-1.8$R_\odot$) and 0.62 (1.8-1.5$R_\odot$). The set in figure 6.4b comes from a latitude of 150° near the edge of the streamer. Here again there are four global spectra from the four different

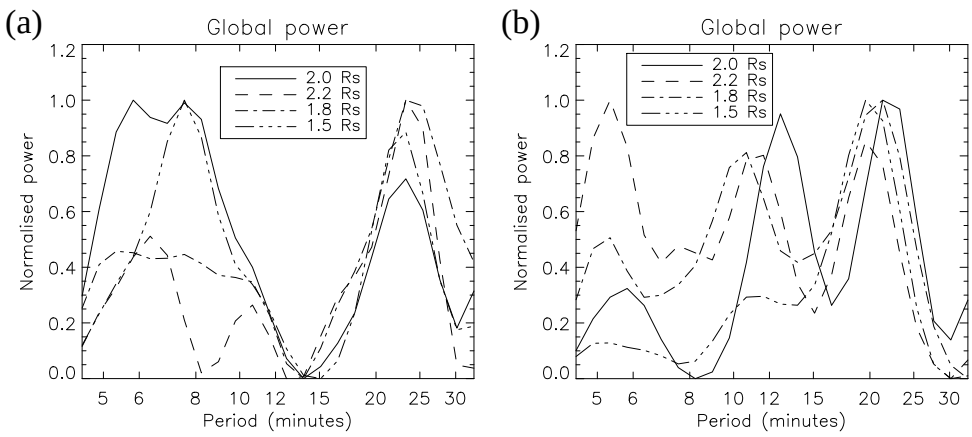

Figure 6.4: Normalized global spectra from all observations from pixels at latitudes (a) 136-137° and (b) 150°. Heights of slit center are given in the legend.

heights. Correlations between consecutive observations are: 0.23 (2.0-2.2$R_\odot$), 0.64 (2.2-1.8$R_\odot$) and 0.82 (1.8-1.5$R_\odot$).

6.4.3 Similar Spectra Across the Slit

Pixels along the slit often possess global power spectra that share no similar features with their neighboring pixels. This is not surprising considering both the coarse 42 arcsec spatial binning of the data and the generally low signal to noise ratio. However, it is reassuring to find peaks in power spectra that remain fairly constant across a region covered by several pixels, or peaks that increase or decrease slowly in period across many pixels. To display such regions, we place the global spectra of pixels side by side in contour plots. Figure 6.5a shows a contour plot of global spectra from the whole UVCS slit from the 2.0$R_\odot$ observation. Figure 6.5b shows the region from 161° to 181° in greater detail. The streamer, quiet sun and coronal hole regions are marked S, Q and C and are bound by vertical lines. The intensity of each time series must be normalized in order to compare power at low and high intensity structures without bias. This is done by subtracting the mean and dividing by the standard deviation in the time series of each pixel prior to the wavelet transform. After the transform, an unsophisticated and simple filter is applied where wavelet coefficients with significance <2% in comparison with a Gaussian noise model are left unchanged while the coefficients with significance >2% are set to zero. This removes noise and weak features that would complicate the display of the power spectra across the slit. The final time averaged global spectra are obtained from the filtered wavelet power spectra. Figure 6.5b is subjected to less filtering than

that used on the main contour plot, with a significance threshold of 8%.

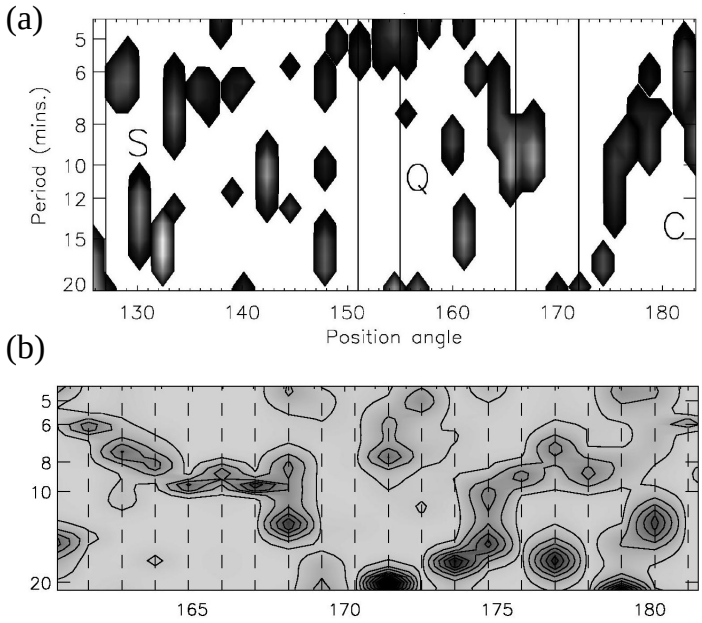

Figure 6.5: Filtered global spectra from slit pixels from the $2.0R_{\odot}$ observation arranged in a contour plot. (a) Global spectra across the whole slit. (b) Global spectra from the region between 161° and 181°, with a lower filter threshold than that used for (a).

As seen in figure 6.5a, many pixels in the streamer have peaks in periodicity between 5-8 minutes, in particular, a group of 8 neighboring pixels situated between 132° and 141° all share peaks at 6-7 minutes. There are 9 neighboring pixels between 149° and 158° with peaks at 5 minutes or less. Around 166°, a group of 5 pixels have peaks of 9 minutes. The region from 165° to 177° is bereft of peaks at periods less than 7 minutes, while small groups of 2-3 pixels share a periodicity of 7-10 minutes in the coronal hole region. The sharing of periodicity across many slit pixels is seen more clearly in figure 5(b) which shows a contour plot of global spectra from 20 neighboring pixels situated between latitudes 161° and 181°, a region that contains the drop in intensity between the quiet sun and coronal hole. The position of the center of each slit pixel is indicated by the dashed vertical lines. The most consistent feature is the band of power extending between latitudes 161° to 168°, period 6 to 10 minutes. Between 161° and 164° the period increases across 4 pixels from 6 minutes to under 10 minutes. From 164° to 168° the periodicity stays between ~9 and 10 minutes over 4 pixels, with a broadening in period at 168°. There is another interesting band of power with decreasing period from 11 to 6 minutes between latitudes 174° to 181°. Isolated clusters of power at short periods ~5 minutes and longer periods ~20 minutes lie between 169° and 180°.

6.5 Discussion

Use of the highest temporal and spatial resolution of UVCS data guarantees a low signal to noise ratio. Before discussing results we must address instrumental effects and their possible contribution toward detected periodic oscillations. Grating jitter is a high frequency oscillation of the grating mechanism, and would hardly affect our results since it has a far shorter period than the exposure time of two minutes (L. Gardner, private communication). Drift is a shifting of the line on the UVCS detector due to either heating/cooling of the instrument or a settling of the grating immediately after it is moved. It is a slow variation, present at a scale of tens of minutes to hours. It may well operate within the lower frequencies shown in our results. Drift causes a shifting of the line position on the detector which would in turn cause a shifting in intensity since different regions of the detector have different gain responses (Kohl et al., 1995). However, an oscillating movement of any part of the UVCS instrument would be likely to induce an oscillation in line position and intensity across the whole UVCS slit, with similar frequency at every pixel. However, this is not seen in this dataset. Indeed, strong oscillations in individual pixels are often not replicated in their neighboring pixels.

It is clear from the wavelet analysis that oscillations of Ly-α intensity are sporadic in our observations. Oscillations remaining coherent for longer than 3 wavelengths are rare. This may be a real property of oscillations at this height or may be due to observational limitations, as we may be detecting only short glimpses of longer duration oscillations whose signals are often lost due to turbulence and other wave motions along the line of sight. A study of a far larger set of data may resolve this issue. Since the oscillations are sporadic, it is useful to create for each observation a histogram summing the durations of significant oscillations found at each period. Figure 6.6 contains histograms for each observation presented in this paper, with total durations converted to units of wave counts. The dotted lines in figure 6.6 are the mean expectation values for Gaussian noise and the dashed lines are the 5% significance levels. These were obtained from two thousand repetitions of the method using dummy observations consisting of Gaussian noise. Note that significant oscillations with duration shorter than one wavelength are not counted. Figure 6.6a is the histogram for the observation with slit center at $1.5R_{\odot}$. The strongest periodicity is at 8 minutes, with other significant bands at 13 and 16 minutes. Figure 6.6b, from $1.8R_{\odot}$ also has a strong periodicity at 8 minutes and another band at 5 minutes. Figure 6(c), from $2.0R_{\odot}$ has only one significant peak at 21 minutes. Figure 6.6d from $2.2R_{\odot}$ has significant peaks at just under 8 minutes and just over 10

minutes. The observations all show significant bands of preferred periodicity. It is interesting that a band of preferred periodicity of ~8 minutes emerges from 3 out of the 4 observations.

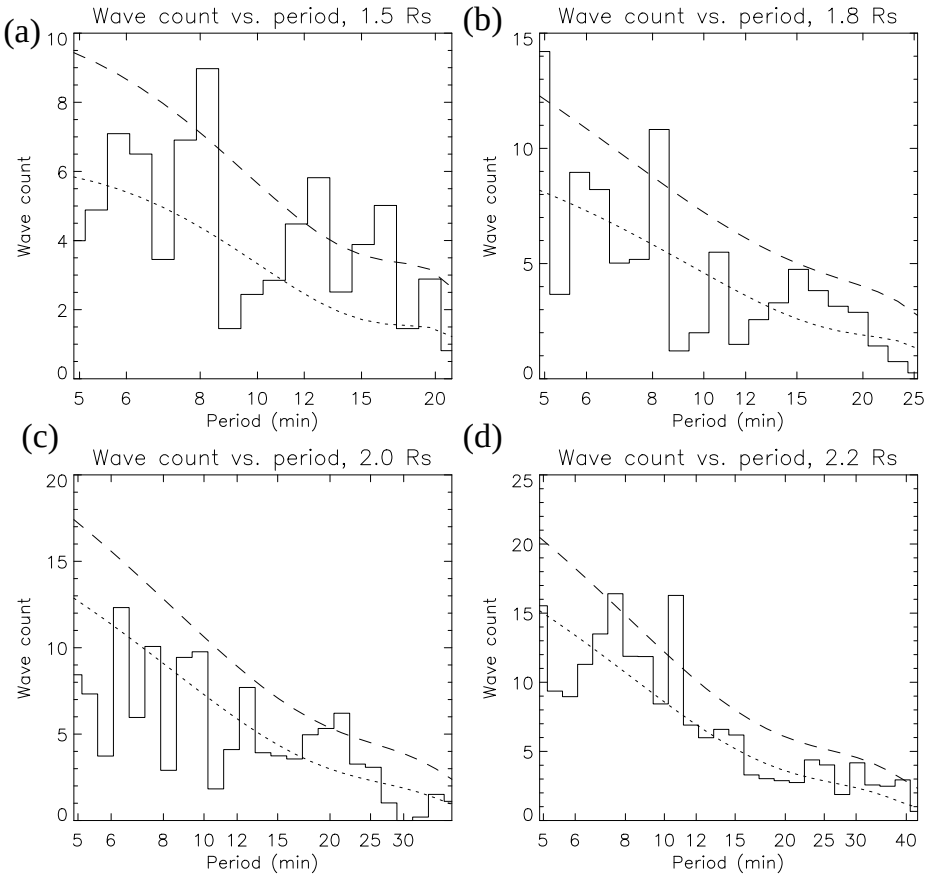

Figure 6.6: Histograms of significant oscillations for the four observations. The dotted line is the mean value and the dashed line is the 5% significance level for Gaussian noise.

Figure 6.7 investigates the spatial origin of the ~8 and ~10 minute bands of periodicity from the $2.2R_{\odot}$ observation by plotting wave counts against latitude. Figure 6.7a shows the distribution of all ~8 minute waves detected along the slit. The streamer, quiet sun and coronal hole are labeled S, Q and C. Figure 6.7b shows the distribution of ~10 minute waves detected along the slit. Both figures show that the contribution to preferred bands of periodicity come from a minority of pixels - that the detected oscillations are sporadic in space as well as in time. Both plots in figure 6.7 show their highest density of wave counts around a latitude of 162° in the quiet sun region. Both also have a smaller peak at 142° which is close to the peak intensity of the streamers. Figure 6.7b shows strong ~10 minute oscillations from two neighboring pixels at 172° in the coronal hole region.

EIT/SOHO observations of polar plumes indicate oscillations with periods of 10-15 minutes (DeForest & Gurman, 1998). Chromospheric and low corona temporal studies of CDS/SOHO

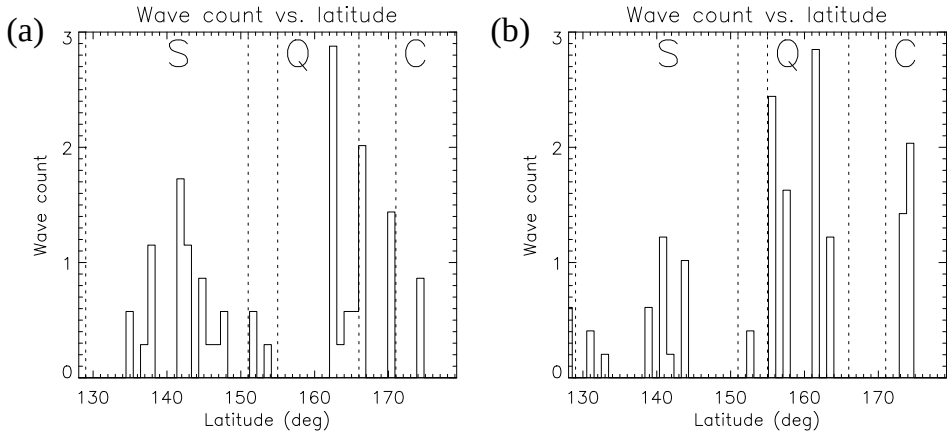

Figure 6.7: Distribution of significant oscillations across the UVCS slit for periodicity of (a) ~8 minutes and (b) ~10 minutes.

data have detected possible significant oscillations with periods of 20-50 minutes increasing to 70 minutes at a height of 25 arcsec off-limb (approximately $1.02R_{\odot}$) in a polar coronal hole plume and inter-plume regions (Banerjee et al., 2001). Both studies interpret the oscillations as the signatures of outward propagating slow magneto-acoustic waves. The total observation times at any one position of the UVCS data presented here are too short to discern whether there are significant oscillations at periods of ~45 minutes or greater. In coronal holes at heights close to those of our study ($1.9R_{\odot}$), Ofman et al. (2000) found quasi-periodic variations in polarized brightness observed by the UVCS white light channel, with significant power spectra peaks at periods around 6-10 minutes. The polarized brightness is directly related to the electron density along the line of sight, and the oscillations were interpreted as evidence of compressional waves propagating outward from the Sun. Produced by resonance scattering of the chromospheric Ly-α emission by neutral hydrogen in the corona, the Ly-α intensity is also proportional to the electron density; hence its behavior should follow that of the polarized brightness. Evidence for a 7-8 minute oscillation in the Ly-α line lends support to the periodicity found in the polarized brightness measurements.

Given that the periodicity derived from the observations are associated with density fluctuations they can be a signature of fast or slow magnetosonic waves. That the periodicity persists at least out to $2.2R_{\odot}$ implies that these waves are not damped very quickly in the corona as some theoretical studies suggest (Hollweg, 1978). Furthermore, that the 7-8 minute oscillations are present in all three regions: coronal hole, quiet Sun and streamer, and are present in 3 out of the 4 observations at different heights, points to the universality of the wave modes propagating in the solar corona,

independently of the large scale magnetic field. They also suggest that pure Alfvén waves, which have never been observed in the corona, are not the only waves present there.

6.6 Conclusions

Application of the wavelet analysis technique to Ly-α UVCS observations shows that oscillations with significant power exist in the line intensity. Furthermore, significant correlations are found between oscillation patterns at neighboring pixels along the slit of the detector. For some observations at similar latitudes, global spectra profiles are preserved as a function of radial distance. Cataloging oscillations of significant power according to periodicity, and weighted by their duration, a preference toward 7-8 minute oscillations in 3 out of the 4 observations is found. Other preferred bands of periodicity are present at the different observations.

The dataset presented here is too small to derive further conclusions regarding the physical cause of the oscillations. Future work will present a statistical study of power spectra profile from a far larger set of observations. These should provide a reliable basis for a more thorough discussion regarding the underlying physical processes responsible for the observed oscillations.

Chapter 7

The Future of UVCS - a Radial Line of Sight

7.1 Introduction

In the next few decades of solar system exploration it is likely that spacecraft missions will venture far closer to the Sun than has been previously attempted. The Solar Probe mission (see *http://solarprobe.gsfc.nasa.gov*), with a planned launch date during 2012, will attempt two solar passes at different times in the solar cycle, flying to heights as low as $4R_{\odot}$. Figure 7.1 shows the planned trajectory of Solar Probe. This will give, at last, invaluable *in situ* measurements of the inner corona. This chapter models and discusses the expected spectral profiles from a UV spectrometer aboard such a spacecraft. This analysis is essential in the proposition and planning of such an instrument.

The current SOHO spacecraft orbits the L1 Lagrangian point between the Earth and the Sun. UVCS aboard SOHO views the 90° scattering of UV coronal emission due to the large distance between SOHO and the Sun. An UV spectrometer placed in the inner corona can take a radial line of sight (LOS) from an unprecedented vantage point. This LOS would necessarily point away from the Sun due to the high intensity of the disk emission. This chapter shows that a radial LOS gives improved outflow velocity and $T_{\parallel}$ diagnostics over those given by 90° scattering.

Section 7.2 presents the geometry and analytical equations suitable for calculating O VI emission along a radial LOS. Section 7.3 describes the parameters obtained from a global two-dimensional

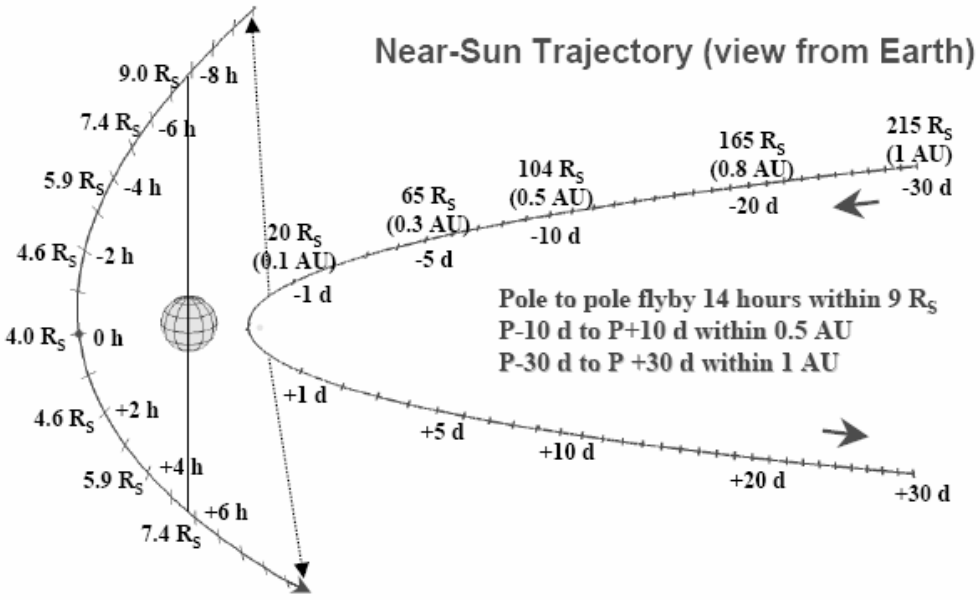

Figure 7.1: The planned trajectory of Solar Probe, from McComas (2004)

magnetohydrodynamic (MHD) three fluid model for both coronal hole and streamer solar wind regions, and gives O VI line profiles computed along a radial LOS using the model parameters. A discussion of the results and conclusions are given in section 7.4.

7.2 A Radial Line of Sight

The geometry and resulting radiative and collisional equations for a radial LOS are far simpler than those for 90° scattering. The radial LOS geometry is shown in figure 7.2. The observer is at point I, looking away from the Sun along the radial *x*-axis. Point P is an emitting point along the *x*-axis. The origin is the Sun center, O, and E is a point on the Sun's disk. θ is the angle OPE, the angle between the radial and the direction of the incident radiation.

7.2.1 Collisional Component

For collisional emission, we need only consider the velocity distribution of emitters along the radial *x*-axis:

$$f(v_x) = \left(\frac{1}{\pi\alpha_x}\right)^{1/2} \exp\left[-\frac{1}{\alpha_x}(v_x - u_x)^2\right], \tag{7.1}$$

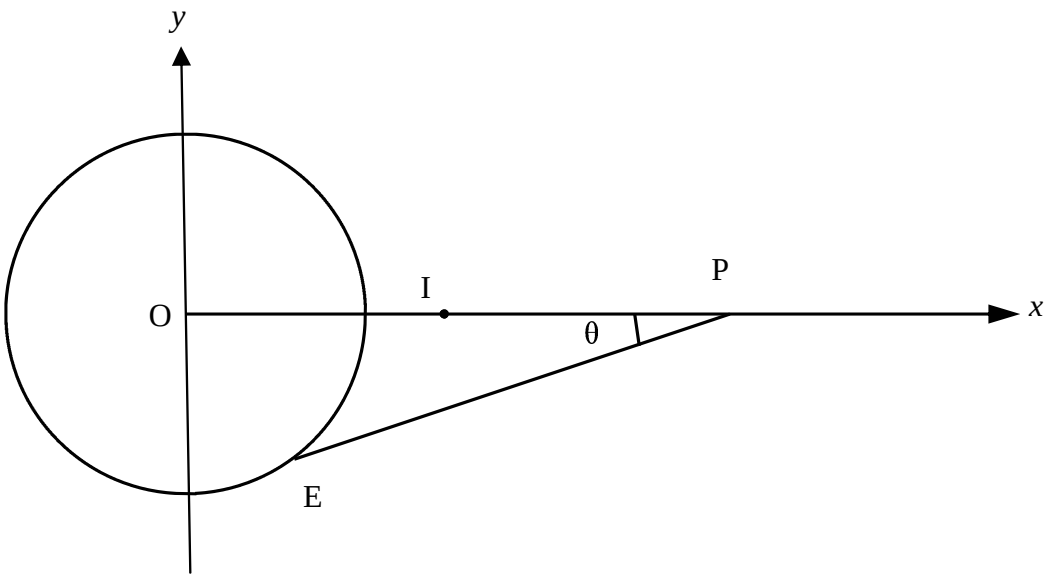

Figure 7.2: Radial LOS geometry. Point O is the Sun center, E is a point on the disk emitting the exciting radiation, P is a point along the radial in the corona and I is the position of the observer. The x-axis points along the radial direction with the origin at Sun center. θ is the angle OPE.

where

$$\alpha_x = \frac{2kT_x}{m}.$$

T_x is the temperature parallel to solar radial, v_x is the particle velocity parallel to solar radial and u_x is the outflow speed along the radial. k is the Boltzmann constant and m is the ion mass.

At wavelength λ, the collisional intensity of a spectral line with a center rest wavelength of λ_0 viewed by an observer positioned a distance x_I from the Sun center along the radial x-axis can be written as (the generic form is given by equation 2.3 of chapter 2 or see Withbroe et al. (1982)):

$$I_c(\lambda) = \frac{1}{4\pi} \int_{-\infty}^{\infty} \int_{x_I}^{\infty} q_c \, n_i \, n_e \; f(v_x) \, \delta\left(\lambda_0 - \lambda - \frac{\lambda_0}{c} v_x\right) dx \, dv_x, \tag{7.2}$$

where q_c is the collisional excitation rate coefficient of the atomic transition. The delta function in the integral over the velocity distribution selects only those ions at the correct velocity to emit at the observed wavelength, $v_x = c\,(\lambda_0 - \lambda)\,/\lambda_0$. Substituting for v_x in equation 7.1 gives an analytical form of equation 7.2 that can be integrated over x to give the collisional intensity at wavelength λ:

$$I_c(\lambda) = \frac{1}{4\pi} \left(\frac{1}{\pi\alpha_x}\right)^{1/2} \int_{x_I}^{\infty} q_c \, n_i \, n_e \exp\left(-\frac{1}{\alpha_x}\left[\frac{c}{\lambda_0}\,(\lambda_0 - \lambda) - u_x\right]^2\right) dx. \tag{7.3}$$

7.2.2 Radiative Component

A rigorous treatment of the radial LOS radiative component demands the inclusion of the velocity distribution perpendicular to the LOS. This would be redundant if the Sun was approximated as a point source. A bi-Maxwellian velocity distribution which is symmetric around the *x*-axis is assumed:

$$f(v_x, v_y) = \left(\frac{1}{\pi\alpha_x}\right)^{1/2}\left(\frac{1}{\pi\alpha_y}\right)\exp\left[-\frac{1}{\alpha_x}(v_x - u_x)^2 - \frac{v_y^2}{\alpha_y}\right], \tag{7.4}$$

where

$$\alpha_y = \frac{2kT_y}{m}.$$

T_y is the temperature perpendicular to solar radial and v_y is the particle velocity perpendicular to solar radial.

The radiative intensity for a radial LOS with a disk emission $I(\lambda', \theta)$ symmetric around the disk center is given by (the generic form is given by equation 2.4 of chapter 2 or see Withbroe et al. (1982) or Li et al. (1998)):

$$I_r(\lambda) = \frac{hB_{12}}{4\pi\lambda_0}\int_{-\infty}^{\infty}\int_{-\infty}^{\infty}\int_{x_I}^{\infty}\int_{-\infty}^{\infty}\int_{0}^{\theta_{max}} n_i\, 2\pi\sin\theta\left[a + b\cos^2\theta\right] I(\lambda', \theta)$$
$$\times f(v_x, v_y)\,\delta\left(\lambda' - \lambda_0 - \frac{\lambda_0}{c}\left[v_x\cos\theta + v_y\sin\theta\right]\right)\delta\left(\lambda_0 - \lambda - \frac{\lambda_0}{c}v_x\right) d\theta\, d\lambda'\, dx\, dv_x\, dv_y, \tag{7.5}$$

where B_{12} is the Einstein coefficient and $I(\lambda', w)$ is the incident chromospheric radiation at wavelength λ'. θ_{max} is the maximum angle subtended by the Sun's disk at P, the position of the emission volume. The scattering profile is $a + b\cos^2\theta$. For O VI 1032, a is 7/8 and b is 3/8; for O VI 1037 there is no preference for scattering direction therefore a is 1 and b is 0 (Noci et al., 1987). For H Ly-α, a is 11/12 and b is 3/12.

In the integral over the velocity distribution, the first delta function selects only those ions which have the correct velocity to be in resonance with the incident wavelength, $v_x\cos\theta + v_y\sin\theta = c(\lambda' - \lambda_0)/\lambda_0$. The second delta function selects only those ions emitting at wavelength λ as seen by the observer, $v_x = c(\lambda_0 - \lambda)/\lambda_0$. Substituting for v_x and v_y in equation 7.4 gives an analytical form for equation 7.5 that can be integrated over x, θ and λ' to give the radiative intensity at wavelength λ:

$$I_r(\lambda) = \frac{hB_{12}}{2\lambda_0} \int_{x_I}^{\infty} \int_{-\infty}^{\infty} \int_0^{\theta_{max}} n_i \ \sin\theta \left[a + b\cos^2\theta\right] I\left(\lambda', \theta\right) \left(\frac{1}{\pi\alpha_x}\right)^{1/2} \left(\frac{1}{\pi\alpha_y}\right)$$
$$\times \exp\left[-\frac{1}{\alpha_x}\left(\frac{c}{\lambda_0}[\lambda_0 - \lambda] - u_x\right)^2 - \frac{c^2}{\alpha_y \lambda_0^2 \sin^2\theta}\left(\lambda' - \lambda_0 - \cos\theta\,[\lambda_0 - \lambda]\right)^2\right] d\theta\, d\lambda'\, dx \qquad (7.6)$$

7.3 Modelled O VI Profiles

O VI profiles are calculated using equations 7.3 and 7.6 for coronal hole and streamer solar wind conditions, for two different temperature anisotropies and for many different heights. For this purpose, we use solar wind parameters obtained from a global two-dimensional magnetohydrodynamic (MHD) three fluid model which extends from the coronal base out to 1 AU (Dr.Bo Li from the University of Wales Aberystwyth, private communication). The solar wind consists of electrons, protons and O^{5+} ions. The electrons are heated by thermal conduction and Coulomb collisions and the ion species are heated by an empirical energy flux. An *ad hoc* field-aligned momentum addition is applied to O^{5+} to help accelerate them so that the speed profile is constrained by UVCS observations. The model is further constrained by *in situ* measurements of the fast and slow solar wind close to Earth. The 2D model corresponds to a solar minimum scenario, with fast wind from a large radially diverging polar coronal hole and slow wind from an equatorial streamer. Two radial paths are taken through the 2D grid of model results, one at position angle 0° directly above the polar coronal hole and another at 90° centered on the equatorial streamer. Plasma conditions from 4 to $30R_\odot$ are shown in figure 7.3.

Figures 7.4 to 7.7 show O VI 1032 and 1037 collisional and radiative profiles calculated for radial lines of sight. The profiles of figures 7.4 and 7.5 are calculated for the equatorial streamer, figures 7.6 and 7.7 for the polar coronal hole. The calculations have been repeated for profiles observed at eight heights - 4, 5, 6, 7, 8, 10, 15 and 20 $R_\odot$. Figures 7.4 and 7.6 have been calculated with a narrow radial velocity distribution, with $T_\parallel$ set at 1% of the ion temperature profiles shown in figure 7.3 but without dropping under T_e, also shown in figure 7.3. Figures 7.5 and 7.7 are calculated for a wide radial velocity distribution, with $T_\parallel$ equal to the ion temperature profiles shown in figure 7.3.

The collisional profiles reflect the velocity distribution of the emitters along the LOS in an

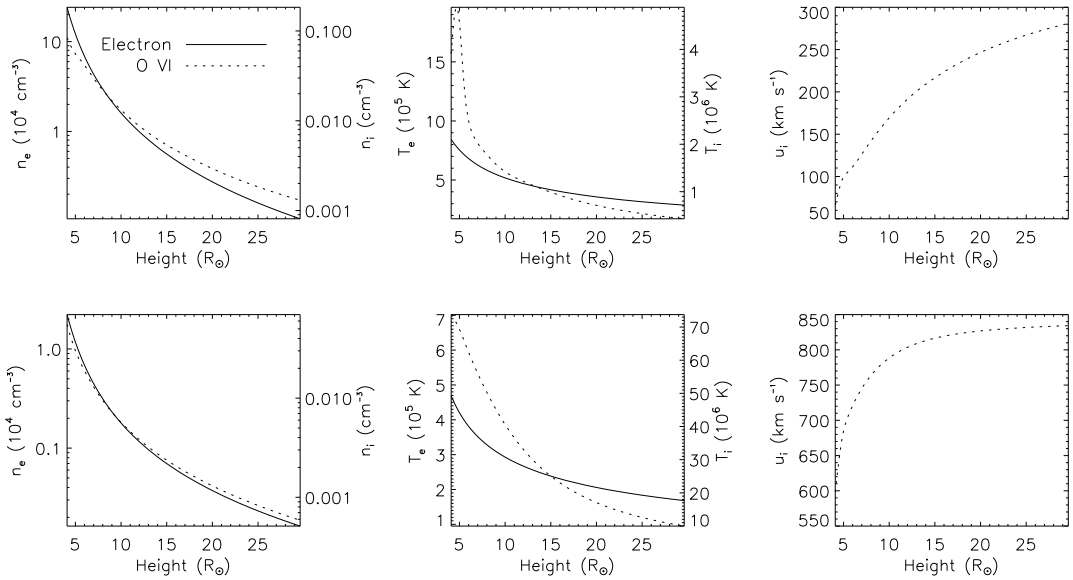

Figure 7.3: Plasma conditions obtained from the MHD 3-fluid model from 4 to $30R_{\odot}$ for the equatorial streamer (top row) and the polar coronal hole (bottom row). The left column shows electron and O^{5+} density, the middle shows electron and O^{5+} temperature and the right shows O^{5+} outflow velocity.

intuitive manner. The outflow velocity u_x results in a simple bulk Doppler shift of the collisional spectral profile to wavelength $u_x\lambda_0/c$. The increase of u_x along the LOS leads to a skewing of the profile, with a wider wing at longer wavelengths.

At low $T_{\|}$, the 1032 radiative profiles dim sharply with increasing velocity. Indeed, the radiative component in the coronal hole with low $T_{\|}$ is so low as to be undetectable at all heights (figure 7.6). The high velocities and low $T_{\|}$ do not allow any resonance between the chromospheric 1032 line and the coronal ions. With a higher $T_{\|}$ (figure 7.7), the coronal velocity distribution is broad enough to allow some coronal ions to resonate.

The 1037 radiative profiles are very interesting. Taking the high $T_{\|}$ streamer profiles as an example (figure 7.5), at the lower heights one can see the resonance peak at 1037.6Å dimming to zero with increasing outflow velocity and height in a predictable and similar way to the 1032 resonance line. However, there is a secondary peak at 1038.3Å which increases in resonance with increasing outflow. At heights of 15 and $20R_{\odot}$, a third resonance peak develops at 1038.8Å. An insight into the basic behavior of this equation can be found by making the approximation of the Sun as a point source so that θ is zero and v_y is redundant. In this case, the delta functions of equation 7.5 are only non-zero when $v_x = c\left(\lambda' - \lambda_0\right)/\lambda_0$ and $v_x = c\left(\lambda_0 - \lambda\right)/\lambda_0$. Equating v_x, this

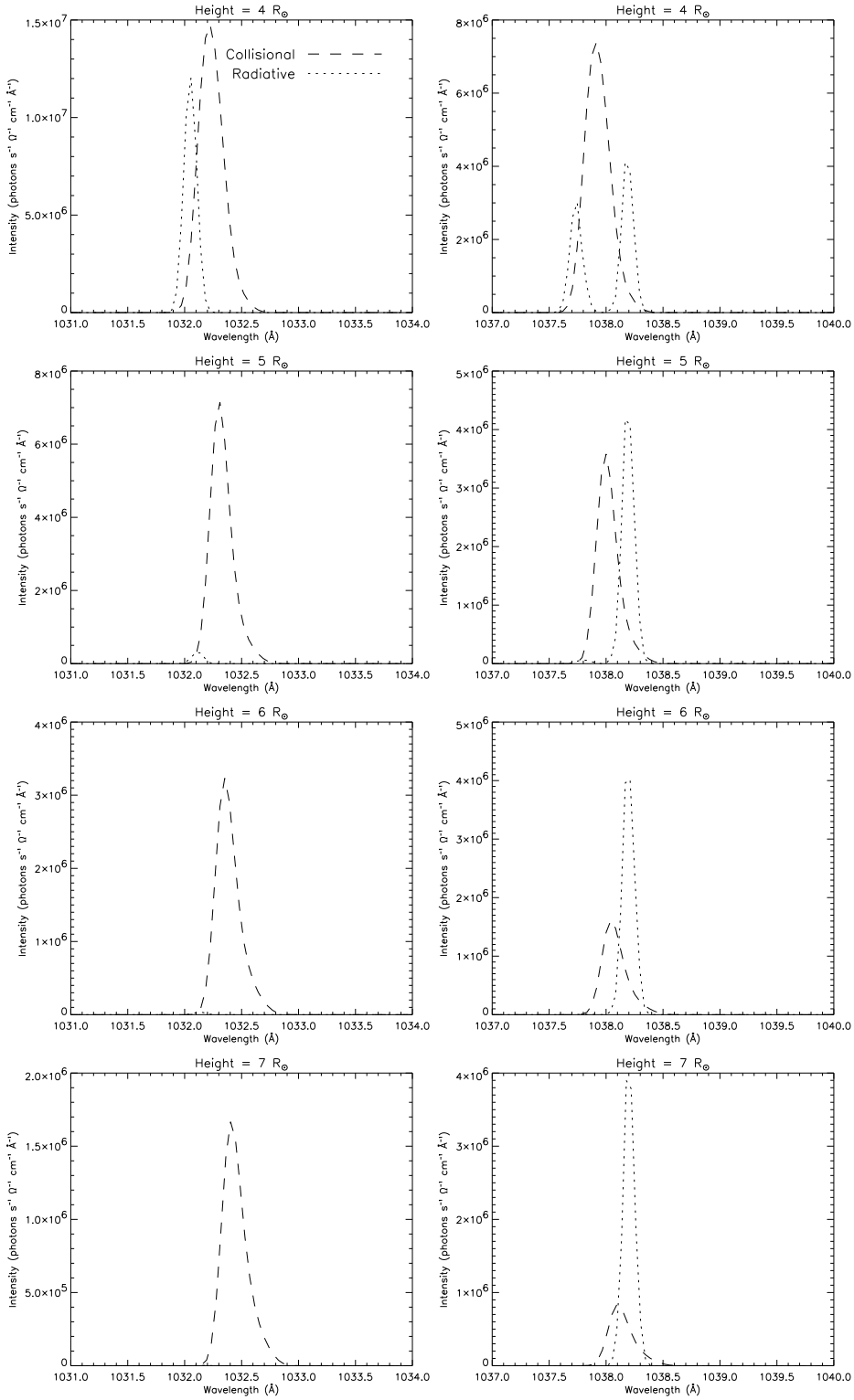

Figure 7.4: Modelled O VI profiles for an equatorial streamer and a low $T_{\|}$ ($T_{\|} = 0.01T_{\perp}$). The left column is for O VI 1032 and the right for O VI 1037. The height of the observer along the radial is increased from 4 to $20R_{\odot}$. This height is labeled above each plot. The dotted line gives the radiative profile and the dashed is the collisional.

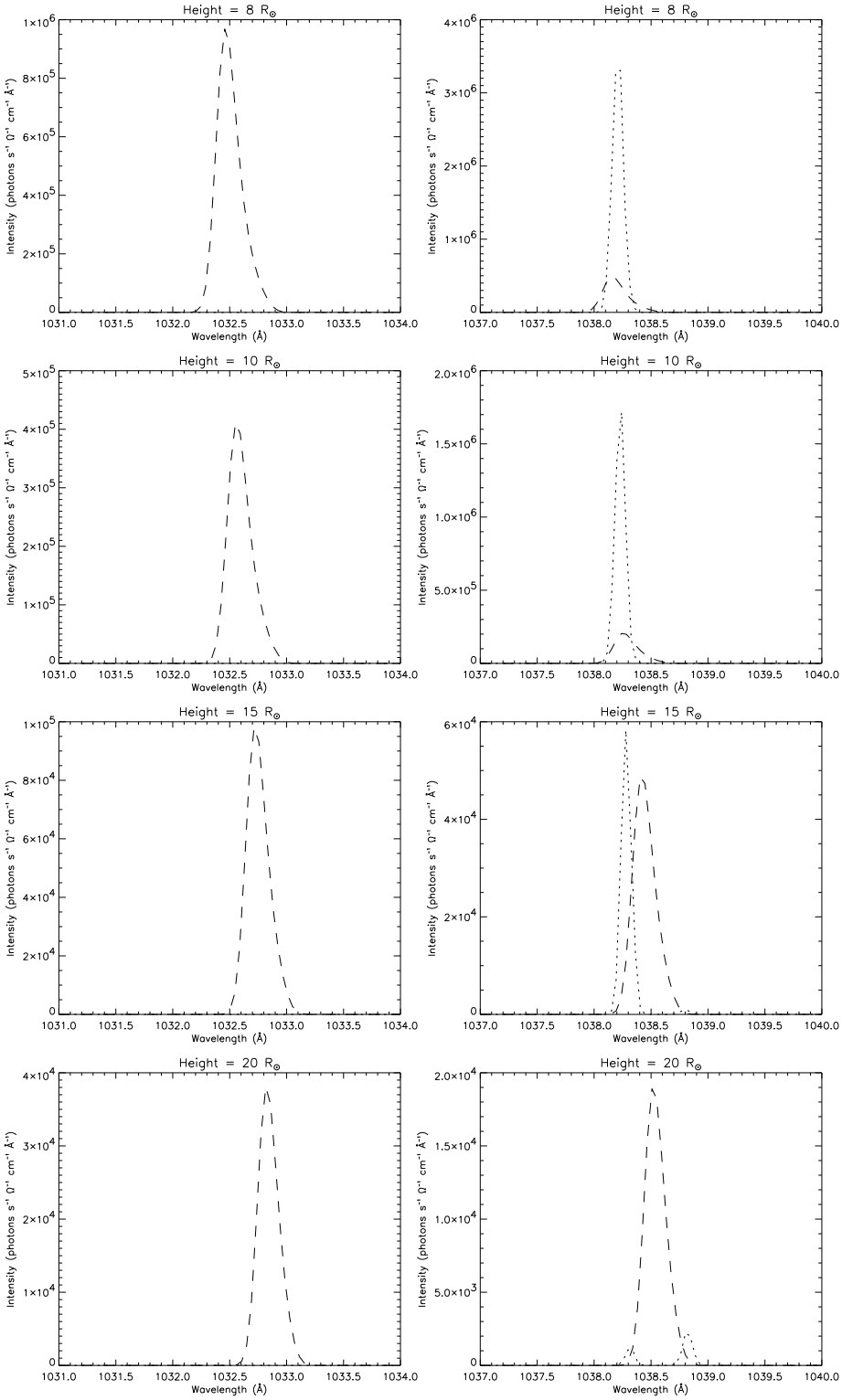

(Figure 7.4 continued)

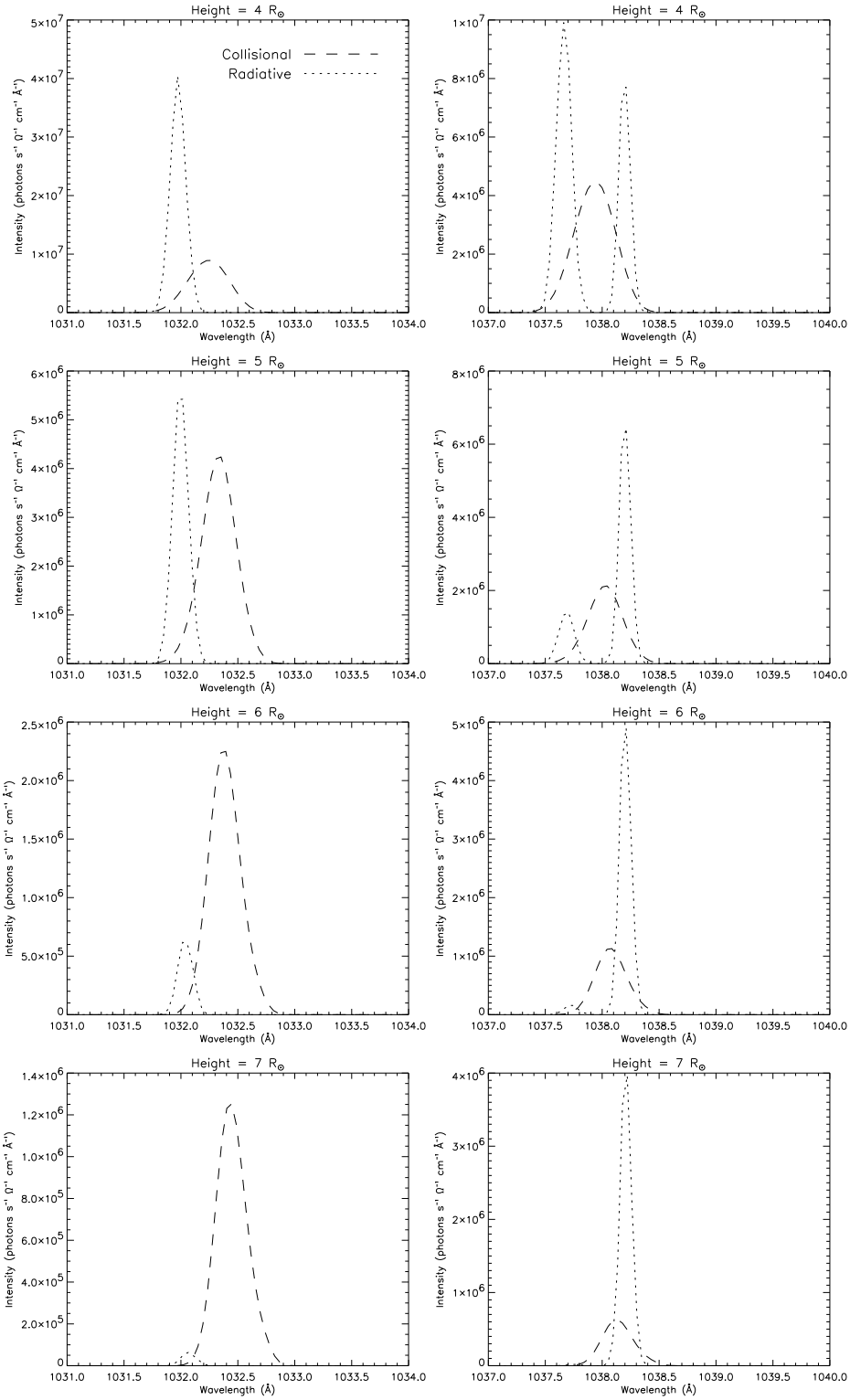

Figure 7.5: Modelled O VI profiles for an equatorial streamer and a high $T_{\|}$ ($T_{\|} = T_{\perp}$, isotropic). The left column is for O VI 1032 and the right for O VI 1037. The height of the observer along the radial is increased from 4 to $20R_{\odot}$. This height is labeled above each plot. The dotted line gives the radiative profile and the dashed is the collisional.

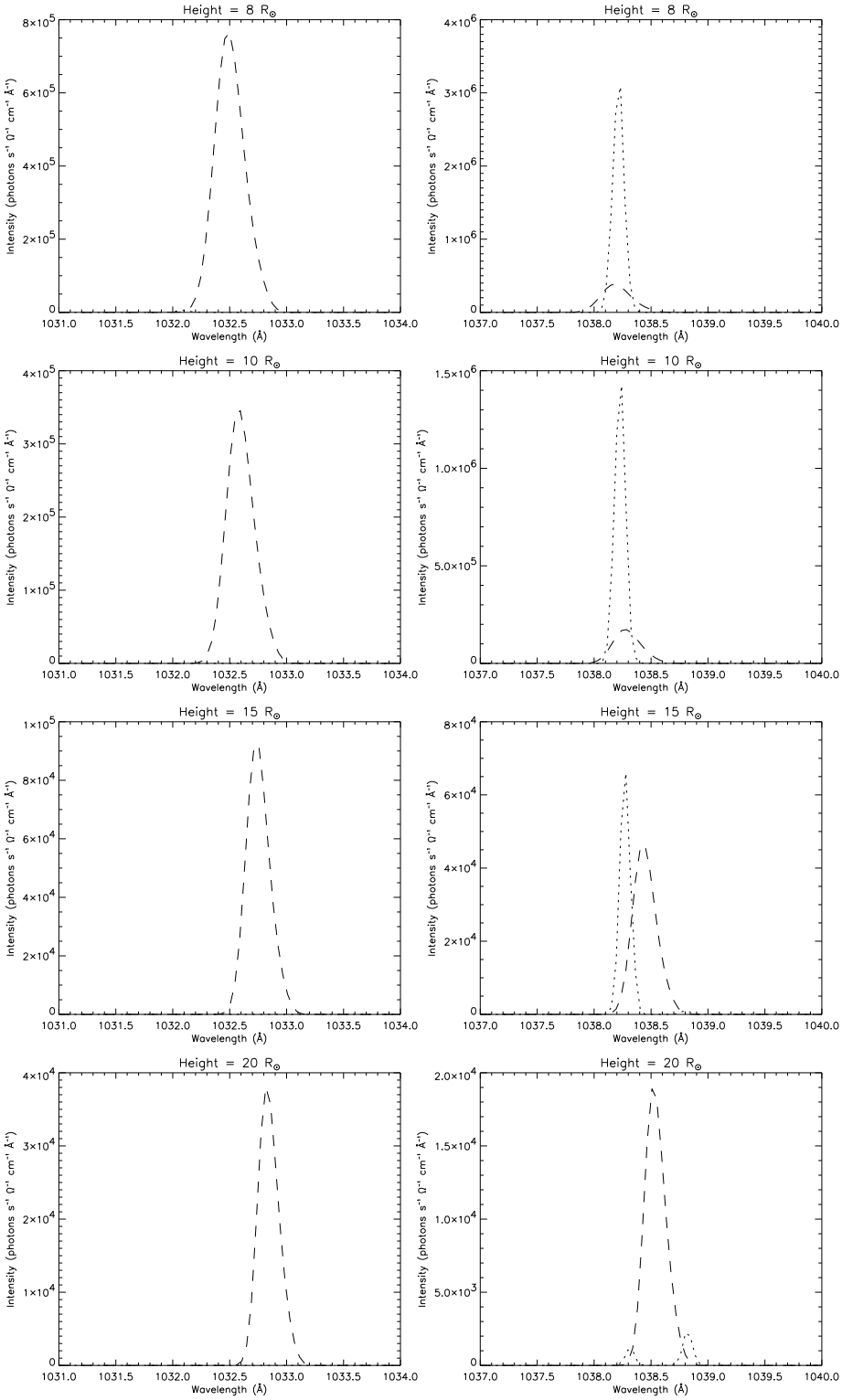

(Figure 7.5 continued)

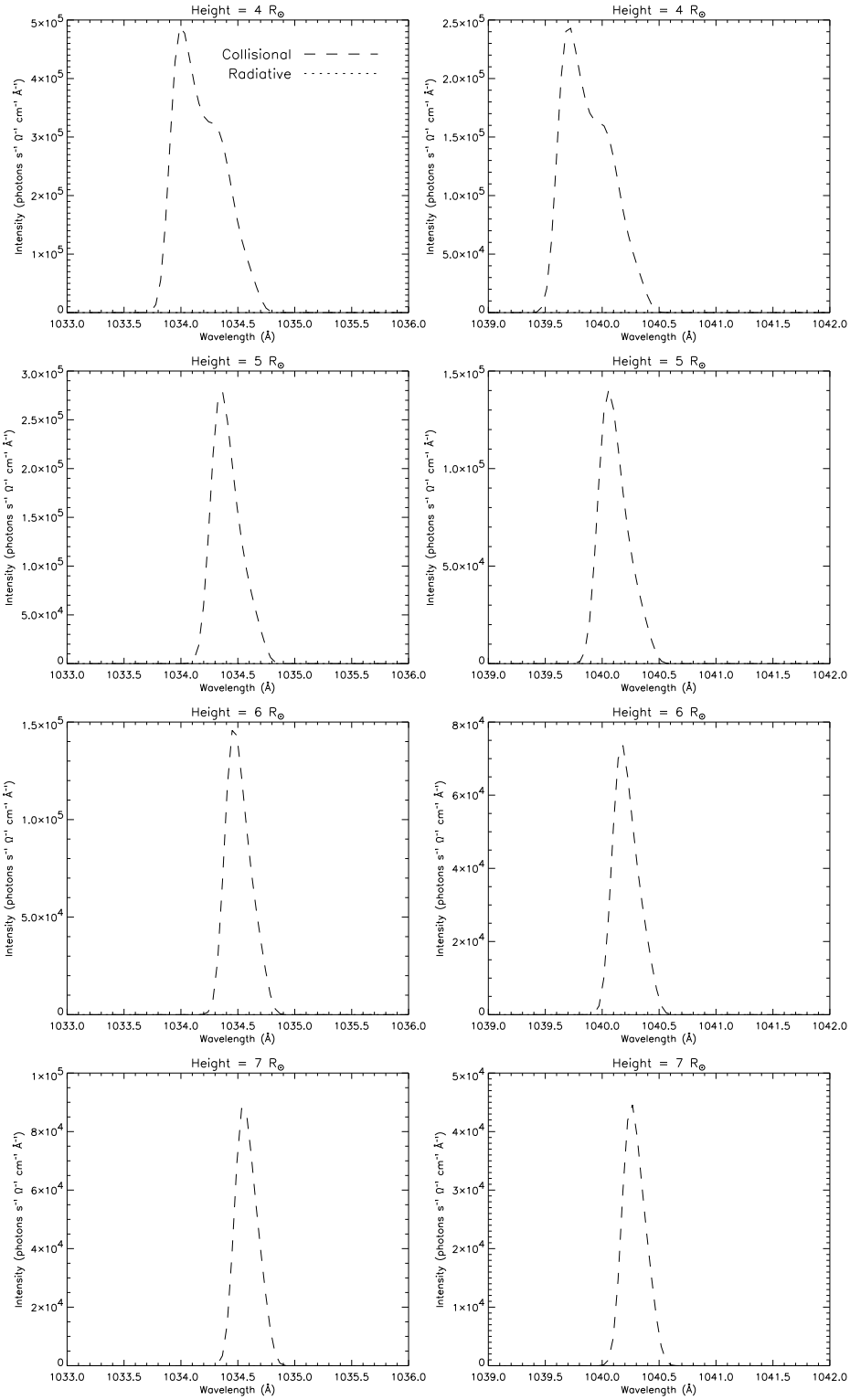

Figure 7.6: Modelled O VI profiles for a polar coronal hole and a low $T_{\|}$ ($T_{\|} = 0.01T_{\perp}$). The left column is for O VI 1032 and the right for O VI 1037. The height of the observer along the radial is increased from 4 to $20R_{\odot}$. This height is labeled above each plot. The dotted line gives the radiative profile and the dashed is the collisional.

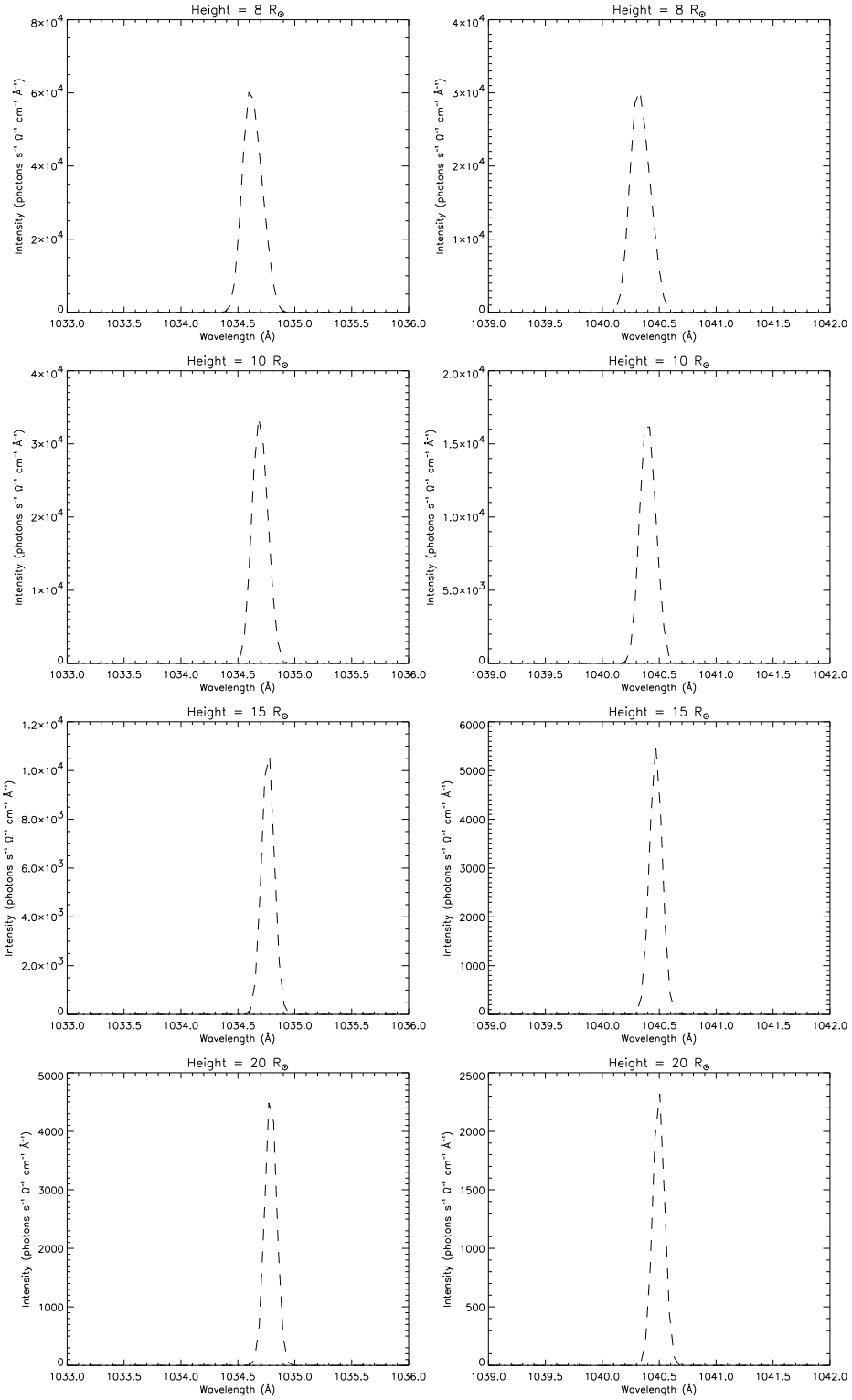

(Figure 7.6 continued)

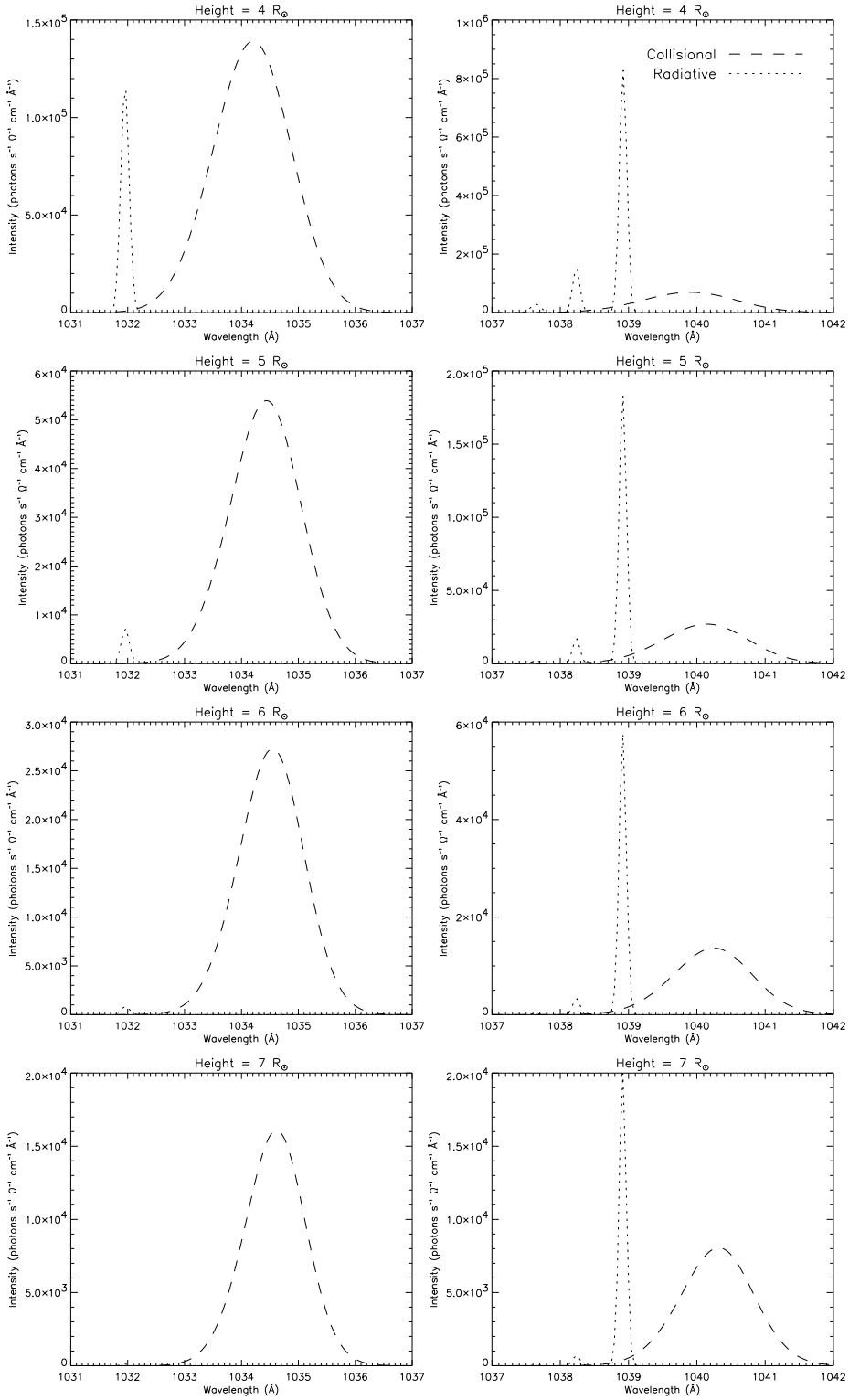

Figure 7.7: Modelled O VI profiles for a polar coronal hole and a high $T_{\|}$ ($T_{\|} = T_{\perp}$, isotropic). The left column is for O VI 1032 and the right for O VI 1037. The height of the observer along the radial is increased from 4 to $20R_{\odot}$. This height is labeled above each plot. The dotted line gives the radiative profile and the dashed is the collisional.

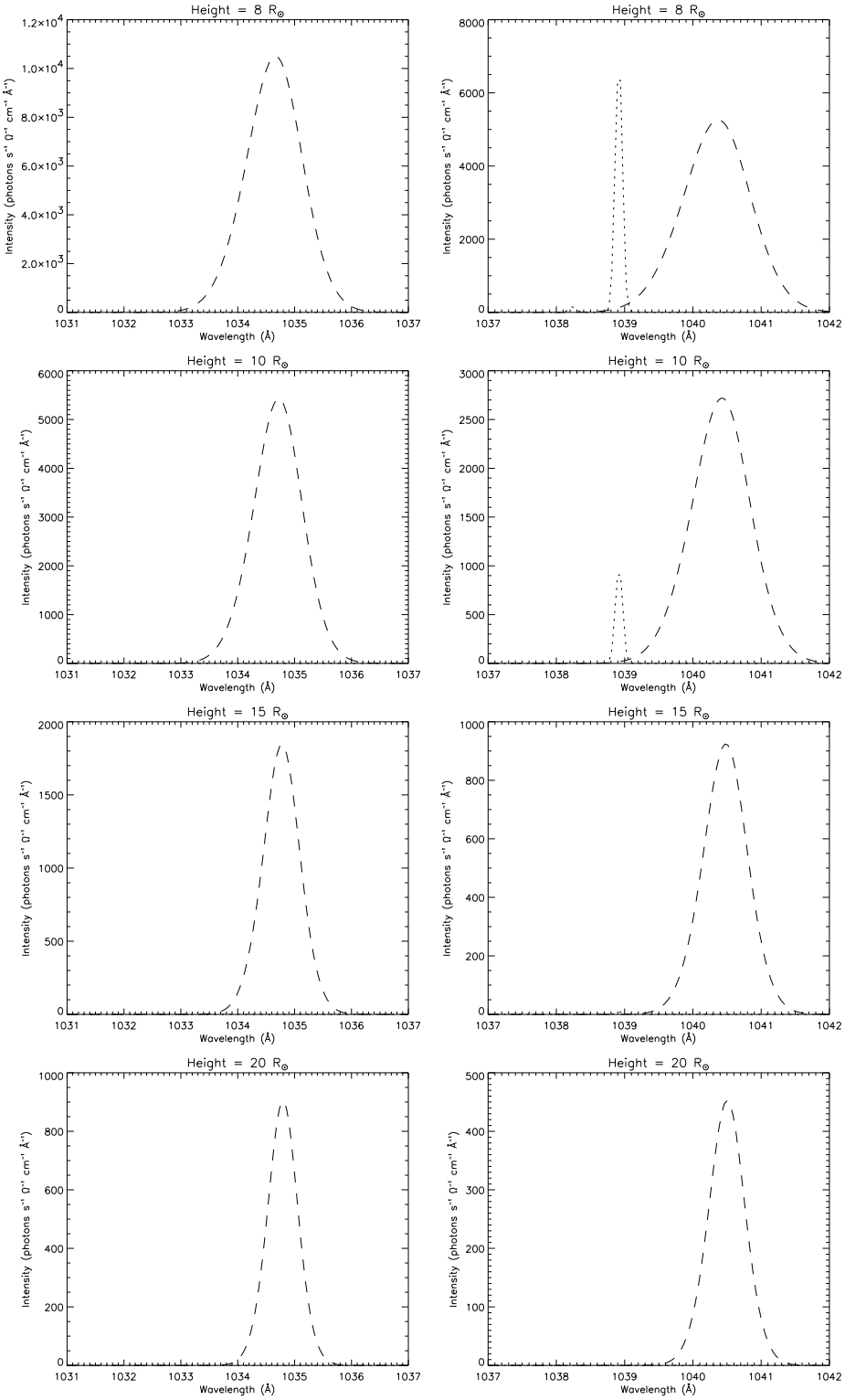

(Figure 7.7 continued)

gives the simple relationship

$$\lambda_0 = \frac{(\lambda + \lambda')}{2}.$$

Thus the intensity of an observed wavelength $\lambda_0 + \Delta\lambda$ is related to the chromospheric intensity at wavelength $\lambda_0 - \Delta\lambda$. The modelled coronal resonance peaks seen at 1038.3 and 1038.8Å are therefore caused by the chromospheric CII doublet at 1037 and 1036.3Å. If a volume of emitters in the corona had a uniform and wide distribution of velocities rather than a peaked Maxwellian distribution, their observed emission would be an exact scaled copy of the chromospheric spectrum, mirrored around λ_0.

7.4 Discussion and Conclusion

The most exciting aspect of radial LOS profiles is the separation of the collisional and radiative profiles which is not possible with 90° scattering. This will allow far better diagnostics for calculating outflow velocities. Firstly, the narrow resonance peaks give a direct wavelength calibration, and the separation of the radiative and collisional components give a direct measure of the bulk outflow velocity. Secondly, given a concurrent observation of the chromospheric spectrum, the relative balance of the 1037 coronal resonance peaks give a second measurement of outflow velocity. Thirdly, the degree of skewness of the 1037 line may give clues to the gradient of outflow velocity along the LOS.

The width of the collisional profile gives a direct measurement of the temperature along the radial, $T_{\parallel}$, a value which at present is only weakly constrained by the semi-empirical modelling of UVCS observations. Since the outflow velocity is measured directly by the red-shift of the collisional profile, the widening of the profile due to the bulk outflow may be removed. The downside of a radial LOS compared to the current UVCS is it cannot measure $T_{\perp}$. However, UVCS has already measured $T_{\perp}$ for over half a solar cycle.

The emission contribution to a radial LOS is more localized compared to the 90° scattering LOS. Consider, for example, a spherically symmetric corona with a typical sharp drop in density with height. The proposed instrument lies in the corona and the main contribution to the observed line intensities comes from the highest density of ions in the locality of the instrument itself. The LOS of the current UVCS passes through both sides of the region of highest density closest to the

Sun. Another technical advantage of a radial LOS would be the lack of contamination by stray light from the Sun's disk, which can be a problem with some observations made by the current UVCS (see section 3.4.4 of chapter 3).

The prospect of a new UVCS aboard Solar Probe is therefore very exciting. The UV spectral observations, combined with *in situ* measurements of electrons, protons and the coronal magnetic field will give unsurpassed constraints on models of solar wind heating and acceleration.

Chapter 8

Conclusion and Perspectives

8.1 Conclusion

Advancements in observations, in particular UV observations of the last thirty years, have led to an enormous growth in the knowledge of the plasma properties of the solar corona. UVCS remains the only instrument capable of providing measurements of the acceleration region of the solar wind that can provide abundance, temperature and outflow velocity. UVCS observations provide essential constraints on models of coronal heating and acceleration unavailable by any other means.

The basic modelling of O VI lines for typical coronal hole conditions in chapter 2 shows the power of the O VI intensity ratio as a diagnostic tool for outflow velocity. The modelling gives evidence of a $T_{\parallel} < T_{\perp}$ anisotropy, in agreement with previous observations of coronal holes by UVCS at solar minimum. A study which investigates the sensitivity of the intensity ratio to various parameters showed that a contribution from sunspots in the incident disk spectrum has a large impact on the behavior of the O VI intensity ratio at velocities below ~180 km s^{-1}.

The inversion method introduced in chapter 4 is successful in calculating ion densities, outflow velocities and temperatures. A narrow solar maximum streamer and a neighboring non-streamer region have a slow but significant ion outflow which increases between 3.1 and 5.1$R_{\odot}$. There is far less contrast between the plasma parameters of the streamer and the neighboring region than that seen in solar minimum observations. Nevertheless, the non-streamer region of this study is significantly different from the streamer in most parameters. This suggests that some regions of the solar maximum corona can not, in UVCS observations, be associated with coronal holes nor

streamers, and may best be defined as the quiet corona.

Using the calculated mass flux and an assumption of a radially expanding corona, a $T_{\parallel} = 2T_{\perp}$ ion temperature anisotropy is shown to be unlikely for both the streamer and non-streamer region. A $T_{\parallel} = 0.1T_{\perp}$ anisotropy gives the best mass flux continuity for the non-streamer region. The mass flux is not so well preserved in the narrow streamer. This may be due to the non-radial expansion of the streamer or due to disturbances within the streamer caused by small mass ejections. A decreasing ion to electron density ratio with height in the non-streamer region may reflect a preferential acceleration of O^{5+} ions.

Applying the inversion method to observations of a large solar maximum active region streamer results initially in zero outflow velocity at low heights and, from results obtained at many heights within the streamer, an unrealistic mass flux. However, MDI images of the Sun's disk reveal a large sunspot associated with the base of the active region streamer. The degree of sunspot contribution to the incident quiet Sun disk spectrum of the line emission model is found to be a critical parameter. A contribution of 3-5% from sunspots allows the convergence of the iterative scheme to non-zero outflow velocities and a self-consistent mass flux. Mass flux is also used to explore the O VI temperature anisotropy. An O VI temperature anisotropy $T_{\parallel}/T_{\perp}$ value of 2 gives unphysical mass flux. A $T_{\parallel}/T_{\perp}$ value of 0.2 leads to mass flux compatible only with a superradial expansion of the streamer. An isotropic $T_{\parallel}/T_{\perp}$ value of 1 gives a mass flux compatible with a radial streamer expansion. This is evidence of an isotropic temperature distribution in the streamer. Comparing the streamer ion and electron densities shows no evidence of preferential acceleration of O^{5+} ions within this active region streamer.

A significant difference in O VI 1032 and 1037 linewidths is often seen in UVCS observations. The parameter study of chapter 3.6 shows that the differences are primarily due to the varying balance of collisional and radiative components in each spectral line, a balance which depends on Doppler dimming and pumping. Any difference in width between the 1032 and 1037 radiative profiles caused by outflow velocity gradients along the LOS are secondary effects. Temperature gradients or inhomogeneities within the corona are also secondary in importance. The 1032/1037 linewidth ratio can in some cases give added constraints on outflow velocity and temperature anisotropy in the empirical modelling of UVCS observations.

The application of a wavelet analysis technique to Ly-α UVCS observations conducted in chap-

ter 6 shows that sporadic oscillations with significant power exist in the line intensity. A preference toward 7-8 minute oscillations in 3 out of the 4 observations analysed is found, in general agreement with the results of Ofman et al. (2000). The oscillations are interpreted as signatures of fast or slow magnetosonic waves propagating outwards in the corona. This suggests that pure Alfvén waves, which have never been observed in the corona, are not the only waves present there.

Chapter 7 looks forward to the prospect of an UV spectrometer aboard the Solar Probe spacecraft. Such an instrument would necessarily use a radial LOS, pointing away from the Sun. A radial LOS is shown to promise excellent diagnostics due to the separation of the O VI collisional and radiative profiles with non-zero outflow velocities. UV spectral observations from aboard Solar Probe, combined with *in situ* measurements of electrons, protons and the coronal magnetic field will give unsurpassed constraints on models of solar wind heating and acceleration.

8.2 Perspectives

8.2.1 The Iterative Inversion Scheme

Many refinements will be made to the iterative inversion scheme introduced in chapter 4. The most pressing issue is the geometry of the inversion. The plane of sky approximation used in this thesis is certainly inadequate for observations of coronal holes or quiet coronal regions. In such cases, a spherically symmetrical inversion must be made. An algorithm for such an inversion is outlined in chapter 3.6. A rigorous approach to streamer observations would be an axisymmetric inversion, with an axis of symmetry along the streamer center and two sets of adjustable ion parameters for the streamer and non-streamer regions along the LOS. The non-streamer parameters can be constrained by applying a spherical symmetrical inversion to UVCS observations of a region neighboring the streamer. The extent and position of the streamer along the LOS can be found by tomographic analysis of white light observations and/or UVCS synoptic observations. A similar improvement can also be made in the inversion of streamer pB observations to obtain electron density along the LOS. The O VI 1032/1037 linewidth ratio will help constrain parameters when using an extended LOS geometry.

The iterative algorithm introduced in chapter 4 uses as input the intensity, linewidth and intensity ratio obtained from fitting the observed O VI profiles to Gaussian profiles. It would be interesting

to develop an algorithm which directly compares observed and synthesized profiles without fitting to Gaussians. Such an algorithm could be applied to observed O VI profiles which do not fit well to a single Gaussian (see, for example, the two Gaussian profiles discussed in section 3.5.3 of chapter 3). This approach could be used to explore coronal parameters that lead to the commonly observed two Gaussian profiles of O VI lines.

The iterative scheme is a diagnostic tool which is not limited to UVCS observations of O VI. Soon the scheme will be tested on SUMER observations of O VI made at heights below $1.5R_{\odot}$ in the corona. The goal is to apply the scheme on a set of coordinated SUMER and UVCS observations from 2000 May, and to calculate O^{5+} parameters from very low in the corona up to the highest UVCS observation from this dataset at $\sim 5.1R_{\odot}$. The goal of this analysis would be a deeper understanding of the structure and conditions in the solar maximum corona.

8.2.2 UVCS Time Analysis

A detailed time analysis will be made on a far larger set of UVCS observations than used in chapter 6. In 2004, observations were tailored specifically for the time analysis of Ly-α and O VI intensity. A short cadence of 60s was used to enable wavelet analysis down to timescales of $\sim$2 minutes, and extremely long observations were made of the same region in the corona, in order to detect long period oscillations.

Preliminary results have shown tentative evidence of significant quasi-periodic oscillations in O VI intensity. There are issues which need to be addressed arising from the low O VI photon counts in most coronal regions. A model of Gaussian noise is used to test the significance of Ly-α fluctuations in the analysis of chapter 6, justified by the reasonably high photon counts at each time step. The generally lower photon counts measured in the O VI lines may demand a model of Poisson distributed noise. Multiresolution algorithms are being applied to O VI data to remove noise and isolate signals with significant quasi-periodic oscillations.

The line emission code described in chapter 2 will be used to find the amplitude of the density waves necessary to create the observed oscillations in intensity. The modelled amplitude of density waves would depend strongly on the extent of the source of oscillations along the LOS. A narrow source would mean a higher amplitude.

8.2.3 UVCS on Solar Probe

The approval of a new UV spectrometer aboard the Solar Probe spacecraft would demand a further development of the radial LOS model described in chapter 7. An iterative inversion scheme with a radial LOS is envisaged, with many parameters tightly constrained by the *in situ* measurements made by Solar Probe such as electron density and temperature.

Bibliography

Allen, L. A., Habbal, S. R., & Li, X., *Thermal coupling of protons and neutral hydrogen with anisotropic temperatures in the fast solar wind*, 2000, J.Geophys.Res., 23123

Antonucci, E., Dodero, M. A., Giordano, S., Krishnakumar, V., & Noci, G., *Spectroscopic measurement of the plasma electron density and outflow velocity in a polar coronal hole*, 2004, A&A, 416, 749

Banerjee, D., O'Shea, E., Doyle, J. G., & Goossens, M., *Long period oscillations in the inter-plume regions of the Sun*, 2001, A&A, 377, 691

Balogh, A., & Forsyth, R. J., *The Results of the ULYSSES Mission: A Survey of the Heliosphere in Three Dimensions*, 1998, ESA SP-417: Crossroads for European Solar and Heliospheric Physics. Recent Achievements and Future Mission Possibilities, 45

Barford, N.C., *Experimental Measurements: Precision, Error and Truth*, 1985, John Wiley & Sons, 2nd edition

Beckers, J.M., & Chipman, E., *The Profile and Polarization of the Coronal Ly-α Line*, 1974, Sol.Phys., 34, 151

Bemporad, A., Poletto, G., Suess, S. T., Ko, Y. K., Parenti, S., Riley, P., Romoli, M., & Zurbuchen, T. Z., *Temporal Evolution of a Streamer Complex: Coronal and in Situ Plasma Parameters*, 2003, ApJ, 593, 1146

Bevington, P.R., & Robinson, D.K., *Data Reduction and Error Analysis for the Physical Sciences*, 1992, McGraw-Hill, 2nd edition

Biermann, L., *Solar corpuscular radiation and the interplanetary gas*, 1957, The Observatory, 77, 109

Breen, A. R., Coles, W. A., Grall, R., L_vhaug, U.-P., Markkanen, J., Misawa, H., & Williams, P. J. S., *EISCAT measurements of interplanetary scintillation*, 1996, Journal of Atmospheric and Terrestrial Physics, 58, 507

Breen, A. R., et al., *Measurements of the solar wind over a wide range of heliocentric distances - a comparison of results from the first three Whole Sun Months*, 2000, Journal of Atmospheric and Terrestrial Physics, 62, 1527

Brueckner, G. E., et al., *The Large Angle Spectroscopic Coronagraph (LASCO)*, 1995, Sol.Phys., 162, 357

Carrington, R. C., *Description of a Singular Appearance seen in the Sun on September 1, 1859*, 1859, Monthly Notices of the Royal Astronomical Society, 20, 13

Clerke, A. M., *The problem of coronium* 1898, The Observatory, 21, 325

Cranmer, S. R., et al., *An Empirical Model of a Polar Coronal Hole at Solar Minimum*, 1999, ApJ, 511, 481

Cranmer, S. R., *Coronal Holes and the High-Speed Solar Wind*, 2002, Space Sci.Rev., 101, 229

Curdt, W., Dwivedi, B. N., & Feldman, U., *The EUV Spectrum of Sunspot Plumes Observed by SUMER on SOHO*, 2000, Journal of Astrophysics and Astronomy, 21, 397

Curdt, W., Brekke, P., Feldman, U., Wilhelm, K., Dwivedi, B. N., Schühle, U., & Lemaire, P., *The SUMER spectral atlas of solar-disk features*, 2001, A&A, 375, 591

DeForest, C.E., & Gurman, J.B., *Observation of Quasi-periodic Compressive Waves in Solar Polar Plumes*, 1998, ApJL, 501, L217

Doyle, J. G., Teriaca, L., & Banerjee, D., *Coronal hole diagnostics out to* $8R_{\odot}$, 1999, A&A, 349, 956

Feldman, W. C., Asbridge, J. R., Bame, S. J., Fenimore, E. E., & Gosling, J. T., *The solar origins of solar wind interstream flows - Near-equatorial coronal streamers*, 1981, J.Geophys.Res., 86, 5408

Feldman, U., Mandelbaum, P., Seely, J. F., Doschek, G. A., & Gursky, H., *The potential for plasma diagnostics from stellar extreme-ultraviolet observations*, 1992, ApJS, 81, 387

Feldman, U., Curdt, W., Doschek, G. A., Schuehle, U., Wilhelm, K., & Lemaire, P., *High-Temperature Lines in SUMER Spectra Recorded above a Bright Solar Active Region*, 1998, ApJ, 503, 467

Festou, M. C., Rickman, H., & West, R. M., *Comets. I - Concepts and observations*, 1993, A&A Rv, 4, 363

Fineschi, S., van Ballegoijen, A., & Kohl, J. L., *Coronal Magnetic Field Diagnostics with UV Spectropolarimetry*, 1999, ESA SP-446: 8th SOHO Workshop: Plasma Dynamics and Diagnostics in the Solar Transition Region and Corona, 8, 317

Frazin, R. A., Cranmer, S. R., & Kohl, J. L., *Empirically Determined Anisotropic Velocity Distributions and Outflows of O5+ Ions in a Coronal Streamer at Solar Minimum*, 2003, ApJ, 597, 1145

Gabriel, A. H., et al., *Rocket Observations of the Ultraviolet Solar Spectrum during the Total Eclipse of 1970 March 7*, 1971a, ApJ, 169, 595

Gabriel, A. H., *Measurements on the Lyman Alpha Corona (Papers presented at the Proceedings of the International Symposium on the 1970 Solar Eclipse, held in Seattle, U. S. A. , 18-21 June, 1971.)* 1971b, Sol.Phys., 21, 392

Gabriel, A.H., Bely-Dubau, F., & Lemaire, P., *The Contribution of Polar Plumes to the Fast Solar Wind*, 2003, ApJ, 589, 623

Gardner, L. D., Atkins, N., Fineschi, S., Smith, P. L., Kohl, J. L., Maccari, L., & Romoli, M., *Efficiency variations of UVCS/SOHO based on laboratory measurements of replica gratings*, 2000, Proc.SPIE, 4139, 362

Gardner, L. D., et al., *UV Radiometric Calibration of UVCS*, 2002, The Radiometric Calibration of SOHO, ISSI Scientific Report SR-002. Edited by A. Pauluhn, M.C.E. Huber and R. von Steiger. ESA Publications Division, Noordwijk, The Netherlands, 2002., 161

Geiss, J., Hirt, P., & Leutwyler, H., *On Acceleration and Motion of Ions in Corona and Solar Wind*, 1970, Sol.Phys., 12, 458

Geiss, J., et al., *The Southern High-Speed Stream - Results from the SWICS Instrument on ULYSSES*, 1995, Science, 268, 1033

Gold, R., *An Iterative Unfolding Method for Response Matrices*, 1964, AEC R&D Report ANL-6984

Gosling, J. T., Asbridge, J. R., Bame, S. J., Feldman, W. C., Borrini, G., & Hansen, R. T., *Coronal streamers in the solar wind at 1 AU*, 1981, J.Geophys.Res., 86, 5438

Guhathakurta, M., & Holzer, T. E., *Density structure inside a polar coronal hole*, 1994, ApJ, 426, 782

Habbal, S. R., Woo, R., Fineschi, S., O'Neal, R., Kohl, J., Noci, G., & Korendyke, C., *Origins of the Slow and the Ubiquitous Fast Solar Wind*, 1997, ApJL, 489, L103

Habbal, S. R., Woo, R., & Vial, J., *UVCS Observations of Velocity Shear at Streamer Boundaries in the Corona*, 2001a, Space Sci.Rev., 97, 5

Habbal, S. R., Woo, R., & Arnaud, J., *On the Predominance of the Radial Component of the Magnetic Field in the Solar Corona*, 2001b, ApJ, 558, 852

Hewish, A., Scott, P. F., & Wills, D., *Interplanetary Scintillation of Small Diameter Radio Sources*, 1964, Nature, 203, 1214

Hodgson, R., *On a curious Appearance seen in the Sun*, 1859, Monthly Notices of the Royal Astronomical Society, 20, 15

Hollweg, J.V., *Fast wave evanescence in the solar corona*, 1978, Geophys.Res.Lett., 5, 731

Hyder, C.L., & Lites, B.W., *Hα Doppler Brightening and Lyman-α Doppler Dimming in Moving Hα Prominences*, 1970, Sol.Phys. , 14, 147

Jansson, P.A., *Deconvolution of Images and Spectra*, 1997, Academic Press, 2nd edition

Ko, Y., Raymond, J. C., Li, J., Ciaravella, A., Michels, J., Fineschi, S., & Wu, R., *Solar and Heliospheric Observatory Ultraviolet Coronagraph Spectrometer and Yohkoh Soft X-Ray Telescope Observations of the High-Temperature Corona above an Active Region Complex*, 2002, ApJ, 578, 979

Kohl, J.L., Reeves, E.M., & Kirkham, B., *The Lyman Alpha Coronagraph*, 1978, New Instrumentation for Space Astronomy, Pergamon, New York, 91

Kohl, J. L., Weiser, H., Withbroe, G. L., Noyes, R. W., Parkinson, W. H., Reeves, E. M., Munro, R. H., & MacQueen, R. M., *Measurements of coronal kinetic temperatures from 1.5 to 3 solar radii*, 1980, ApJL, 241, 117

Kohl, J. L., & Withbroe, G. L., *EUV spectroscopic plasma diagnostics for the solar wind acceleration region*, 1982, ApJ, 256, 263

Kohl, J. L., Weiser, H., Withbroe, G. L., Zapata, C. A., & Munro, R. H., *Evidence for Supersonic Solar Wind Velocities at 2.1* $R_{\odot}$, 1984, Bulletin of the American Astronomical Society, 16, 531

Kohl, J. L., Gardner, L. D., Strachan, L., & Hassler, D. M., *Ultraviolet spectroscopy of the extended solar corona during the SPARTAN 201 mission*, 1994, Space Science Reviews, 70, 253

Kohl, J. L., et al., *The Ultraviolet Coronagraph Spectrometer for the Solar and Heliospheric Observatory*, 1995, Sol.Phys., 162, 313

Kohl, J. L., et al., *First Results from the SOHO Ultraviolet Coronagraph Spectrometer*, 1997, Sol.Phys., 175, 613

Kohl, J. L., et al., *UVCS/SOHO Empirical Determinations of Anisotropic Velocity Distributions in the Solar Corona* 1998, ApJL, 501, L127

Koutchmy, S., & Livshits, M., *Coronal Streamers*, 1992, Space Sci.Rev., 61, 393

Krieger, A. S., Timothy, A. F., & Roelof, E. C., *A Coronal Hole and Its Identification as the Source of a High Velocity Solar Wind Stream*,1973, Sol.Phys., 29, 505

Krüger, A., *Introduction to Solar Radio Astronomy and Radio Physics*, 1979, D. Reidel Publishing Co., Dordrecht, Holland

Li, X., Habbal, S. R., Kohl, J., & Noci, G., *The Effect of Temperature Anisotropy on Observations of Doppler Dimming and Pumping in the Inner Corona*, 1998, ApJL, 501, L133

Li, J., LaBonte, B., Acton, L., & Slater, G., *Persistent Coronal Streamers and the Identification of Sunspot Clusters*, 2002, ApJ, 565, 1289

Lyot, B., *tude de la couronne solaire en dehors des clipses. Avec 16 figures dans le texte*, 1932, Zeitschrift fur Astrophysics, 5, 73

Marsh, M.S., Walsh, R.W., De Moortel, I., Ireland, J., *Joint observations of propagating oscillations with SOHO/CDS and TRACE*, 2003, A&A, 404, L37

Mazzotta, P., Mazzitelli, G., Colafrancesco, S., & Vittorio, N., *Ionization balance for optically thin plasmas: Rate coefficients for all atoms and ions of the elements H to NI*, 1998, A&AS, 133, 403

McComas, D., *Solar Probe Status Report*, 2004, COSPAR, Paris

McIntosh, S. W., Diver, D. A., Judge, P. G., Charbonneau, P., Ireland, J., & Brown, J. C., *Spectral decomposition by genetic forward modelling*, 1998, A&AS, 132, 145

McIntosh, S.W., Fleck, B., Judge, P.G., *Investigating the role of plasma topography on chromospheric oscillations observed by TRACE*, 2003, A&A, 405, 769

Miralles, M. P., Cranmer, S. R., & Kohl, J. L., *Ultraviolet Coronagraph Spectrometer Observations of a High-Latitude Coronal Hole with High Oxygen Temperatures and the Next Solar Cycle Polarity*, 2001, ApJL, 560, L193

Morgan, H., Habbal, S.R., & Li, X., *Hydrogen Ly-α intensity oscillations observed by the Solar and Heliospheric Observatory Ultraviolet Coronagraph Spectrometer*, 2004, ApJ, 605, 521

Muglach, K., *Dynamics of solar active regions. I. Photospheric and chromospheric oscillations observed with TRACE*, 2003, A&A, 401, 685

Munro, R. H., & Withbroe, G. L., *Properties of a Coronal "hole" Derived from Extreme-Ultraviolet Observations*, 1972, ApJ, 176, 511

Nemec, A.F., & Nemec, J.M., *A test of significance for periods derived using phase-dispersion-minimization techniques*, 1985, AJ, 90, 2317

Neugebauer, M., Snyder, C.W., *Mariner 2 Observations of the Solar Wind 1: Average Properties*, 1966, J.Geophys.Res., 71, 4469

Noci, G., Kohl, J. L., & Withbroe, G. L., *Solar wind diagnostics from Doppler-enhanced scattering*, 1987, ApJ, 315, 706

Noci, G., et al., *First results from UVCS/SOHO*, 1997a, Adv.Space Res., 20, 2219

Noci, G., et al., *The quiescent corona and slow solar wind*, 1997b, ESA SP-404: Fifth SOHO Workshop: The Corona and Solar Wind Near Minimum Activity, 75

Ofman, L., Romoli, M., Poletto, G., Noci, G., & Kohl, J.L., *Ultraviolet Coronagraph Spectrometer Observations of Density Fluctuations in the Solar Wind*, 1997, ApJL, 491, L111

Ofman, L., Romoli, M., Poletto, G., Noci, G., & Kohl, J.L., *UVCS WLC Observations of Compressional Waves in the South Polar Coronal Hole*, 2000, ApJ, 529, 592

O'Shea, E., Banerjee, D., Doyle, J.G., Fleck, B., & Murtagh, F., *Active region oscillations*, 2001, A&A, 368, 1095

Parker, E. N., *Dynamics of the Interplanetary Gas and Magnetic Fields*, 1958, ApJ, 128, 664

Pätzold, M., Tsurutani, B. T., & Bird, M. K., *An estimate of large-scale solar wind density and velocity profiles in a coronal hole and the coronal streamer belt*, 1997, J.Geophys.Res., 102, 24151

Peter, H., *The nature of the solar transition region*, 2002, ESA SP-508: From Solar Min to Max: Half a Solar Cycle with SOHO, 11, 237

Phillips, K.J.H., *Guide to the Sun*, 1992, Cambridge University Press, 229

Pneuman, G. W., & Kopp, R. A., *Gas-Magnetic Field Interactions in the Solar Corona*, 1971, Sol.Phys., 18, 258

Quémerais, E., & Lamy, P., *Two-dimensional electron density in the solar corona from inversion of white light images - Application to SOHO/LASCO-C2 observations*, 2002, A&A, 393, 295

Ramsay, *Council note on the discovery of Helium*, 1896, Monthly Notices of the Royal Astronomical Society, 56, 262

Raouafi, N.-E., & Solanki, S. K., *Effect of the electron density stratification on off-limb O VI line profiles: How large is the velocity distribution anisotropy in the solar corona?*, 2004, A&A, 427, 725

Raymond, J. C., et al., *Composition of Coronal Streamers from the SOHO Ultraviolet Coronagraph Spectrometer*, 1997a, Sol.Phys., 175, 645

Raymond, J. C., Suleiman, R. M., van Ballegooijen, A. A., & Kohl, J. L., *Absolute Abundances in Streamers from UVCS*, 1997b, ESA SP-415: Correlated Phenomena at the Sun, in the Heliosphere and in Geospace, 383

Rense, W. A., *The Origin of Zodiacal Light*, 1952, ApJ, 115, 501

Rickett, B., *IPS observations of the solar wind velocity and microscale density irregularities in the inner solar wind*, 1992, Solar Wind 7 Colloquium, 255

Rutten, R.J., & Krijger, J.M., *Dynamics of the solar chromosphere IV. Evidence for atmospheric gravity waves from TRACE*, 2003, A&A, 407, 735

Schmidt, M., *Brightness, polarization and electron density of streamers in the solar corona*, 1953, Bulletin of the Astronomical Institutes of the Netherlands, 12, 61

Schwenn, R., & Marsch, E., *Physics of the Inner Heliosphere II - Particles, Waves and Turbulence*, 1991, Physics and Chemistry in Space Vol 21: Space and Solar Physics, Springer-Verlag,

Strachan, L., Kohl, J.L., Weiser, H., Withbroe, G.L., & Munro, R.H., *A Doppler dimming determination of coronal outflow velocity*, 1993, ApJ, 412, 410

Strachan, L., Panasyuk, A. V., Dobrzycka, D., Kohl, J. L., Noci, G., Gibson, S. E., & Biesecker, D. A., *Latitudinal dependence of outflow velocities from O VI Doppler dimming observations during the Whole Sun Month*, 2000, J.Geophys.Res., 2345

Strachan, L., Suleiman, R., Panasyuk, A. V., Biesecker, D. A., & Kohl, J. L., *Empirical Densities, Kinetic Temperatures, and Outflow Velocities in the Equatorial Streamer Belt at Solar Minimum*, 2002, ApJ, 571, 1008

Sturrock, P. A., & Smith, S. M., *Magnetic-Field Structure Associated with Coronal Streamers* ,1968, Sol.Phys., 5, 87

Swings, P., *Edln's Identification of the Coronal Lines with Forbidden Lines of Fe X, XI, XIII, XIV, XV; Ni XII, XIII, XV, XVI; Ca XII, XIII, XV; A X, XIV*, 1943, ApJ, 98, 116

Torrence, C., & Compo, G.P., *A Practical Guide to Wavelet Analysis*, 1998, Bulletin of the American Meteorological Society, 76, 61

Vaiana, G. S., Krieger, A. S., & Timothy, A. F., *Identification and Analysis of Structures in the Corona from X-Ray Photography*, 1973, Sol.Phys., 32, 81

van de Hulst, H. C., *Zodiacal Light in the Solar Corona.*, 1947, ApJ, 105, 471

Van de Hulst, H.C., *The Electron Density of the Solar Corona*, 1950, Bulletin of the Astronomical Institutes of the Netherlands, 11, 135

Waldmeier, M., *The coronal hole at the 7 March 1970 solar eclipse*, 1975, Sol.Phys., 40, 351

Wang, T.J., Solanki, S.K., Curdt,W., Innes, D.E., Dammasch, I.E., & Kliem, B., *Hot coronal loop oscillations observed with SUMER: Examples and statistics*, 2003, A&A, 406, 1105

Warren, H. P., Mariska, J. T., Wilhelm, K., & Lemaire, P., *Doppler Shifts and Nonthermal Broadening in the Quiet Solar Transition Region: O VI*, 1997, ApJL, 484, L91

Whipple, F. L., & Gossner, J. L., *An Upper Limit to the Electron Density Near the Earth's Orbit.*, 1949, ApJ, 109, 380

Withbroe, G. L., Kohl, J. L., Weiser, H., Noci, G., & Munro, R. H., *Analysis of coronal H I Lyman alpha measurements from a rocket flight on 1979 April 13*, 1982, ApJ, 254, 361

Withbroe, G. L., Kohl, J. L., Weiser, H., & Munro, R. H., *Probing the solar wind acceleration region using spectroscopic techniques*, 1982, Space Sci. Rev., 33, 17

Woo, R., & Habbal, S. R., *Imprint of the Sun on the Solar Wind*,1999a, ApJL, 510, L69

Woo, R., Habbal, S. R., Howard, R. A., & Korendyke, C. M., *Extension of the Polar Coronal Hole Boundary into Interplanetary space*, 1999b, ApJ, 513, 961

Woo, R., Habbal, S. R., & Feldman, U., *Role of Closed Magnetic Fields in Solar Wind Flow*, 2004, ApJ, 612, 1171

Young, C. A., *Pending problems in astronomy*, 1884, The Observatory, 7, 316

Zangrilli, L., Poletto, G., Nicolosi, P., Noci, G., & Romoli, M., *Two-dimensional Structure of a Polar Coronal Hole at Solar Minimum: New Semiempirical Methodology for Deriving Plasma Parameters*, 2002, ApJ, 574, 477